Group 13 Metal Doping of Cadmium Selenide Nanocrystals and Atomic Layer Deposition of Copper Oxide and Copper Aluminum Oxide

A DISSERTATION
SUBMITTED TO THE FACULTY OF THE
UNIVERSITY OF MINNESOTA
BY

Joshua Paul Halverson

IN PARTIAL FULFILLMENT OF THE REQUIREMENTS
FOR THE DEGREE OF
DOCTOR OF PHILOSOPHY

Wayne L. Gladfelter, Advisor

May, 2017

Abstract

Semiconductors are a broad class of materials and by extension present a large array of possibilities for potential research. This thesis looks at two different areas of semiconductor research. The first is electronic doping of semiconductor nanocrystals and the second is the deposition of copper aluminum oxide via atomic layer deposition (ALD).

Semiconductor nanocrystals are semiconductor particles with diameters less than 10 nm. At these size ranges, semiconductor nanocrystals display several unique electrical and optical characteristic due to quantum confinement. Quantum confinement is a phenomenon that arises when the physical size of the nanocrystal is smaller than the wavefunction size of the electrons and holes that allow electrical conductivity in semiconductors. These quantum confinement effects are tunable based on the size of the nanocrystal, which allows one material to have a broad range of possible uses. Even greater control could be had if semiconductor nanocrystals could be doped with heterovalent dopants, as is seen in traditional semiconductors. This thesis look at incorporating group 13 dopants into cadmium selenide nanocrystals and found that while the dopants had effects on the electronic structure of the nanocrystals they were not successfully incorporated into the nanocrystals. The dopants instead were bound to the surface of the nanocrystal.

Copper aluminum oxide has generated interest as a potential p-type transparent conductive oxide. Thin films of this material have been deposited via physical vapor methods. Depositing this material via ALD provides a great level of film thickness control, which is critical in many thin film devices. Deposition of copper containing films via ALD

has been hampered by a lack of suitable copper precursor. As a solution to that problem, this thesis demonstrates the construction of an ALD deposition system that can use both solid and liquid ALD precursors. This system with its extended capabilities was then used to deposit thin films of copper aluminum oxide using solid copper precursors.

Table of Contents

List of Figures

List of Diagrams

of the two plates. It shares materials, cutout pattern, and hole positions with the top plate. The holes are drilled and tapped for the 10-24 screws from the top plate. Page 3 is for the two cradle arms. They are also made from 0.5” aluminum with cutouts to save weight. They have a radiused section to hold the main reactor body, and they are attached to the top plate with the 10-24 screw from the top plate. Page 4 is an overview of the main ALD cradle showing how all of the various component fit together.

List of Equations

List of Tables

Chapter 1:

1.1 Background:

1.1.1 Nanocrystals: Faraday is given credit for the first example of nanocrystals, as he noted a liquid that changed colors when he added phosphorus to gold chloride. He deduced the result as being particles of gold, so small as to not be differentiated by a microscope, had formed from the reduction of gold chloride.[1] From these beginnings, the development of nanocrystals as a discreet branch of research has grown out of the meeting of traditional colloid research and 2-D quantum confined structures such as superlattices.[2-3]

Colloid chemistry, is the study of materials that form the bridge between mechanical suspensions and molecular solutions.[2, 4-5] During the 1980s heterogeneous colloid catalysis was applied to semiconductors, as the donor electrons needed for catalysis could be generated photonically. At the time, it was hoped to use colloidal semiconductors to photosensitize the reduction of water, as a means of storing solar energy.[5-6] In an effort to achieve this goal, colloidal sizes were pushed even smaller, both to increase surface area, and to increase light penetration into these solutions. As the size of these colloidal particles continued to decrease researchers began to notice that these "nanoparticles" had properties dependent upon the size of particle. These size dependent effects are a consequence of quantum confinement and as researchers began to enter this regime much interest was generated in the size dependent properties of these unique materials[5, 7-10]

1.1.2 Quantum Confinement: A series of energetic effects observed when wavefunctions, which have a discreet size, become physically confined by the material within which they are housed. The application of boundary conditions to the wavefunction causes an increase in the ground state energy of the wavefunction as well as a quantization of the energy of

the wavefunction (Figure 1.1b).[11] From the perspective of the electron, hole, or exciton a bulk single crystal is effectively infinite in three dimensions. However, these wavefunctions do have a finite radius, a_e, a_h, *and* a_{exc} respectively. So, if the size of the material in any dimension becomes small with respect to these radii, then the respective wavefunction becomes confined by the limited size of the material.

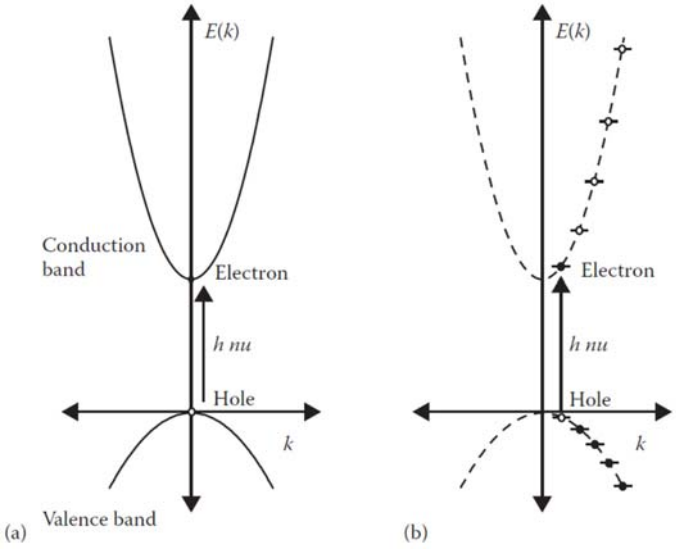

Figure 1.1: A cartoon showing the band diagram for an idealized direct bandgap semiconductor (a) and how that band diagram changes, developing discreet transitions, under the effects of quantum confinement (b).

The confinement of the three distinct wavefunctions, electron, hole, and exciton, leads to the formation of three distinct confinement regimes. The strong confinement regime, the particle is smaller than the radii of all three wavefunctions. The intermediate confinement regime, the particle is smaller than a_{exc} and either a_h *or* a_e. Finally the weak

confinement regime, only the exciton wavefunction is constrained by the size of the nanocrystal.[11] From equation 1.1, it is possible to see why quantum confinement affects holes and electrons differently. Since the material dielectric constant (ε), electron mass (m), and the hydrogen atom Bohr radius (a_o) are constant, only the effective mass of the particle (m^*) determines the Bohr radius of that particle. Electrons have the lightest effective masses; they have the largest Bohr radii. This leads to the electron wavefunctions being more strongly confined, and therefore having a higher energy. This is why electron (conduction band) levels are typically more discreet and have greater energy separations than the hole (valence band) levels. This can be visualized in figure 1b.[11] The increase in energy resulting from wavefunction confinement is also responsible for the increase in bandgap energy as nanocrystal size decreases. Interest in quantum confinement resulted in the field of nanocrystals being born as a discreet branch of research. However, initial excitement was tempered by the experimental difficulties of producing samples of high enough quality to observe the effects of quantum confinement predicted by theory.

$$a_{B(a_{exc,}\, a_h\, or,\, a_e)} = \varepsilon \frac{m}{m^*} a_o \tag{1.1}$$

1.1.3 Doping: Doping is the process of intentionally adding defects into a semiconductor to control its properties. Traditionally elements with extra electrons, such as phosphorous in silicon, are added to introduce electrons into the conduction band of the semiconductor to increase conductivity. These are n-type doped semiconductors. While elements with fewer electrons, such as boron in silicon, are added to introduce positive charger carrier holes into the valence band. These are p-type doped semiconductors.

1.1.4 Nanocrystal Doping: Traditional semiconductor methodologies rely on having essentially defect free starting materials and from there doping in the impurities to allow

the semiconductor to function as needed.[12] This approach does not translate well to the doping of nanocrystals. Nanocrystals with their small size, high number of defects, and a high percentage of the atoms present at the surface are vastly different from bulk semiconductors. This coupled with the fact that in order to ensure even one dopant atom per nanocrystal doping quantities must be orders of magnitude higher than traditionally doped semiconductors.

Initial attempts at doping semiconductor nanocrystals were derived from traditional semiconductor doping methods. Using dopants with very high solubilities, up to 50% in the bulk semiconductor.[13,15,16] These dopants were added to the nanocrystal synthetic solution to incorporate them into the nanocrystal.[13-14] These early attempts were all failures, and nanocrystals began to develop a reputation for being "self-purifying" and hence un-dopable.[15-17] The problems result from the differences between bulk semiconductor synthetic methods, and nanocrystal colloidal methods. High temperature bulk semiconductor synthesis allows for facile diffusion, and is therefore limited by thermodynamic constraints. The relatively low temperature colloidal synthesis, may never reach the equilibrium required to be thermodynamically controlled, and hence is subject to kinetic controlled.[15] Doping bulk semiconductors is determined solely by the Gibbs free energy change associated with increase in local defects. While in nanocrystals doping is determined by a balance between the free energy changes of dopant incorporation, lattice formation, solvation, and the kinetic factors associated with these processes.[15, 17]

Nanocrystal nucleation results from the free energy change for the formation of the crystalline lattice. However, this is being opposed by the free energy change of ion solvation. This leads to a critical particle radius, beyond which the free energy change for

the lattice formation is greater than the free energy change of ion solvation, and the particle will not be able to dissolve back into solution. Impurities can interrupt this nucleation process, and since impurities in a crystalline lattice are inherently higher in energy, this can lead to impurity exclusion from the lattice.[15, 17] This makes nanocrystals very difficult to dope with impurities. In order to dope a nanocrystal with an impurity atom, the impurity-surface interaction must be kinetically stable. Stable enough, so that the impurity is retained on the nanocrystal surface long enough to be incorporated into the growing crystalline lattice.[15, 17]

Of the successful incorporation of dopants into nanocrystals there are two broad categories, the incorporation of isovalent dopants, and heterovalent dopants. The first example of isovalent dopant incorporation into a semiconductor nanocrystal was the doping of manganese into zinc sulfide nanocrystals.[18] Manganese has also been doped into many other II-VI semiconductor nanocrystals including: CdSe[14], ZnSe[19], and PdSe[20]. Isovalent doping is less influenced by many of the problems associated with nanocrystalline doping, which is why many of the best know examples of doped nanocrystalline systems involve isovalent dopants.[13, 15-16] The synthetic challenges of nanocrystalline doping become much more problematic with heterovalent dopants.

P-type II-VI semiconductor nanocrystals, those that contain extra holes as carriers, have traditionally been synthesized through cation exchange. The metal salt of the dopant of interest is added to a solution of semiconductor nanocrystals, there is a reversible cation exchange reaction to produce doped semiconductor nanocrystals. It was shown that if silver and copper salts were added to solutions of CdSe, the result was p-typed CdSe.[21]

N-type II-VI semiconductor nanocrystals, those that contain extra electrons, are

traditionally made through impurity doping. However, the first example of n-type CdSe was created using standard chemical reduction techniques.[22-24] N-type doping of II-VI semiconductor nanocrystals has focused primarily on the group 13 elements. The more recent work has been on the incorporation of indium into CdSe.[25-27]

1.1.5 Nanocrystal Synthesis: II-VI semiconductor nanocrystals were originally synthesized by precipitation from a hydrogen chalcogenide gas and a metal ion. Alkali metal salts of the chalcogen were also used.[2-3, 5] The reactions were carried out in solvents with poor metal and semiconductor solubilities, and the resulting products were often washed with solutions of polyphosphines, phosphine oxides, and amines to act a capping and stabilizing agents.[2-3, 5, 28-29]

These precipitation-based syntheses resulted in poor control over the size dispersity of the sample. Polydispersity, with its overlapping electronic transitions, hides the quantized transitions predicted in nanocrystal theory.[2-3, 5, 7-9] The ideal synthesis for monodisperse nanocrystals is a two-step process. First a discreet nucleation step that starts all of the nanocrystals in the system growing from the same beginning. This is followed by a slow growth process step. This slow growth decreases the number of defects in the nanocrystal and allows for better control over the final size of the nanocrystal.[2-3, 5, 7-10, 30] (Figure 1.2).[13]

Initial attempts consisted of trying to control the sample size dispersion by controlling the size of the reaction area. This was done using confined structure synthetic techniques, such as: synthesis in reverse micelles,[28-29] in vesicles[31], and in zeolites[32]. These methods did give better control than precipitation methods over the final size of the nanocrystals. They were still polydisperse samples. Furthermore, since the nucleation and

growth steps of these syntheses are concurrent it was difficult to optimize the reaction appropriately to achieve the desired monodisperse samples.[2-3, 5, 28-29]

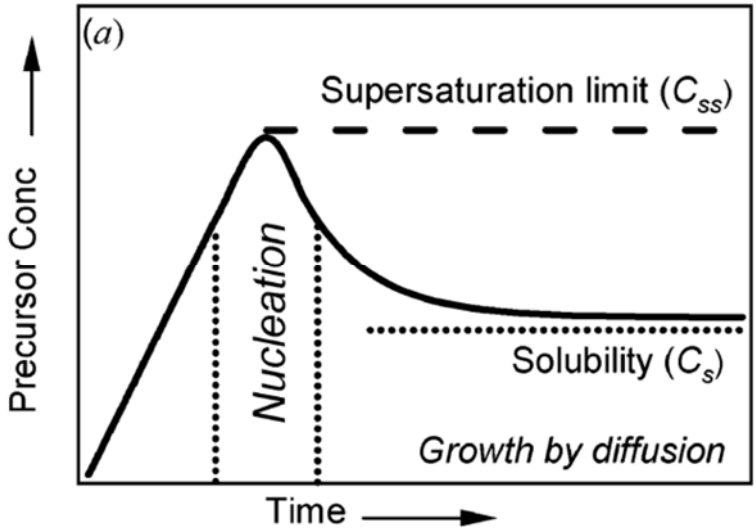

Figure 1.2: A graph of precursor concentration vs. time during a hot injection nanocrystal synthesis. Reprinted from Bryan, J. et al. 2005

Further efforts by *Murray et al.* offered a solution to the problem.[9] They began with a hot coordinating solvent, a mixture of trioctylphosphine (TOP) and trioctylphosphine oxide (TOPO), and injected into that a mixture of dialkyl cadmium and selenium dissolved in TOP.[9] This causes the reactant concentrations to rise above the super-saturation limit, causing a brief period of nucleation. This is followed by a slower period of diffusion-controlled growth until the reactant concentrations fall below the saturation limit.[9, 13, 30] (Figure 1.2). The nanocrystal size can be monitored via ultraviolet-visible (UV-Vis) spectroscopy. The first absorption shifts as a function of particle size due to quantum confinement effects. The TOP/TOPO solvent mixture also serves as the capping agents for the nanocrystals. The long chain alkyl groups prevent the increase of size dispersity from

Van der Waals aggregation and Ostwald ripening. The phosphine (phosphine oxide) groups help to pacify surface defects and prevent surface oxidation. They also increase the solubility of the nanocrystals in numerous organic solvents.[9, 13] The nanocrystals were separated using a size-selective method of gradually increasing the polarity of the organic solvent. This gradual increase in polarity destabilized the largest particles in solution, causing a reversible flocculation.[9] Repeating this size-selective precipitation allowed for the preparation of monodisperse, size-controlled, semiconductor nanocrystal samples. While the synthesis used in this work was based on the work of *Murray et al.* there have been two improvements that have been incorporated in the synthesis used here. First, replacing the pyrophoric organometallic reagents with safer metal oxide precursors.[33] Secondly, modifying the solvent system by adding hexadecylamine (HDA) to increase monodispersity, and to remove the need for size-selective precipitation.[34]

A separation of steps, nucleation from growth, was needed in order to produce monodisperse nanocrystal samples. Similar methodology is being developed to synthesize doped nanocrystals. By separating nanocrystal nucleation, from nanocrystal doping and growth, the detrimental effects dopants have on nucleation are avoided, and the conditions for doping can be optimized. Several synthetic methods have been tested in an effort to successfully dope CdSe nanocrystals.

Successive ion layer adsorption and reaction (SILAR) is a technique combining chemical bath deposition and atomic layer epitaxy. It was originally developed for use in thin films.[35] The controlled growth of epitaxial materials is allowed by only introducing one precursor at a time. This allows time for each precursor to react completely, minimizing defects and producing more uniform crystalline structures. The advantages of

SILAR methods are numerous when attempting to dope semiconductor nanocrystals. The lower temperatures used prevent secondary nucleation. The longer reaction times allows for the use of more stable reagents, and allows more time for the dopant to be incorporated into the material. The epitaxial nature of the growth material helps preserve the narrow original size distribution.[36]

Seeded injection type syntheses use a traditional hot, coordinating solvent precursor injection, but the injection contains presynthesized nanocrystals, "cores". The main benefit of this type of synthesis is the ability to grow much larger particles than is possible with SILAR type syntheses, from tens to hundreds of nanometers.[37] These larger nanocrystals provide more material and locations for dopant incorporation. However, the higher temperatures used in seeded injection syntheses do lead to more polydispersity and secondary nucleation events than is present in SILAR type syntheses.

Not all doping experiments need to be conducted during the synthesis of the nanocrystals. Due to their high surface area to volume ratio dopants can be added later via cation exchange. Dopants diffusing into semiconductors has been well studied.[38] While the high temperature methods of traditional semiconductor doping allow for facile diffusion, they are less applicable here. Room temperature rates of diffusion are not high, and root mean square diffusion distances are measured in nanometers per hour.[39] But, given their sizes, on the order of nanometers, their high surface areas, and defect filled structures there still can be appreciable dopant diffusion into semiconductor nanocrystals. It has been shown that silver will diffuse readily into CdSe.[40] If given enough time the entire nanocrystal will convert to Ag_2Se. The rates of diffusion for group 13 metals are much lower in CdSe that for silver, there is still a diffusion distance on the order of nanometers

over approximately 24 hours.

1.1.6 Doping Characterization: Certain dopants such as manganese and cobalt are favored when studying doped semiconductor nanocrystals. Manganese has a very distinct electron paramagnetic resonance (EPR) splitting pattern, which is sensitive to local environmental changes.[13-14, 19-20] Cobalt has unique magnetic circular dichroism (MCD) pattern that is local environment sensitive.[13] These dopants are favored as they have a well-defined characterization method. Many dopants, lacking a clear, definite characterization technique, must be characterized more broadly. The heteroatoms are introduced to change the electronic properties of the material. To create more free charge carriers. In direct band gap semiconductors, such as CdSe, these changes in electronic structure can be measured spectroscopically, as electrons can be excited with light. Spectroscopic methods, such as UV-Vis absorption, photoluminescence excitation (PL), and IR spectroscopy, form a foundation of measurement when studying heteroatom doping in semiconductor nanocrystals.

According to theory there are two spectroscopic signatures expected from introducing permanent free charge carriers to semiconductor nanocrystals. A blue shift in the first UV-Vis absorption and PL spectra. States close to the bandgap would be filled with free charge carriers and more energy would be required to excite electrons to unfilled states. A signal in the IR spectrum would begin to grow as the level of doping increased due to intraband transitions of the free charge carriers. Signals as clear as these are very rarely, if ever, seen in nanocrystalline systems. The first example of n-type CdSe was created using standard chemical reduction techniques.[22-24] This is the only work thus far to show the IR transitions predicted by nanocrystal theory in n-type CdSe. There is also a

report of copper doped zinc selenide prepared by copper dopant incorporation, not cation exchange. This sample contains permanently active optical holes and is one of the few examples of permanent optical features from heteroatom incorporation into II-VI semiconductor nanocrystal.[41]

While there has been on incorporating group 13 metals, such as indium, into CdSe, these systems fail to show any of the predicted spectroscopic transitions.[25-27] Several novel characterization methods were introduced however, including single particle energy-dispersive X-ray spectroscopy[25], to measure the dopant concentration on a per particle basis and terahertz spectroscopy[27], to measure the change in conductivity of the nanocrystals as a function of their polarizability. Novel characterization methods aside, too much of the foundation of these works is drawn from statistical calculations, such as Fermi-Dirac statistics[25], to support the claim that these nanocrystals have been successfully doped.

1.1.7 Extended X-ray Absorption Fine Structure (EXAFS): EXAFS is an extension of x-ray absorption spectroscopy and was developed over decades alongside improvements in x-ray and computer technology.[42] X-rays are absorbed by elements when the X-rays are energetic enough to eject a core electron. This gives each element a distinct set of x-ray absorption lines. This is x-ray absorption spectroscopy. Energetically above the absorption edge non-monoatomic samples display a sinusoidal oscillation in the absorption signal. These oscillations are the EXAFS signal (Figure 1.3). These oscillations are a result of the ejected photoelectron interacting with atoms surrounding the excited atom. The photoelectron wave can be back scattered to the excited atom where it can interfere with the newly excited photoelectrons. The ejected photoelectron has energy equal to the energy of the incoming photon, minus the binding energy of the electron. The energy, and

therefore the frequency, of the ejected photoelectron changes as the energy of the incoming photon increases. The changing frequency of the ejected photoelectron changes how it interacts with the back scattered electron and newly created photoelectrons. These patterns of constructive and destructive interference lead to the oscillations seen in the EXAFS portion of the x-ray absorption spectra. Models can be created to investigate the local eviroment of the absorbing atom. Theorectical EXAFS spectra can be generated from these models and compared to the measured spectrum. This allows for a large amount of information about the local enviroment of the absorber atom to be obtained from the EXAFS experiment.

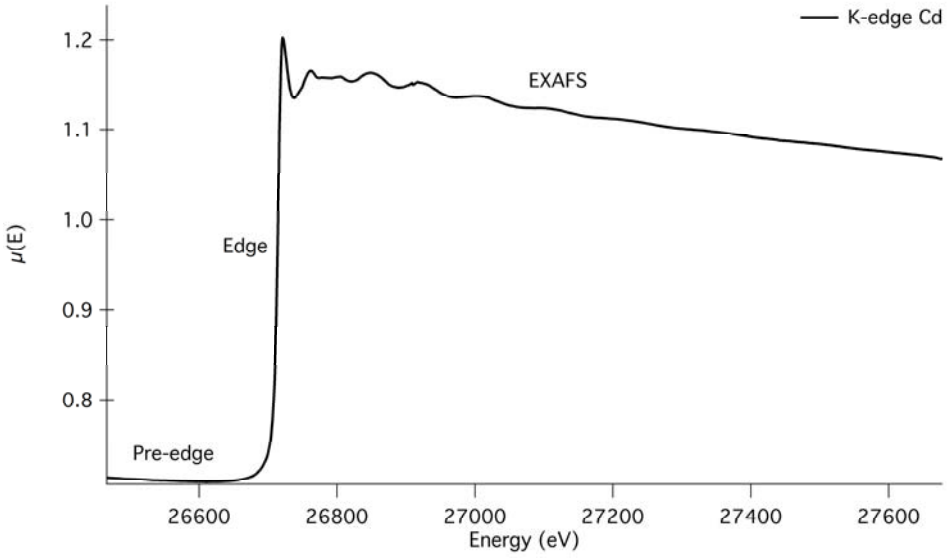

Figure 1.3: An x-ray absorption spectra showing the various parts of the spectra as well as the EXAFS oscillations.

1.2 Experimental:

1.2.1 CdSe Particle Synthesis: 411 mg of cadmium oxide, 8.0 g of trioctylphosphine oxide (TOPO), 18.0 g of hexadecylamine (HDA), and 1.62 g of dodecylphosphonic acid (DDPA)

are loaded into a 100 mL 3-neck flask capped with a rubber septum, condenser, and thermocouple. The system is heated to 60 °C, degassed and purged with nitrogen three times over an hour. Under nitrogen the reaction is heated to ~300 °C to allow the formation of clear cadmium adduct $Cd(DDPA)_2$. In a nitrogen glove box, selenium shot is added to trioctylphosphine (TOP) and allowed to stir for 24 hrs. creating a 1 M solution of trioctylphosphine:selenium. A 20 mL syringe is prepared in the glove box containing 14.0 mL of TOP, 4.0 mL of trioctylphosphine:selenium (TOP:Se), and 0.3 mL of diphenylphosphine. Once clear $Cd(DDAP)_2$ is form the system is cooled to 270 °C. The contents of the prepared syringe is quickly injected into the reaction mixture. The color change of the reaction is used to determine the appropriate particle size. After the desired particle size is reached the reaction is removed from heat, and cooled to 60 °C. The particles are precipitated with methanol, then ethanol, and redispersed into hexanes. After sitting overnight in hexanes the nanocrystal solution is poured off to remove the remaining excess ligand and surfactant.[36]

1.2.2 SILAR Doping Synthesis: A 0.1 M solution of cadmium oleate is prepared by adding 3.1 g of oleic acid to 642 mg of cadmium oxide in 46.5 mL of octadecene. The solution is heated under nitrogen to ~220 °C until the solution turns clear. A 1 M TOP:Se solution is prepared as described in the CdSe nanocrystal synthesis. Presynthesized CdSe nanocrystals (37.5 nmol) are added to a 100 mL 4-neck flask along with 5.0 g of HDA, 50.0 mL of phenyl ether, and the dopant complex. Group 13 metal acetylacetonates (acac) such as aluminum acetylacetonate $[Al(acac)_3]$ were used as dopants. The flask is capped with a thermocouple, rubber septum, a condenser, and a dropping funnel. The mixture is heated to 65 °C, degassed and purged with nitrogen three times over an hour. In a nitrogen glove

box a 20 mL syringe containing 14.4 mL of TOP and 1.6 mL of 1 M TOP:Se is prepared and injected into the dropping funnel. The reaction mixture is heated to 230 °C and the $Al(acac)_3$ is allowed to interact with the CdSe nanocrystals for 10 min. Sufficient TOP:Se to form one half of a monolayer (~.5 mL) is added to the reaction mixture via dropping funnel and stirred for 10 min. 16.0 mL of cadmium oleate is then injected via syringe and allowed to stir for 10 additional minutes. Finally the TOP:Se is added drop wise over the next 3.5 hours. After the addition of the TOP:Se the reaction is allowed to stir for another 20 min at 230 °C. The reaction is then cooled to 50 °C and precipitated twice with acetone, and once with ethanol. The particles are then redispersed in hexanes. After sitting overnight in hexanes the nanocrystal solution is poured off to remove the remaining excess ligand and surfactant.[36]

1.2.3 Quantum Yield Experiments: CdSe nanocrystals prepared by the SILAR method dispersed in hexanes were precipitated with methanol. Then precipitated with 50/50 methanol/ethanol and finally with ethanol to remove any residual HDA. They were redispersed into spectroscopic grade hexanes, with each solution set to have an absorbance of 0.200 at 400 nm. Rhodamine 6G dispersed in spectroscopic grade methanol was used a comparison standard for computing quantum yields. Each CdSe sample was excited at 400 nm and a photoluminescence spectrum was taken. The sample was removed and the Rhodamine 6G standard was immediately scanned with an excitation wavelength of 400 nm.

1.2.4 Inductively coupled plasma elemental analysis: Throughout the experiment extensive care was taken to prevent aluminum contamination of the particle solutions. All acids were trace metal grade and only 18 MΩ water was used. All equipment was soaked

for twenty four hours in bleach water, followed by twenty four hours in a 1% HCl solution, followed by at least twenty four hours in water. The equipment was left in the water solution until use. Samples were added to 2mL of aqua regia and allowed to digest for fifteen minutes until all traces of color were gone. The solutions were diluted to 50 ml with a 5%HCl/2%HNO_3 solution and then submitted for analysis.

1.2.5 Extended X-ray Absorption Fine Structure Experiments (EXAFS): CdSe nanocrystals prepared by the SILAR method dispersed in hexanes were precipitated with methanol. Then precipitated with 50/50 methanol/ethanol and finally with ethanol to remove any residual HDA. The nanocrystals were redispersed into hexanes and dried under vacuum overnight, to a viscous putty.

1.3 Characterization:

1.3.1 UV-Vis Spectroscopy: All measurements were taken on an Ocean Optics USB4000 spectrophotometer using an integration time of 5 seconds and averaging 100 scans. All spectra were taken using a quartz cuvette with a 1.00 cm path length.

1.3.2 Infrared Spectroscopy: All measurements were taken on a Nicolet 560 magna IR, FTIR spectrometer using a resolution of 2 cm^{-1} and averaging 32 scans. Films were drop cast onto salt plates before measuring.

1.3.3 Photoluminescence Spectroscopy: All measurements were taken on a Spex Fluorolog 1680 0.22 m Double Spectrometer, scanning in 1 nm increments with a 0.5 second integration time. The excitation wavelengths used are listed in the respective figures.

1.3.4 X-ray Diffraction: All measurements were taken on a Bruker-AXS Microdiffractometer using a copper Kα x-ray source and a 0.8 mm spot size. Samples were

drop cast onto silicon wafers before measurement. Each sample was scanned twice, once at $2\theta = 35°$ and $\Omega = 17.5°$ for 5 minutes and once at $2\theta = 60°$ and $\Omega = 30°$ for 5 minutes. The spectra were combined and peaks were fitted using MDI JADE 9. The line width broadening analysis was done using the Scherrer equation in MDI JADE 9 with LaB_6 used to compensate for the line broadening of the instrument.

1.3.5 TEM: All measurements were taken on a FEI Tecnai G^2 F30 electron microscope. Samples were prepared on TedPella formvar carbon copper 200 mesh grids that were dipped in a solution of the sample dispersed in toluene. All size analyses were done using a pixel length comparison to the attached scale bar in Adobe Photoshop.

1.3.6 Elemental Analysis, ICP-MS: Measurements were taken on a Thermo Scientific XSERIES 2 ICP-MS with ESI PC3 Peltier cooled spray chamber, SC-FAST injection loop, and SC-4 auto sampler. Samples were diluted appropriately and 20 ppb of Y internal standard was added. All elements were analyzed using He/H_2 collision-reaction mode.

1.3.7 EXAFS: Samples were measured on the BM20B at Argonne National Labs. 1-2 mg of each sample was pressed into kapton tape and measured. Spectra were measured from -250 eV to -40 eV in 5 eV steps, from -40 eV to 30 eV in 1.4 eV steps, and from 30 eV to 973.38 eV in 0.05 k steps, all using a 1s integration time per step. All eV values are given relative to the k absorption edge of the element being analyzed. Cadmium and selenium measurements were done via absorption and gallium measurements were done via both absorption and fluorescence. Data reduction was done using the xafsX utilities.[43] Spectra modeling and comparison was done using the Demeter XAS package.[44]

1.4 Results:

1.4.1 CdSe Particle Synthesis: The synthesis used in this work is based on that of Reiss

et. al. The synthesis incorporates the use of non-pyrophoric precursors and the addition of HDA.[45] HDA focuses the size dispersion of the nanocrystals and removes the need for a post-synthesis size-selective precipitation.[34, 45] Another deviation in the synthesis is the addition of diphenylphosphine to the mixture of TOP:Se and TOP. Diphenylphosphine was shown to increase the yield of the synthesis, to greater than 75%.[46]

The quality of the nanocrystals synthesized can be assessed optically by measuring the full width at half maximum (FWHM) of the first absorption and luminescence peaks, or by a statistical TEM measurement, looking for low shape and size dispersion. Figure 1.4 displays sharp peaks for both the absorption and luminescence spectra, with the FWHM of the emission peak being 31 nm. These narrow peaks are indicative of a monodisperse system of low size dispersion and the spectra agree well with previously published results.[7-10, 34, 45, 47-48]

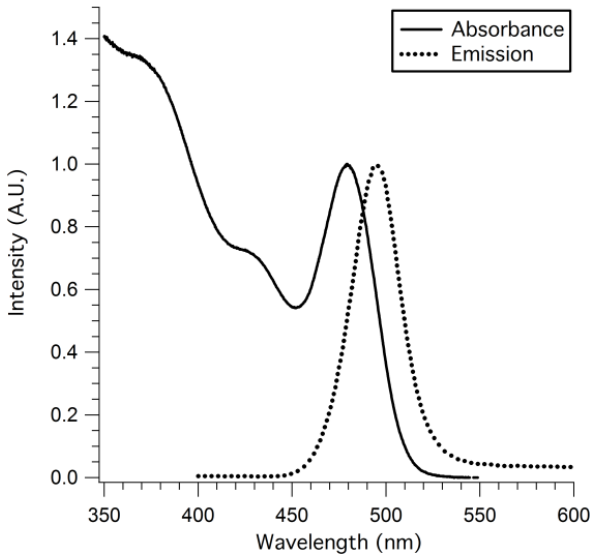

Figure 1.4: Normalized UV-Vis absorption and photoluminescence (300nm excitation) spectra of CdSe nanocrystals.

The bandgap and extinction coefficient of CdSe is dependent on size, and both have been fitted by polynomial equations from TEM and XRD data.[49] Equation 1.2[49] allows the calculation of the nanocrystal diameter (D) from the λ_{max} of the first absorption peak.

$$D=(1.6122\times10^{-9})\lambda^4-(2.6575\times10^{-6})\lambda^3+(1.6242\times10^{-3})\lambda^2 -(0.4277)+(41.57) \quad (1.2)$$

Equation 1.3[49] allows the concentration [C(M)] to be calculated from the absorbance (A) of λ_{max}, the nanocrystal diameter (D) and the length of the cuvette (L).

$$C = \frac{A}{5857(D)^{2.65} \times L} \quad (1.3)$$

From equations 1.2 and 1.3 the diameter and concentration of the CdSe nanocrystals is 2.17 nm and $2.00\text{x}10^{-4}$ M, respectively.

Another measure of the quality of semiconductor nanocrystal sample is the degree of crystallinity in the sample. Figure 1.6 (undoped) is an XRD spectra of 2.17 nm CdSe nanocrystals. The spectrum predominately shows the peaks expected for hexagonal CdSe. The expected phase of CdSe, especially at the higher temperatures used during the synthesis.[50] There is some intermixing between the hexagonal and cubic phases. The limited crystalline domains in the nanocrystals mean that even a few stacking faults can cause blurring of phase specific peaks in the XRD spectrum. The spectrum does display a lot of line broadening and noise due to the small size of the nanocrystals.[9] Scherrer line width analysis gives a crystalline diameter of 2.14 nm, in very close agreement with the UV-Vis data.

1.4.2 SILAR Doping Synthesis: The SILAR synthesis is designed to add new material to the nanocrystal monolayer by monolayer. The slower reaction rate will help to preserve the

crystallinity of the sample as well as increase the likelihood of dopant incorporation into the nanocrystal. A series of samples prepared by SILAR methods and doped with aluminum (Table 1.1) was prepared to study the doping of CdSe nanocrystals with group 13 dopants. As with the undoped CdSe nanocrystals UV-Visible and photoluminescence spectroscopy was used to investigate the quality of the nanocrystals. (Figure 1.5) All of the samples show a broadened first absorption transition and photoluminescence spectrum. That along with a decreased distance between the peak of and the valley after the first absorbance transition is indicative of a larger size dispersity of the nanocrystal sample.

Sample	Abs. Maxima (nm)	PL Maxima (nm)	UV-Vis Size (nm)	XRD Size (nm)
Undoped	574	606	3.63	3.53
0.085 mol% Al	598	612	4.50	4.63
0.17 mol% Al	585	602	3.99	3.56
0.26 mol% Al	583	597	3.92	3.46
2.3 mol% Al	584	592	3.95	3.55

Table 1.1: Spectroscopic data of the SILAR prepared CdSe samples. Listed UV-Vis nanocrystal sizes are calculated from the polynomial method listed previously. XRD sizes listed are calculated from Scherrer line width analysis as listed previously. All doping percentages given in this work are the amount of dopant added to the reaction mixture relative to the amount of cadmium precursor added (mol%). They are not representative of the actual percentage of dopant incorporated into the particle.

This is consistent with the longer reaction times of the SILAR synthesis, hours vs. a few minutes for the original sample synthesis, and is an effect previously reported.[9-10, 45] The addition of the aluminum dopant to the reaction mixture helps maintain the monodispersity

of the sample. This has been seen for other group thirteen dopants.[26]

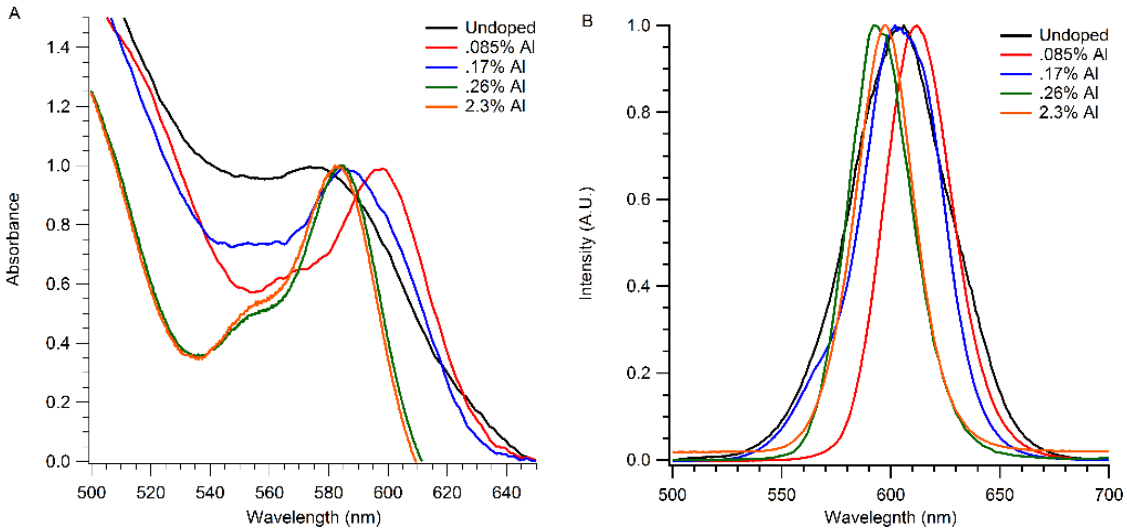

Figure 1.5: Figure A. shows a UV-Vis spectra of the nanocrystals prepared by SILAR and doped with aluminum. All of the spectra have been normalized to the first absorption peak. The .26% Al and 2.3% Al samples show a better defined first absorption as the reaction time was reduced from 3.5 hrs. to 1hr. Figure B shows a normalized PL spectra of the nanocrystals prepared by SILAR and doped with aluminum.

All five samples still show the effects of quantum confinement. The spectra show an increase in the optical band gap energy from 709 nm of bulk CdSe.[51] There are also peaks in the spectra that correspond to the various quantum confined optical transitions. Using the polynomial method established earlier[49] the particles range in size from 3.63 nm to 4.50 nm in diameter. The XRD data supports this with sizes ranging from 3.53 nm to 4.63 nm. As can be seen from the XRD data (Figure 1.6) the nanocrystals still predominately display the reflections of hexagonal CdSe.

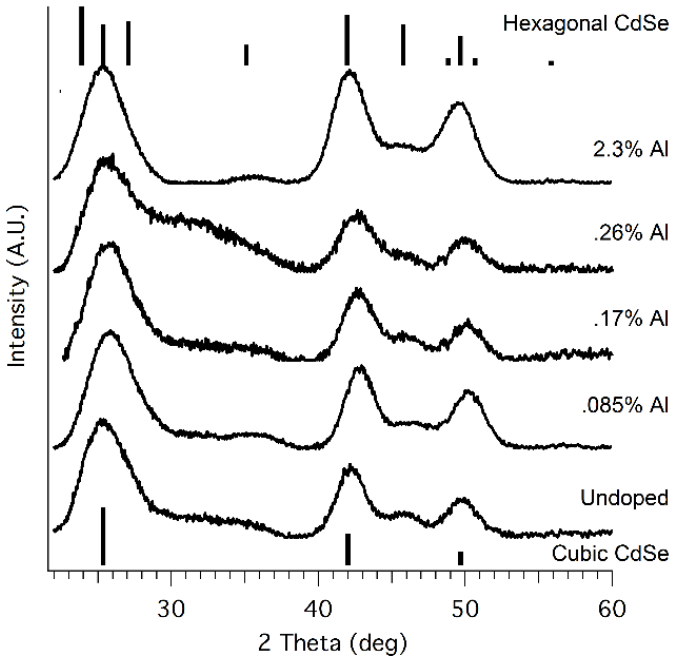

Figure 1.6: XRD spectra of SILAR samples. The diffraction peaks for cubic and hexagonal CdSe are shown on the bottom and top of the figure respectively.

These particles also show no evidence of electronic doping. The first transition, the $1S_h$-$1S_e$ transition is still visible in all of the spectra, this would be absent if electrons had been placed in the delocalized $1S_e$ state.[22-24] The photoluminescence peaks of the CdSe:Al samples display similar Stokes shifts than the undoped CdSe sample. If the samples were electronically doped this would be observed as a larger Stokes shift than the undoped sample. Along with the disappearance of the $1S_h$-$1S_e$ transition in the visible spectrum. There should be a concurrent growth of the $1S_e$-$1P_e$ transition in the IR spectrum. This $1S_e$-$1P_e$ transition has been observed experimentally.[22-24] The energy of the $1S_e$-$1P_e$ transition can be calculated with equation 1.4, where $\alpha_{n,l}^2$ is the nth zero of the lth order Bessel

function, a is the particle radius in meters, and m_e^* is the effective mass of the electron.[11] For particles ranging in size from ~3.5 nm to ~4.5 nm, the $1S_e$-$1P_e$ transition would begin at ~3300 cm^{-1} or ~2000 cm^{-1} respectively and it would be approximately 1500 cm^{-1} wide. A trap state to quantum confined state transition, or a newly formed dopant state to a quantum confined state transition would be observable in the IR as well. Studies on indium and tin dopants in CdSe have concluded that the dopant levels formed are 280 meV (2258 cm^{-1}) and 100 meV (807 cm^{-1}) below the conduction band, respectively.[25]

$$E_{n,l} = \frac{\hbar^2}{2a^2}\left\{\frac{\alpha_{n,l}^2}{m_e^*}\right\} \tag{1.4}$$

The IR spectra of the SILAR particle series (Figure 1.7) doesn't show any peaks attributable to electronic doping. The only observable peaks in the IR are from the carbon-hydrogen movements associated with the capping ligands. In addition to the SILAR synthesis used above, several other synthetic methods were tried in an effort to produce CdSe nanocrystals with observable optical transitions. These included trying to synthesize much larger particles, 10 nm to 100 nm, varying the temperature significantly, and removing the SILAR method all together and simply adding both precursors to a sample of presynthesized nanocrystal cores. None of these experiments produced any results notably different from those of the traditional SILAR synthesis.

It has been shown experimentally that it is possible to chemically reduce CdSe to show the predicted optical transitions associated with electrons in the conduction band.[24] Similar experiments were attempted using sodium biphenyl. The very high reduction potential of the extra electrons in the nanocrystals made the spectroscopy difficult.

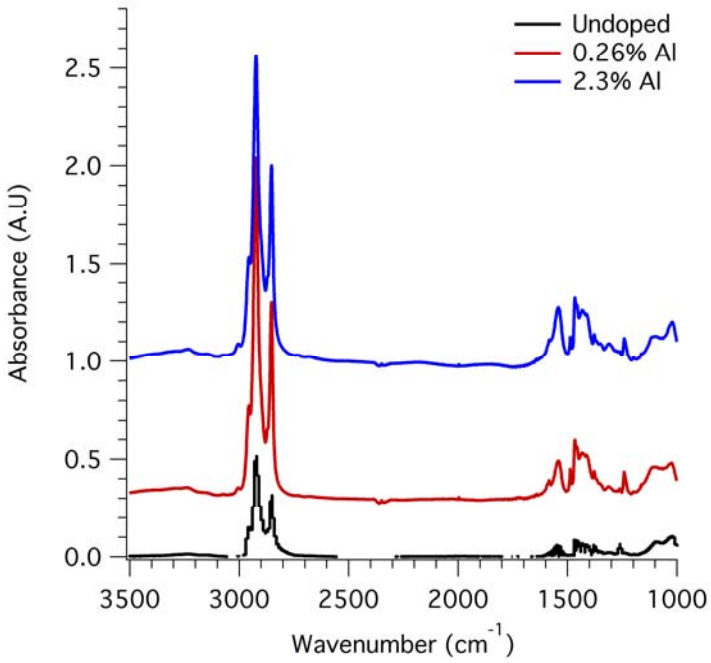

Figure 1.7: IR spectra of the SILAR nanocrystal series. Several spectra removed and the spectra are offset for clarity. Intensity is a function of film thickness on the salt plate and is not relevant.

Other reduction techniques were tried in an effort to reduce the CdSe nanocrystals. They were heated in a 5% hydrogen atmosphere, and in vacuum. They were exposed to a mercury arc lamp while in the IR spectrometer. The same experiment was attempted with the nanocrystals suspended in ethanol. None of these experiments were able to produce any noticeable changes in either the UV-Vis or IR spectral measurements. Similar techniques were used on ZnO nanocrystals, as they are much more stable in regards to having extra electrons in their conduction band. (Figure 1.8) This was to confirm that both our experimental and theoretical predictions were correct, while using a more forgiving system.

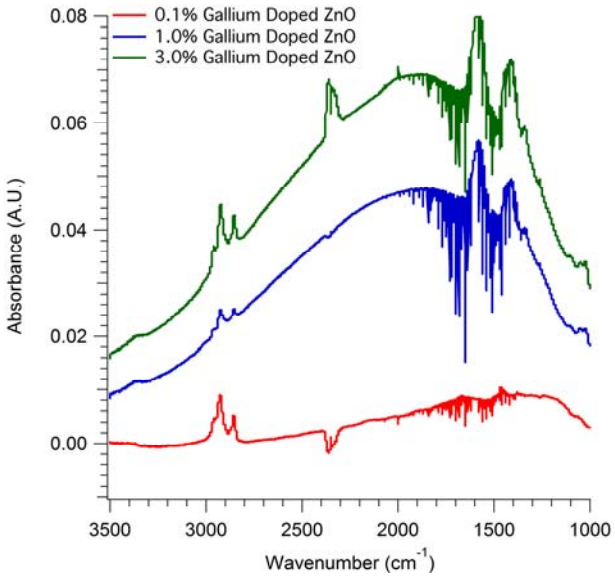

Figure 1.8: IR spectra of several gallium doped ZnO nanocrystal samples. The spectra have had the signal from the undoped sample subtracted from them to better show the signal.

1.4.3 Quantum Yield Experiments: Cadmium selenide is a direct band gap semiconductor, which means light is an excellent method to investigate the electronic structure of the material. Semiconductor nanocrystals as general category are highly luminous, with fluorescence spectra providing complimentary information to the optical absorption spectra.[11, 13, 17, 40, 52-54] However, as previous experiments have demonstrated the quantized nature of the optical spectra is often obscured do to polydisperse samples, and non-uniformity between samples. So rather than looking for specific spectroscopic transitions a more generalized approach may be more useful. Quantum yield is the measure of the number of photons emitted for the number of photons absorbed. So an overall increase in nanocrystal fluorescence is an indication of a change in the electronic structure,

a radiative decay path with a faster decay time than previous non-radiative pathways.

It has been well documented that introducing dopants to semiconductor nanocrystals increases their fluorescence.[14, 17-18, 21-22, 40-41, 55-58] Therefore increased fluorescence would strongly suggest that nanocrystals have been successfully doped. CdSe nanocrystals were doped with group 13 metals and their quantum yield was studied, using rhodamine 6g as a comparison standard. (Figure 1.9). There is an obvious increase in fluorescence as the dopant percentage increases. This is followed by a decrease in fluorescence, though still above the undoped nanocrystals, as the dopant percentage increases further.

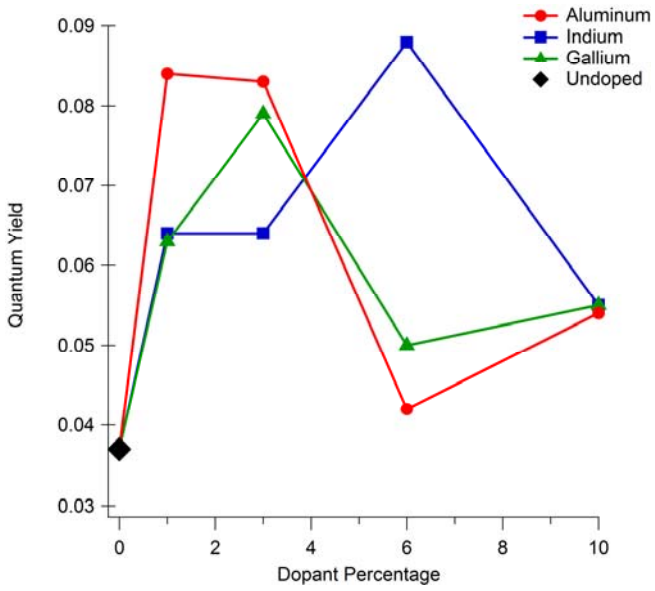

Figure 1.9: Shows the quantum yield of cadmium selenide nanocrystals doped with group 13 metals.

It is possible to say that the dopants are present with the nanocrystals, and that they are interaction with the electronic structure of the nanocrystals. An accurate mechanism for the

fluorescence changing as a function of dopant percentage requires an accurate measurement of the dopant atom's location.

1.4.4 EXAFS Experiments: It has been shown that the dopants added to the nanocrystals are interacting with the electronic structure of the nanocrystal. That doesn't, however answer the question of the dopant's location, and by definition, quantum confinement means that the electronic structure of the nanocrystal extends to at least the surface of the nanocrystal. In order to understand the local structure of the dopant atoms the spectroscopic technique EXAFS will be used. This experiment will utilize just the EXAFS signal rather than the EXAFS and x-ray absorption near edge structure (XANES) signals that make up an x-ray absorption fine structure (XAFS) experiment.

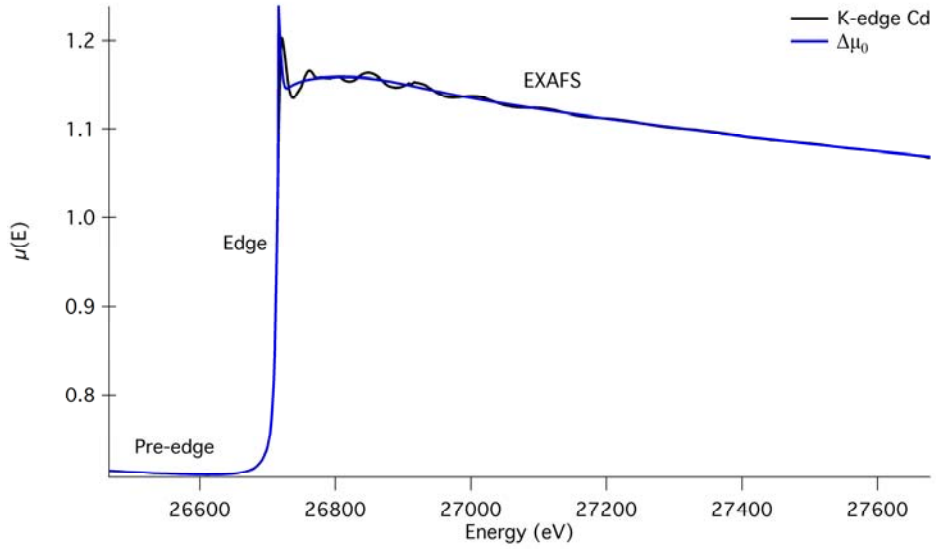

Figure 1.10: An x-ray absorbance spectrum. The black line is the measured K-edge of cadmium. The blue line is the idealized background needed to determine the EXAFS signal. The various regions of the spectra have been labeled.

EXAFS is a form of x-ray absorption spectroscopy. There is a characteristic x-ray absorbance spectrum (Figure 1.10) and the EXAFS signal needs to be extracted from it. The EXAFS signal is defined in equation 1.5, with μ being the x-ray absorption coefficient and μ_o being the idealized x-ray absorption coefficient.[59]

$$\chi(E) = \frac{\mu(E) - \mu_o(E)}{\mu_o(E)} \tag{1.5}$$

The data reduction begins with the removal of the pre-edge region of the graph. This is done by fitting a Victoreen polynomial to it (Figure 1.11a). The edge is then fitted and the edge step is normalized to one (Figure 1.11b). The data is converted to wavenumbers (k-space) as it simplifies the spherical math of the electron scattering. Equation 1.6 demonstrates this conversion, were E the X-ray energy, and E_o is the energy of the X-ray absorption edge. The rest of the background is fitted and removed with a spline function (Figure 1.11c). The remaining data is the EXAFS signal χ(E) (Figure 1.11d-f).

$$k = \sqrt{\frac{2m(E - E_o)}{\hbar^2}} \tag{1.6}$$

When Fourier transformed from wavenumber (k-space, χ(k)) into angstrom (real space, χ(R)) the EXAFS signal takes on a form similar to the radial distribution function; it cannot be treated as one however. There are many scattering paths, both single and multiple, that make up the peaks present in χ(R). Also due to phase shifting of the electron during scattering the distance between scattering shells cannot be quantified without first modeling the data. The function χ(R) can give information regarding number of nearest atoms, bond lengths, and structure disorder. In order to extract that information the data is modeled against the standard EXAFS equation (Equation 1.7).[59]

$$\chi(k) = \sum_j \frac{N_j S_o f_j(k) e^{-2k^2\sigma_j^2}}{kR_j^2} \sin[kR_j + \delta_j(k)] \qquad (1.7)$$

The scattering [f_j(k)] and phase factors [δ_j(k)] are both dependent on atomic number, which will further clarify which atoms are neighbors to the dopant atoms.

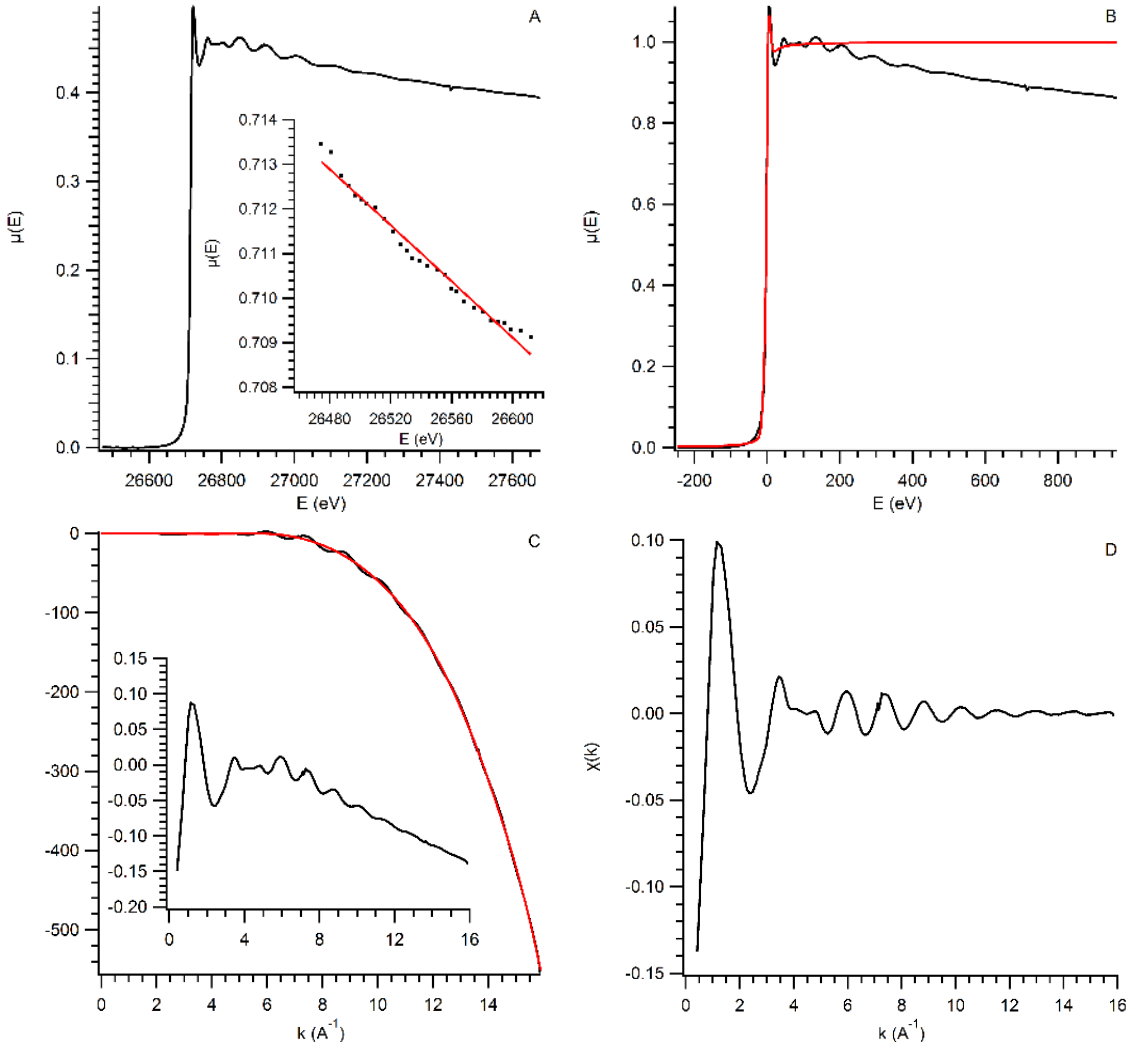

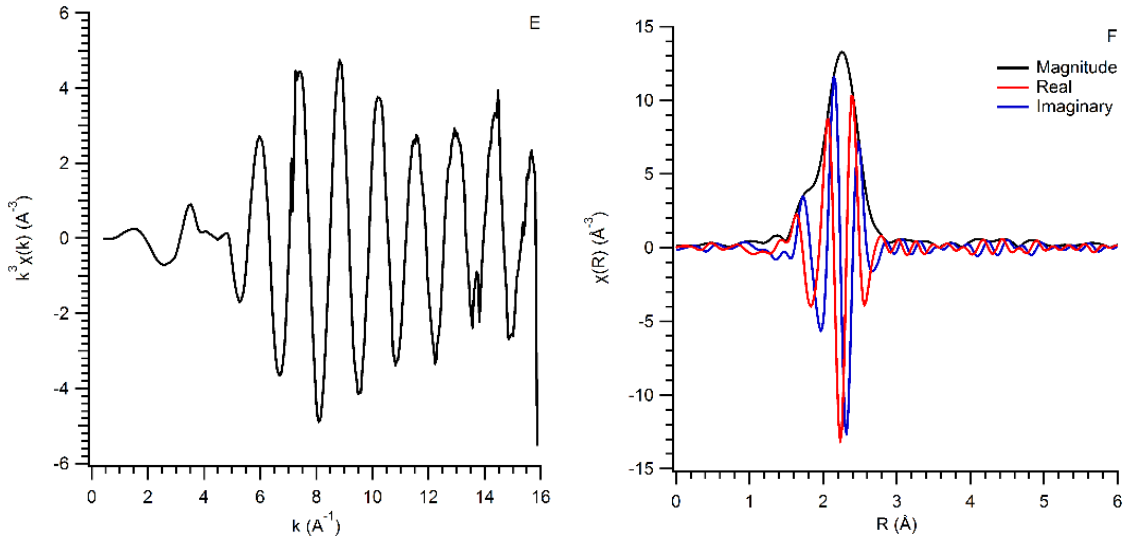

Figure 1.11: Shows the various steps needed to extract the EXAFS signal from the original x-ray absorption measurement. (a) Shows the x-ray signal after the pre-edge region has been fitted and removed. The inset shows the x-ray data (black dots) and polynomial model function used to fit it (red line). (b) Shows the model fitting the x-ray absorption edge (red line) and the x-ray absorption data has been normalized so that the ideal edge height is one. (c) A spline function (red line) is fitted as a background to the data. The data has been transformed from eV to wavenumber and the data shown has been weighted by k^3 this helps to emphasize the EXAFS signal which weakens as a function of distance. The inset shows the same data without the k^3 weight. (d) Shows the extracted EXAFS signal χ(k). (e) Is the same data a (d) but with a k^3 weight. (f) Is the Fourier transform of χ(k). χ(R) has a real and imaginary part. The combined magnitude of which is similar to the atomic radial distribution function.

These two functions are calculated using the commercial software FEFF[60] based on a physical model of the system. The modeling is done using the variables: path degeneracy

(N), amplitude reduction factor (S), path length (R), and the mean square disorder of neighbor distance (σ) from the EXAFS equation (Equation 1.7) and the E_o term from the energy conversion equation (equation 1.6). The starting model for CdSe is the wurtzite phase of bulk CdSe.[61] While this doesn't take into account the surface species and effects of the nanocrystal system. The fitting will show that over reasonable atomic distances (1.8Å-4Å) the bulk phase model does an excellent job of representing the experimental data. Figure 1.12 shows the fitting results for the K-edges of cadmium and selenium. There is very good agreement between the model and the experimental data, the misfit between the two is ~1%. The fitted R term from equation 1.7 is also with 0.1Å of the ideal crystalline

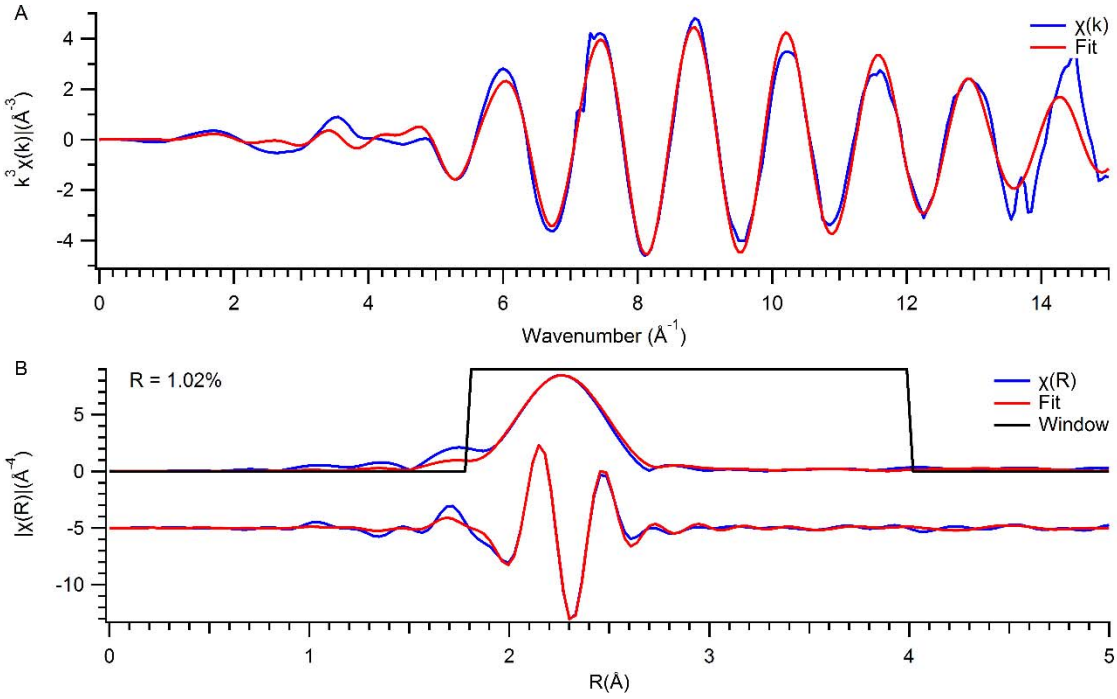

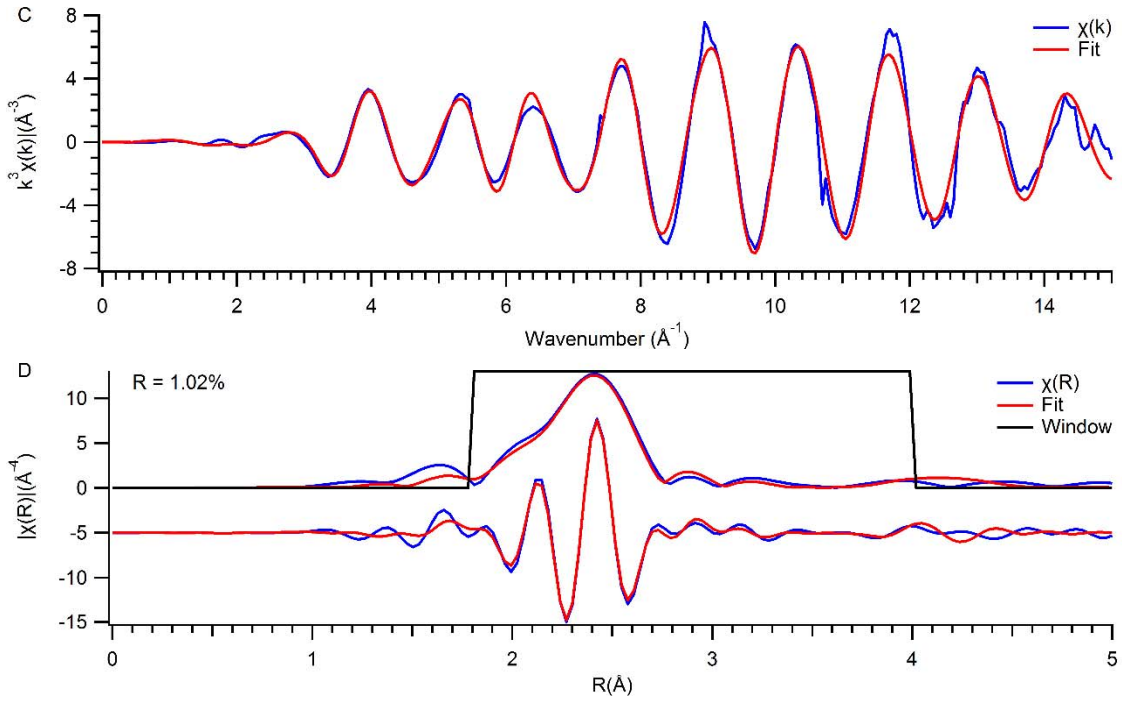

Figure 1.12: Shows the results of fitting hexagonal crystal phase model of CdSe to the experimental EXAFS data. Figure A shows the k^3 weighted X(k) data for cadmium. Figure B shows the R^3 weighted R(k) data for cadmium. The upper trace is the magnitude of R(k) and the lower traces is the real component of R(k). The black line is the window over which the data was fitted in R-space. The fit (red lines) shows very good agreement with the experimental data (blue lines) in both magnitude and phase. There is only a 1% mismatch between data and model over the fitting window. Figures C and D repeat the figures A and B respectively but for the selenium data.

value.[61] This demonstrates that even a first approximate approach to fitting the experimental data works very well. This greatly simplifies the fitting process, as there is no straightforward way to model disorder in fitting EXAFS data.

Throughout this project, CdSe nanocrystals have been doped with group 13 metals.

The EXAFS experiments used gallium, as the x-ray beamline wasn't able to go low enough in energy measure the K-edge of aluminum and indium is next to cadmium on the periodic table, so both K-edges overlap. There are several possible locations for the gallium atom to incorporate in the crystalline structure. The ideal location would be the direct replacement for a cadmium atom, accomplishing the idealized n-type doping where an atom is replaced with an atom with one more electron. The gallium atom could also be incorporated into an octahedral or tetrahedral hole in the crystal. The final possibility is that the gallium atom is bound to the surface of the nanocrystal. Each of these possibilities can be modeled and fitted to the EXAFS data, and the results are in figures 1.13 and 1.14.

The direct replacement of cadmium by gallium model represented in figure 1.13A-B is the first and least representative model. Not only is there a large misfit between model

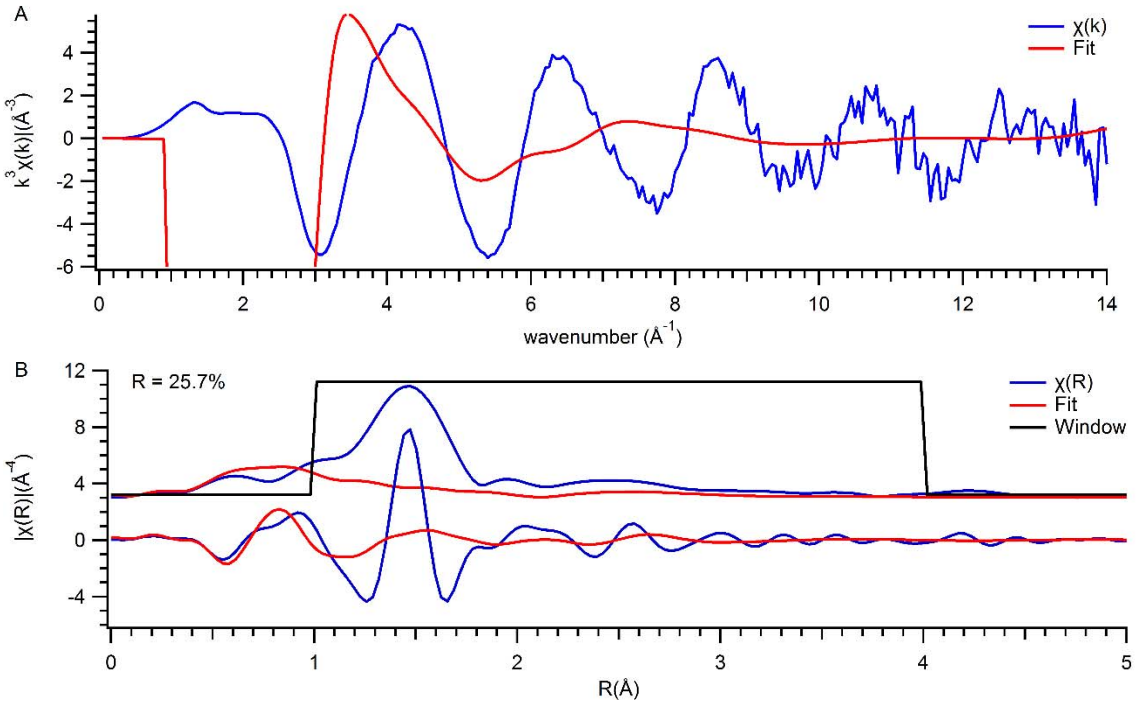

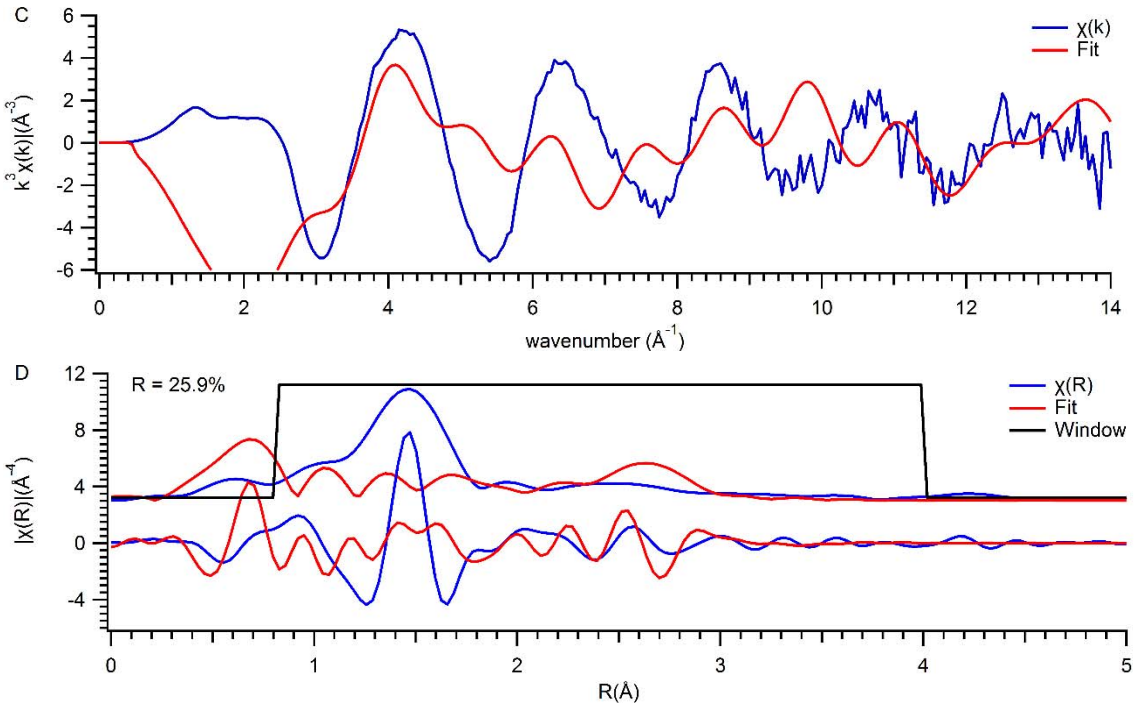

Figure 1.13: Shows the results of fitting two different models, for different positions of a gallium atom, to the experimental EXAFS data. Figures A and B are for the replacement of a cadmium atom with a gallium atom. Figures C and D are for the gallium atom in an octahedral hole in the crystal structure. Figure A shows the k^3 weighted X(k) and figure B shows the R^3 weighted R(k) data for cadmium replacement model. In figure B the upper trace is the magnitude of R(k) and the lower traces is the real component of R(k). The black line is the window over which the data was fitted in R-space. Figures C and D repeat the figures A and B respectively but for the octahedral hole model.

and data but the model fails to follow the data in either k or r space. A quick comparison between the cadmium and selenium K-edge data (figure 1.12) and the gallium K-edge data (figure 1.13) show that the nearest atom (first peak in R-space) to gallium is much closer that the nearest neighbor to cadmium which prevents gallium from being a direct replacement for cadmium. This problem, of the gallium nearest neighbor being closer than

the gallium-selenium bond distance, prevents the octahedral hole model (figure 1.13C-D) and the tetrahedral hole model (figure 1.14A-B) from being correct as well. The large mismatch (R) between the model fit and the experimental data reflects this as well. The final model is of a gallium atom being attached to the surface of the nanocrystal. In that model the nearest neighbor is the head group of the surfactants that are bound to the nanocrystalline surface. As would be expected the gallium-oxygen and gallium-nitrogen bonds, from TOPO and HDA respectively, would be much shorter than the gallium-selenium bond. This is reflected in the much better fit of this model compared to the other models. The structure and phase factors used in the EXAFS equation (equation 1.7) give

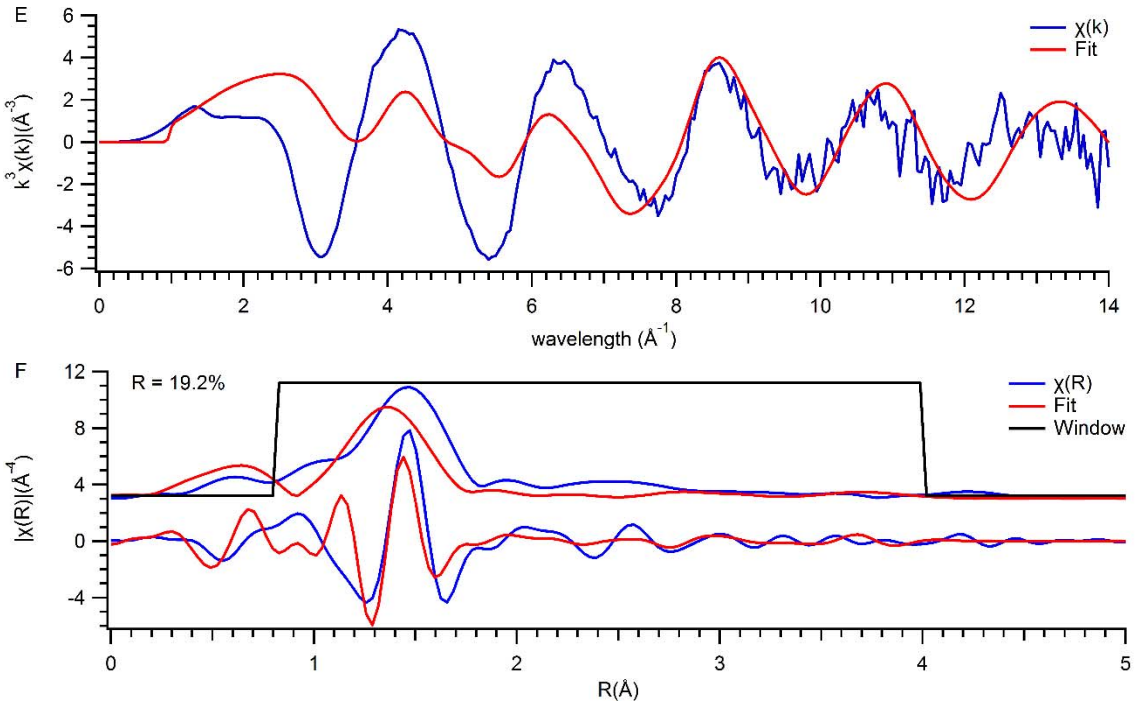

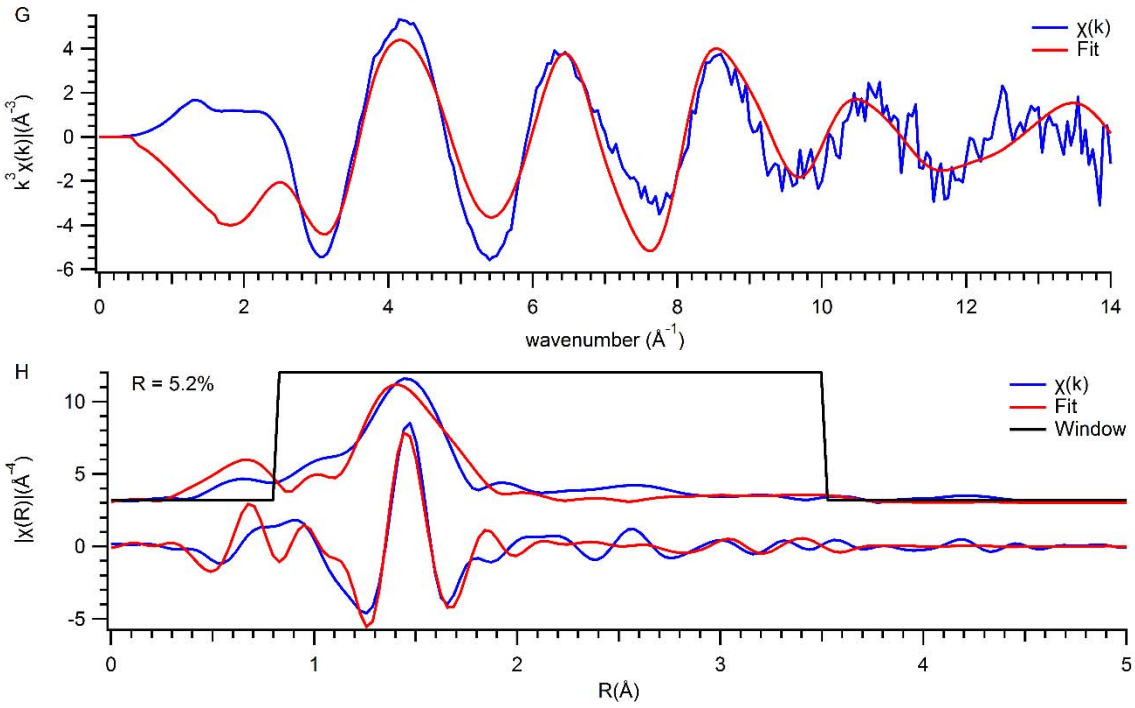

Figure 1.14: Shows the results of fitting two different models, for different positions of a gallium atom, to the experimental EXAFS data. Figures E and F are for the gallium atom in a tetrahedral hole in the crystal structure. Figures G and H are for the gallium atom bound to the surface of the nanocrystal. Figure E shows the k3 weighted X(k) and figure F shows the R3 weighted R(k) data for the tetrahedral hole model. In figure F the upper trace is the magnitude of R(k) and the lower traces is the real component of R(k). The black line is the window over which the data was fitted in R-space. Figures G and H repeat the figures E and F respectively but for the surface bound gallium model.

further evidence of a gallium atom bound to the surface of the nanocrystal and coordinated the surfactant capping ligands. Figure 1.15A shows the structure factors of selenium, oxygen, and nitrogen compared to the measured gallium EXAFS data. Oxygen and nitrogen are much better representations of the nearest neighbor to gallium. It is worth

noting that the selenium structure factor is a reasonable representation for the second nearest neighbor of the gallium EXAFS spectrum. Amplitude reduction in the EXAFS spectrum is the result of structural disorder which would be expected from an environment such as the surface of a nanocrystal. Figure 1.15B shows the phase factors of selenium, oxygen, and nitrogen compared to the measured gallium EXAFS data.

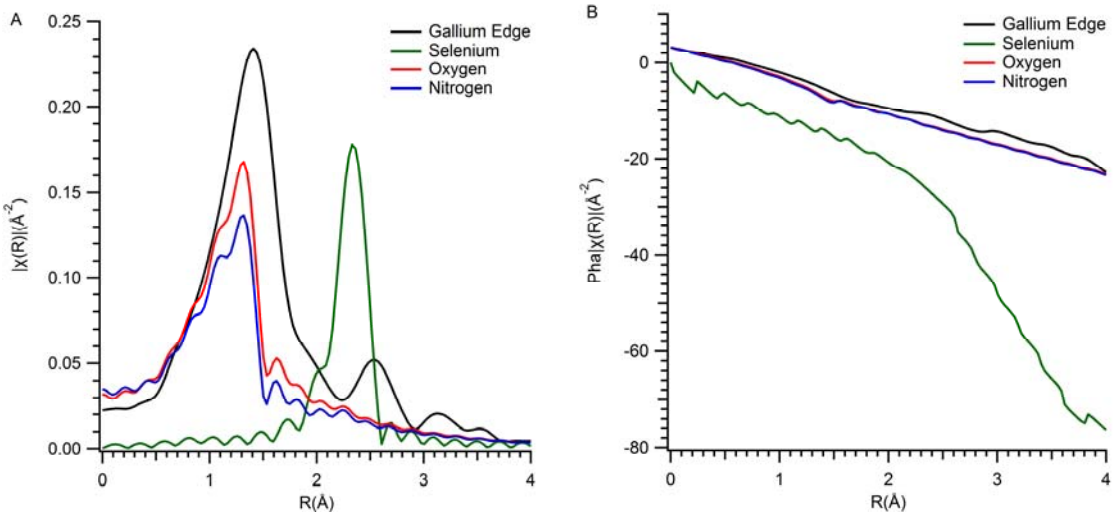

Figure 1.15: Figure A shows the structure factors of the possible nearest neighbor atoms compared to the measured gallium EXAFS spectrum. Figure B shows the phase factors of the possible nearest neighbor atoms compared to the measured gallium EXAFS spectrum.

As with the structure data oxygen and nitrogen are much better representations that selenium. The combination of the structure and phase factors, along with the reasonable fit of the surface model shows that the gallium atoms are bound to the surface of the CdSe nanocrystals and are coordinated with the surfactant capping ligands.

1.5 Discussion: Dopant atoms have been added to the cadmium selenide nanocrystal systems, they are not however incorporated into the crystal lattice. Instead they are bound to the surface of the nanocrystal, coordinating with the surfactant capping

ligands present there. The dopants are present as both the ICP-MS and EXAFS experiment detect their presence in concentrations expected based on the amounts added during the synthesis. Apart from being present the dopants don't have a strong effect on the overall nanocrystal system. The XRD spectra (figure 1.6) show no structural changes expected from a large amount of dopant atoms being incorporated into the nanocrystal. The optical spectra as well (figures 1.5, and 1.7) don't show any changes attributable to anything other than differences in nanocrystal diameter and size distribution between samples. Electronic doping of nanocrystals usually results in bleaching of observed transitions, or the filling in of predicted transitions.[14, 22, 24] Dopants also cause the rise in deep trap state emissions.[62] None of these effects are seen in these nanocrystal samples. The EXAFS (figures 1.13, 1.14) shows that the gallium dopant atoms are bound the surface. The nearest atom distance is less than 2 angstroms, too short to be either Ga-Cd or Ga-Se bond. The structure and phase components of the EXAFS equation (figure 1.15) are also consistent with the gallium atoms being closest to the nitrogen and oxygen atoms of the surfactant capping ligands. The quantum yield data (figure 1.9) is more complicated. There is an increase of quantum yield with increasing doping suggesting that the dopants are present with the nanocrystals. The amount of increase isn't linear, the quantum yield decreases to just above the undoped sample as the dopant load increases.

Semiconductor nanocrystals have complicated surfaces, so any interaction with them is going to produce complicated effects. The surfactant capping ligands, TOPO[9] and HDA[34], were used initially to slow down the nanocrystal grow and to focus the size distribution. However it was soon noticed that these capping ligands dramatically increased the fluorescence of the nanocrystals. It has been shown that the extra electron density from

these ligands helps to passivate the surfaces of nanocrystals, by filling in trap states, coordinating to dangling bonds, and filling localized orbitals. These surface states act as electron traps, allowing for non-radiative recombination, effectively quenching nanocrystal fluorescence. Later efforts expanded on this "capping" of the surface by over coating the surface entirely different semiconductors.[34, 36, 45, 47, 63] This addition of electron density to the nanocrystal surface to increase fluorescence explains the observed quantum yield effects. At low concentrations the dopant atoms fill surface sites left vacant by the capping ligands, effectively increasing the fluorescence. As the doping levels increase the dopant atoms begin to insert themselves between the surface and the capping ligands. The dopants are trivalent cations which drain away electron density from the surface. They themselves can also act as recombination centers. These effects increase as the doping percentage increases, and are responsible for the decreased quantum yield as the doping percentage increases.

Along with the experimental evidence there is computational evidence to support the idea that the dopant atoms are bound to the nanocrystalline surface. In order for a dopant atom to be incorporated into the nanocrystal the binding of dopant needs to be more energetically favorable than the increase in energy resulting from the impurity incorporation. It was calculated that the binding energy of dopant atoms on the (001) face of a zinc-blende (cubic) structure are increased by a factor of 2 to 10.[15] This explains why the early doping successes were in cubic systems such as ZnSe[19] and ZnS[18] and why early attempts to dope CdSe (hexagonal) were unsuccessful.[14]

More indirect evidence for the failure of this doping method is that later, successful methods no longer use the two precursor, surfactant mediated hot-injection methods.

Methods such single precursor source[64-65] and dopant exchange and substitution[66-67] overcame the problems associated with this original doping method.

1.6 Conclusion: Cadmium selenide nanocrystals were synthesized using several methods. These methods were adapted by adding group 13 metals to the synthesis in an effort to electronically dope the nanocrystals. The dopants were not successfully incorporated into the nanocrystal. They are instead bound to the surface of the nanocrystal. However, their location, local bonding environment, and overall effect on the nanocrystal has been successfully studied using a variety of methods.

Chapter 2:

2.1 Introduction:

2.1.1 Background: Atomic layer deposition (ALD) reactors are used to deposit thin layers of material on a substrate. As with any deposition process there needs to be control over the introduction of precursor material into the reactor in order to control the final thickness and composition of the material being deposited.

While the mechanisms behind the reactions involved in ALD are more complicated and will be discussed in greater detail in the next chapter, the overall concept is simple. A precursor is introduced into the reactor, allowed to interact completely with the substrate. The excess is removed via vacuum exhaust pumps and inert purging gas. Then the cycle is repeated with the next precursor material. By controlling the materials being introduced and the number of cycles being performed very fine control over final composition and film thickness can be achieved.

It should be obvious from the simplified mechanism that the selection of the precursor materials is critical for the successful deposition of the desired material. A precursor requires several properties in order to be useful in ALD systems. The precursor must be reactive enough to quickly cover the substrate. The precursor needs to be volatile enough to readily enter the gas phase for transport through the reactor. Finally, the precursor needs to be stable enough to remain intact as it moves through the reactor. It also must be stable enough to be safely handled. The ALD reactor itself imposes a few quite strict limitations on the precursor selection, which is the reasoning behind the construction of a new ALD reactor.

Traditionally, gas flows throughout the reactor are controlled with mechanical valves. This imposes two equipment based constraints on precursor selection. First, the valves restrict gas flow through them. This puts a lower limit on the volatility of the precursor. Secondly, the valves have temperature working limits. This puts an upper limit on the temperature that can be used to increase the volatility of the precursor into an acceptable range.

These two limits on volatility restrict traditional ALD reactors to the use of liquid precursors. Unfortunately, many of the organometallic precursors that are mechanically compatible with the reactor equipment are hazardous to work with. Nearly all of them are toxic and many of them are pyrophoric; they ignite spontaneously upon contact with air. Some are so reactive that they break down while being moved through the reactor. They deposit material on the lines leading to the reactor rather than on the desired substrate.

Replacing liquid ALD precursors with solid ALD precursors would eliminate nearly all of the problems mentioned for liquid ALD precursors, and as such are hugely advantageous. Solid precursors are almost always much more stable than liquid precursors for depositing the same material. This increase in stability leads to solid precursors being traditionally cheaper to manufacture. It also leads to solid precursors being less reactive which means they are safer and easier to work with. They typically don't require the sealed or air-free conditions that liquid ALD precursors do.

Despite their numerous advantages solid ALP precursor have one main disadvantage, low volatility. This can be overcome by heating the precursors to higher temperatures and using higher carrier gas flow rates. These higher temperatures also serve to increase the reactivity of the more stable solid precursors. However there is an upper

limit to both the precursor temperatures and flow rates. The mechanical valves responsible for controlling the introduction of the solid ALD precursors into the reactor can only handle so high a temperature and so large a flow rate. These limits are nearly always much lower than what is required to use solid ALD precursors.

The obvious thing to do would be to remove the mechanical valves, but there still needs to be a way to control and direct the necessary gases throughout the reactor. One solution to this problem, and the one that will be used in this construction is inert gas valving. Flows of inert gas are used to create pressure barriers. These pressure barriers act as a closed "valve". This barrier can be removed by changing the flows of inert gas, allowing the "valve" to open.

The design of this system was originally patented in 1983[68]. Several of the reactor dimensions were taken from this patent. The overall design of the reactor is similar to the design diagramed in the patent. Though there are some differences to account for the specific design considerations of this construction.

2.1.2 Design Considerations: Many of the design choices made in the course of construction were made in order to conform to the following considerations and limitations placed on the design. The first, and most important, was the overall cost. The project had a grant of a few tens of thousands of dollars. This was one to two orders of magnitude less than the cost of a commercial instrument. The need to keep costs as low as possible, especially considering many of the needed components have fixed prices that can only be worked around influenced several design choices. As many components as possible had to be "off the shelf." This reduced cost as these items are usually cheaper, being massed produced. It also removed the need for expensive custom machining. However, there were

several advantages to this method of construction other than just cost reduction. The lack of customization means that these parts were, and are readily available, having no lead time for their construction. They are also replaceable, especially by researchers who may not be familiar with the overall system. Replacements can be easily swapped in for damaged or defective parts. This "off the shelf" philosophy extends to the construction materials as well. Unless there was a good reason to do otherwise, all materials are commercially standardized and available: material composition (i.e. 304 and 316 stainless steel), lengths, thicknesses, thread pitch, etc. Again, this minimizes expensive custom machining and allows for easy part procurement and replacement.

Second, the reactor needed to be able to use both solid and liquid precursors. This was accomplished by using an inert gas valving system for the solid precursor and a traditional vacuum draw system for the liquid precursors.

Third, the reactor needed to be able to deposited material on standard 2 in diameter silicon wafers. The materials to be deposited by the reactor are semiconductors and electrical measurements are important characterization tools for these materials. These measurement are difficult on the ~1 cm sample pieces produced in a standard 25.4 mm diameter reactor.

Finally, the reactor need to be user friendly and accessible to novice users. Many custom instruments, especially those constructed on academic budgets tend to esoteric in their operation. Cobbled together would be an accurate description. The design therefore makes use of several automation controllers and simplified user interfaces to minimize the amount of instruction needed to operate the reactor.

2.2 Solid Precursor Reactor Construction:

2.2.1 Introduction: The rest of this chapter will detail the construction of each of the varying subsections of the ALD reactor. Any necessary graphics will be included in the section. Any of the required technical diagrams used in the construction will be included at the end of this chapter. A bill of materials will also be included in the end of the chapter.

2.2.2 Precursor Delivery Systems: There are several precursor delivery systems in this reactor, two for solid precursors and two for liquid precursors. These precursor systems, as well as the gas delivery systems all feed into a manifold at the front of the reactor (Figure 2.1).

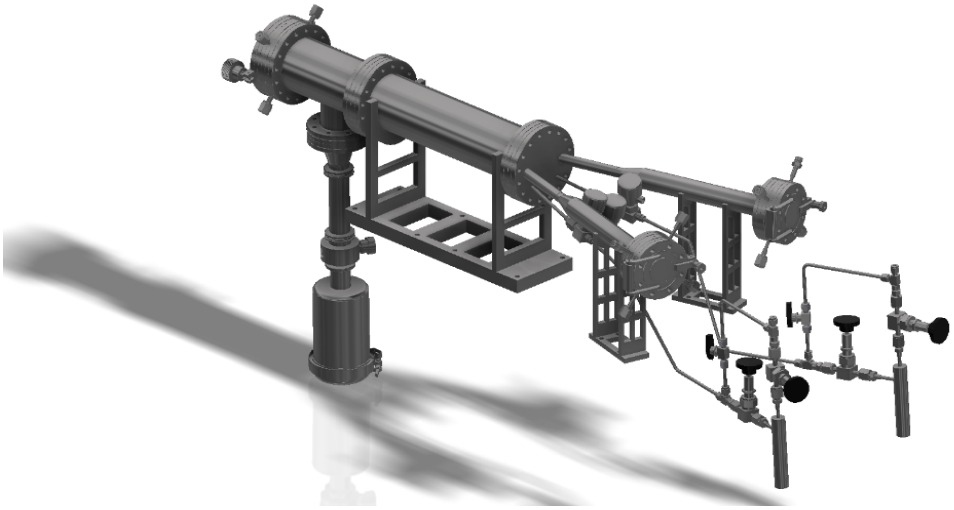

Figure 2.1: A rendered simplified model of the overall reactor. The solid precursor delivery system are the twin metal arms on the right side of the model. The liquid precursor delivery system is the pair of metal cylinders below the solid precursor

The liquid precursor system consists of a simple stainless steel bubbler with inlet and outlet valves (Figure 2.2, Diagram S1). Nitrogen gas can be bubbled through the precursor to help improve its volatility. The precursor delivery into the main reactor is controlled by a

standard pneumatic valve between the precursor vessel and the main reactor (Figure 2.1). The solid precursor system consists of a glass cylinder that holds the precursor and controllers the gas flows needed to establish the necessary pressure gradients in order for the "valve" to work (Figure 2.3, Diagram S2).

Figure 2.2: Liquid precursor vessel. Hand valves are needed to seal the precursor for filling as many of the precursors are pyrophoric. Quarter turn valve (far left) can be used as a gas bypass of the precursor vessel if needed.

This glass cylinder is placed inside of a stainless steel cylinder that contains the vacuum and is externally heated (Diagram S3).

Figure 2.3: Solid precursor system glass inner sleeve. The precursor is placed in an open alumina boat shown above.

The mechanism of action is based on using a plug of N_2 gas as a "valve". Figure 2.4A. shows a cut away of one of the solid precursor delivery systems. The solid precursor (blue) is in an alumina boat that is inserted into the glass precursor sleeve. (Figure 2.3). The glass sleeve is inserted into the stainless steel sleeve where it is pumped down to system vacuum and heated externally. The precursor begins to sublime. Figure 2.4B shows how the system works when the "valve" is "closed". N_2 gas flows between the glass and stainless steel sleeves (red lines). The gas is pulled towards the left side of the precursor vessel and exhausted by the main system vacuum pump. Simultaneously the gas is pulled towards the right side of the precursor vessel and exhausted by the precursor vacuum pump. This creates a plug of N_2 gas that prevents the solid precursor from entering the reaction zone and functions as a "closed valve". The flow of N_2 across the precursor boat causes the sublimed precursor to flow towards the right side of the precursor vessel. Since the end of the vessel isn't heated this causes the sublimed precursor to deposit on the walls of the glass precursor sleeve, where most of it can be recovered. This also prevents the solid precursor from being exhausted by and potentially damaging the precursor vacuum pump. Figure 2.4C shows how the system works when the "valve" is "open". An additional stream of N_2 gas is pulsed into the rear of the glass precursor vessel. This overcomes the standing plug of N_2 gas and pulses the sublimed solid precursor into the reaction zone.

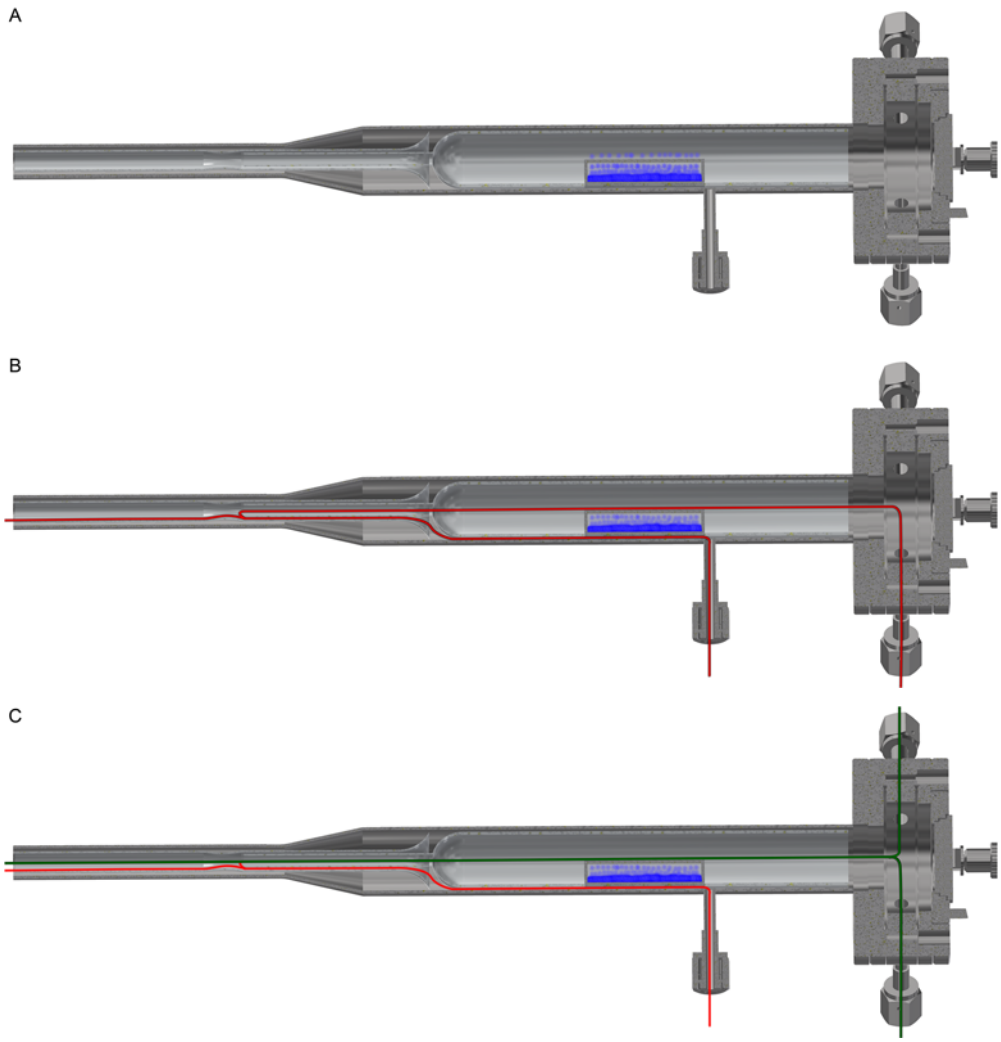

Figure 2.4: Figure A is a cut-away of one of the solid precursor delivery systems. Figure B is a depiction of the system in the "valve closed" state. The red lines represent the flow of N_2 gas. Figure C is a depiction of the system in the "valve open" state. The green lines represent the flow of the new stream of N_2.

The final precursor delivery system is for delivering gases. It is controlled by a pneumatic valve (Figure 2.1, central of the 3 pneumatic valves, between the solid precursor lines).

2.2.3 Reaction Zone and Sample Stage: The main body of the reactor is taken up by the

reaction zone.

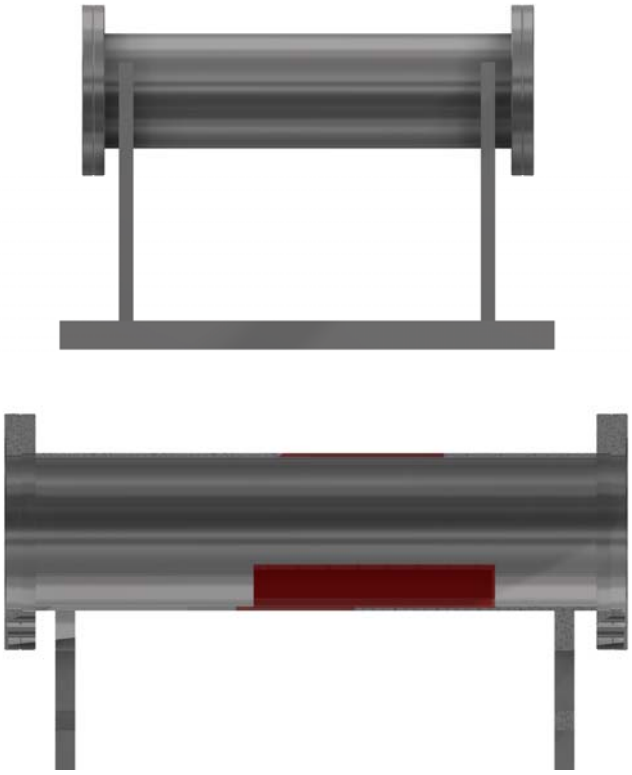

Figure 2.5: The top images shows the reaction zone, without the external heaters. It is sitting on its support cradle. The bottom image is a cut away of the reaction zone. The sample stage has been colored red for clarity.

This is the portion of the reactor where the precursors react with the sample substrate in order to deposit materials. This is also the main structural component of the ALD reactor. All of components of the reactor bolt to the reactor zone. The reactor zone is supported by a stainless steel cradle that acts as the structural base of the reactor (Figure 2.5, Diagram S4, Diagram S5). The reaction zone is made up of a stainless steel tube that is heated externally (Figure 2.5, Diagram S6). This section is heated independently of the precursor

delivery sections. The reaction zone is usually at a higher temperature than the precursor sections as precursor reactivity and decomposition are desired in this section, but not in the precursor delivery sections. The sample stage is a section of a cylinder cut length wise (Figure 2.6, Diagram S7). It is made from the same diameter stainless tubing as the reaction zone.

Figure 2.6: The sample stage for the ALD reactor. The top has been drilled and tapped for screws.

However, the tubing is twice the thickness as the reaction zone tubing. It was turned down on a lathe to the correct diameter to be a close fit to the reaction zone tube. Since the reaction zone is heated externally a close fit is important. The stage has a thick top plate to ensure temperature consistency and uniformity. The top plate is drilled and tapped to allow for easy attachment to the sample stage. There is also a thermocouple connected to the sample stage, so that sample temperature is accurate, as the reactor is being heated externally.

2.2.4 Exhaust System: The final major component of the solid precursor ALD reactor is

the exhaust system. It consists of two vacuum pumps and their associated traps. The first is a 48 m^3/h rotary vane pump. This is the main system pump, and is responsible for keep a low base pressure and exhausting the excess ALD precursors. The pump is protected by a particle trap, to help catch and leftover solid precursor and a cold trap. ALD precursors are very reactive, and can break down and polymerize pump oil, so the cold trap prevents damage to the pump oil and by extension the pump. The second vacuum pump is a 16 m^3/h rotary vane pump. It is responsible for applying vacuum to the ends of the solid precursor lines to establish the necessary gas flow conditions. As it is handling a much lower gas flow rate, a simple cold trap protects the pump.

2.3 Auxiliary ALD Systems:

2.3.1 Heating System: A large portion of ALD research requires careful temperature control. ALD processes function differently, if at all, depending on temperature. Precursors need to be temperature controlled to ensure their volatility is in the correct range. Obviously a heating system is needed, and in order to ensure uniformity it should be tightly, and actively controlled. Unfortunately there is no easy solution to this problem. The reaction zone of the reactor is based on a very common ALD reactor design, the hot-wall tube reactor. These have the advantages of being both simple to design and heat. Tube furnaces are inexpensive and easily controlled. This reactor doesn't easily lend itself to being heated in this way. Three separate furnaces would be expensive, and there isn't physical room for all of them, assuming units could be found that would be accommodating of the various shapes of this reactor. The solution employed is to use band heaters. These are easy to install, as all of the major components of the reactor are tubes. They are also an off the shelf part, so in the eventuality of fail they are much easier to replace that if a more custom

heating solution was employed. Also the separation of heater from controller allows for one controller and power system. This simplifies construction and improves ease of use. Thirteen heaters are used. Four for each of the solid precursor lines and five for the reaction zone.

Both the heat controller (Figure 2.7, Diagram S8) and power supply had to be assembled (Figure 2.8), as manufactured units were outside the budget of this project. The heart of the heat controller is a commercial heater microcontroller. It accepts thermocouple inputs and sends out controller signals to the larger power handling components of the power supply. It also comes with a learning algorithm. It varies the power output to see how the system load changes in response. It results in an extremely well controlled system. Over a twelve hour ALD process the temperature of each zone varies ~0.25°C from the set point. It is equipped with an external LCD display and user interface. This was installed in a custom 19in enclosure with the rest of the ALD reactor control systems (Diagram S8). The controller measures three different thermocouple inputs, one for each zone. The two solid precursor lines have their thermocouples attached to the outside of the stainless steel tubes. The reaction zone thermocouple is spot welded to the sample stage.

The heaters for this reactor have a total combined power rating of 5kW. No controller is going to be able to provide the power needed. There needs to be separate power supply. This translates the controller signal, typically 5-24 Vdc, to the much larger mains voltage, in this case 240 Vac. It should be obvious that a system with this much power, that safety needs to be paramount in its construction. There are two important safety consideration in play.

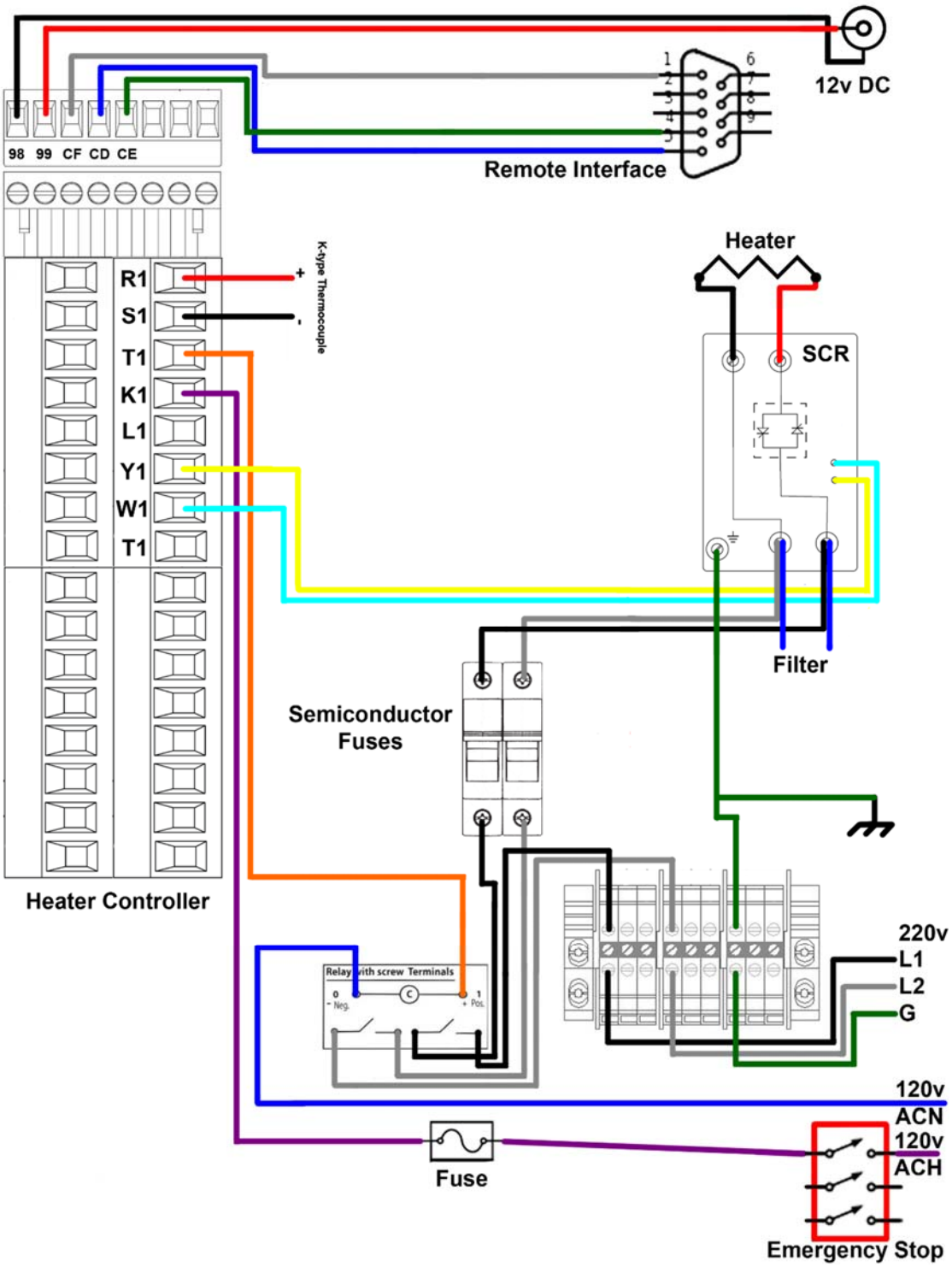
12v DC
98 99 CF CD CE
Remote Interface
Heater
SCR
K-type Thermocouple
+
-
R1
S1
T1
K1
L1
Y1
W1
T1
Filter
Semiconductor
Fuses
Heater Controller
220v
L1
L2
G
120v
ACN
120v
ACH
Fuse
Emergency Stop

Figure 2.7: Is a simplified electrical schematic of the heater power supply. There are three separate heating zones on the ALD reactor, therefore there are three separate heating circuit in the power supply. The section of the heater controller marked with letter inputs (example R1) is repeated for two other sections of the controller (example R2). The thermocouple, SCR, heater, filter, semiconductor fuses, and relay are all tripled in the final power supply. The power supply accepts input from the remote interface on the heater controller. It also accepts two power inputs, a 220v-15A connection and an 110v connection.

The first is electrical safety, which is solved by following established electrical wiring practices, placing the system in a grounded enclosure, and minimizing exposed high voltage contacts. The grounded enclosure ensures that any voltage source coming in contact with the enclosure trips circuit breakers, and blows internal fuses. This prevents electrical shock, and system damage. Minimizing exposed high voltage contacts means that even if someone were to enter the electrical enclosure while it was energized there is nothing they could contact that would result in electrical shock.

The second safety consideration is understanding and planning for system failure. In order to prevent run-away heater operation the system needs to be designed in such a way to fail closed. Any failure of the control circuit should result in all power being removed from the heaters. This fail closed design is implemented in several stages throughout the power supply design. The main power components are three silicon controlled rectifiers (SCR). These are solid state devices that don't suffer from the mechanical wear and potential contact fusing problems of mechanical relays.

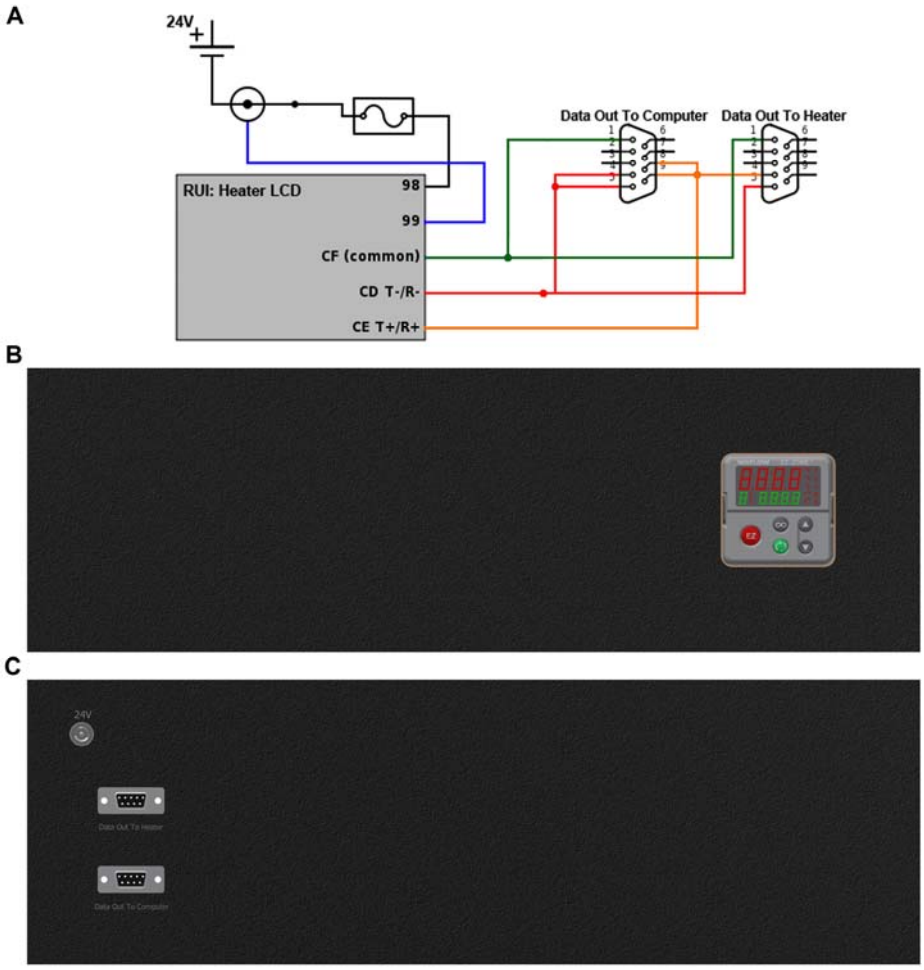

Figure 2.8: Figure A shows the electrical schematic of the heater controller. Figures B and C are computer rendered images of the custom front and back panels, respectively.

They are also an inherently fail closed design. Unless there is a continuous voltage applied to the gate no current can flow through the SCR. Before power can be fed to the SCRs the main voltage passes through a set of mechanical relays. These relays again need to be constantly held open by the microcontroller. Any loss of power to the microcontroller would close the SCRs, preventing current flow. It would also close the relays that allow power to get there in the first place. The final control mechanism is the voltage needed to

open the mechanical relays passes through a latching mechanical switch. In the event of any problems with the heat system, pressing this switch will cut power to the relays, thus cutting power to the rest of the system. This switch will remain in that state until manually reset.

2.3.2 Power System: In addition to the main systems, there are many smaller systems and components of the ALD reactor that need power, all of the mass flow controllers, the electronic solenoid valves for actuating the pneumatic valves, and the system lighting to name a few. All of the subsystems of the ALD reactor were chosen such that they would run on either 12 Vdc or 24 Vdc, simplifying the power requirements. While many of these devices can operate with an AC to DC wall power adapter, having a dozen of them plugged in around the ALD reactor would be cumbersome and unsafe. A better solution is to have one central 12Vdc and 24Vdc power supply and powering each device off that. A custom 19in 3U enclosure was designed to hold the two power supplies (Figure 2.9, Diagram S9). Switches were wired to the front of the enclosure to allow ease of use when turning the various systems on and off.

2.3.3 Computer System and LabVIEW: While other systems on the ALD reactor benefit from having a computer controller, the controllers are not necessary. However, it would be impossible to perform ALD deposition without a computer controller to run the valves. The computer is a standard Windows PC (x64) that is mounted on the 19in rack with the rest of the accessory systems. National Instruments LabVIEW was chosen as the programing language for the operations. The LabVIEW environment has several important advantages over more traditional programing languages for this application. It has an easy learning curve for simple applications, which is important for future usability of the code.

Necessary hardware interfaces can be purchased from National Instruments. LabVIEW is well supported by the scientific instrumentation communities. These two facts mean that most of the necessary hardware code is already written and just needs to be reused in the current application. The PC is equipped with three separate National Instruments hardware cards, a 16 input, 16 output 30Vdc industrial digital communications card for running the valve assembly, an eight RS485 port serial card for data acquisition from the peripherals, and an X-Series digital to analog converter for acquisition of other signal data.

There isn't room, or need, to give a complete treatment of the LabVIEW code. It was coded in accordance with established best practices. However it bears explaining the main portion of the ALD code, the code responsible for the operation of the valve system. The ALD code takes a table of values and converts that table into a series of valve movements. The table represents a series of steps in one ALD cycle, with each row being a single sub step. Each column represents a position on the valve controller, or by extension a valve. The ALD code the runs a series of nested FOR loops, a loop that runs a given number of times. Each loop parses a different portion of the ALD table. The first loop reads the number of rows in the table, the number of sub steps in the ALD cycle.

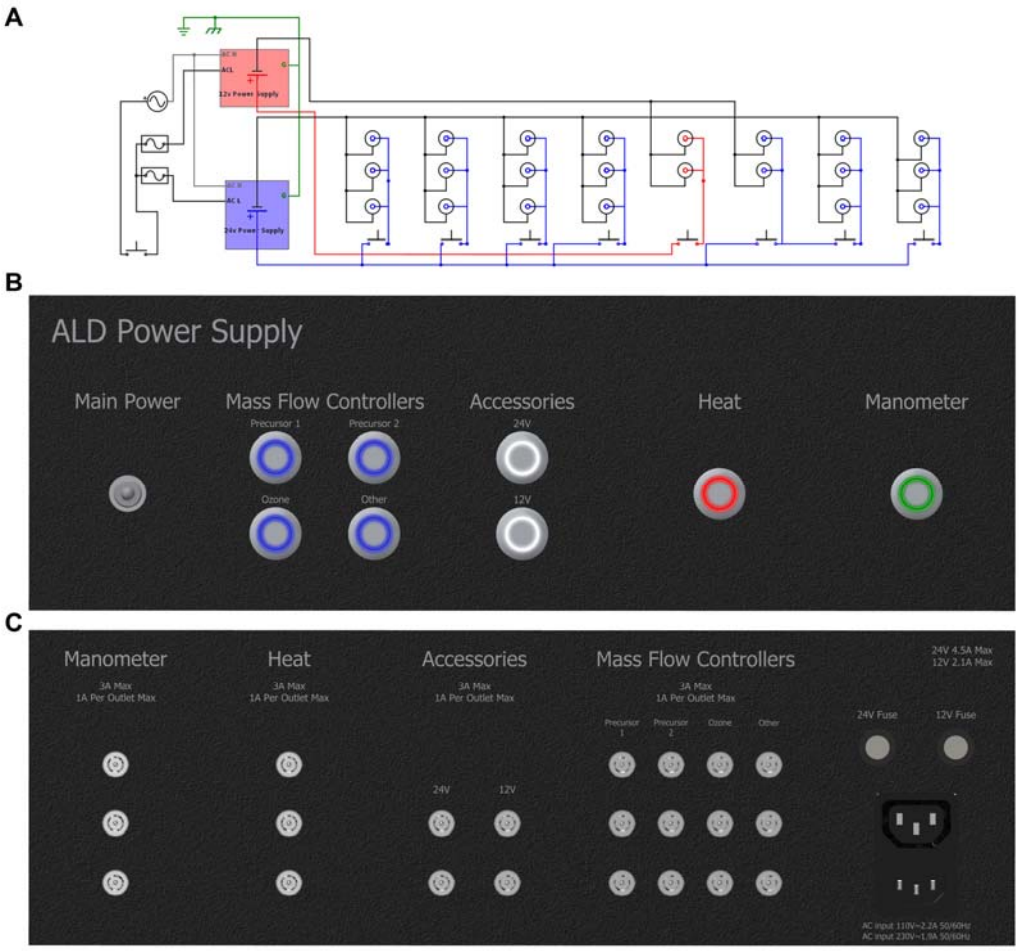

Figure 2.9: Figure A shows the electrical schematic of the ALD power supply. Figures B and C are computer rendered images of the custom front and back panels, respectively.

The second loop reads the number of columns, the number of valves in system. The third loop reads the value in the cell, the number of times the valve needs to open and close. There are two advantages to operating the control code this way. First, it's easy to implement and understand. Second it's flexible and extendable, based on the inputs given to it. The user can pick whatever valve and cycle scheme is needed for their experiment and the code will operate without needing to be reprogrammed between experiments.

Finally, it prevents accidently opening multiple valves simultaneously, as each step in the operation is sequential.

2.4 ALD Reactor Testing: Preliminary testing of the ALD reactor proceeded as expected. During and after construction each component and subsystem was tested to ensure it was operating correctly. Examples include, leak testing the system and measuring the total system pressure, allowing the system to heat up and measuring for constant and uniform heating, running dummy ALD runs to check the computer programming for bugs, etc. This type of testing is straightforward and is necessary feedback during any development process. The next phase of testing involves operating the reactor as anticipated, looking for problems with the overall deposition. These tests were simply ALD depositions performed with published and well-studied ALD processes. This was done to isolate engineering problems from chemical problems, using well studied systems to point out any flaws in construction.

A primary concern is whether the gas valve system was operating as expected. If the "closed" valve pressure gradient wasn't operating correctly a small but constant amount of precursor would leaking into the reaction zone. The valve set up was tested using 3 different ALD chemistries. Iron oxide was deposited using ferrocene and ozone.[69] Hafnium oxide was deposited using hafnium chloride and ozone.[70] Finally copper oxide was deposited using copper acetylacetonate and ozone.[71] The deposited materials were compared to published results looking for any differences in deposition rate. The reactor was physically inspected looking for any material deposited in the reactor. This deposited material would indicate that at some point both precursors were allowed to interact, indicating a failure in the gas valving system at preventing unwanted precursor

introduction. The deposited materials compared favorably with their literature counterparts, and no extraneous depositions were found in the reactor. With the gas valve system confirmed to be working correctly, the next phase of testing was looking at how uniformly the reactor deposited films.

One of the design goals of this reactor was the ability to use 2in silicon wafers, so it is necessary to look at the film uniformity for the reactor as a whole and especially of a 2in square area. As with the valve testing a well-known ALD system was used to separate engineering problems from chemical problems. The system deposits zinc oxide via diethylzinc and ozone, and is a very well-studied system.[72] The initial testing involved placing small silicon wafers at regular intervals throughout the reaction zone. The film thickness of each of these pieces was measured via spectroscopic ellipsometry (See Chapter 3 for experimental conditions). The resulting image plot gives a reasonable map of thickness of the deposited material throughout the reactor (Figure 2.10). The image tells and interesting and disappointing story about the uniformity of the deposition. The film is non-uniform in a chaotic manner suggesting the conditions inside the reactor are non-laminar. The thickness per cycle of the deposited film is much lower than expected.[72]

Testing continued and the film uniformity continued to improve. Changing conditions such as reducing total gas flow into the reactor, increasing pulse and purge times, and changing the position of the silicon wafers in the reactor all contributed to making the films more uniform. Figure 2.11 shows the results of those incremental improvements. The film is uniform across the width of the reactor and shows a decreasing film thickness down the length of the reactor, indicative of simple precursor depletion along the length of the film. With continued tweaking there were incremental

improvements to the film uniformity.

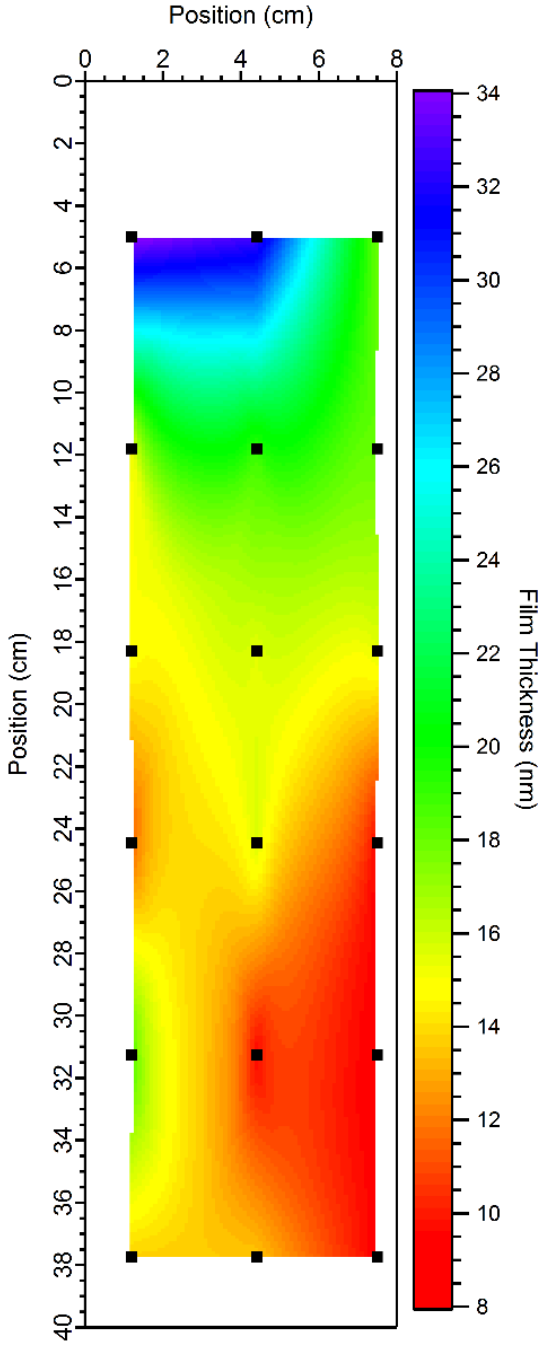

Figure 2.10: A diagram showing the film thickness deposited throughout the ALD reaction zone. Each black square represents a 1 cm^2 piece of silicon wafer. The film thickness deposited on each of these wafers was

measured. These points were used to make an intercalated color map image. The scales are measured in centimeters in x and y respectively. The origin represents the oxygen inlet, while (0,8) represents the zinc precursor inlet. This image is a flat representation of the curved inside surface of the ALD reaction zone.

However it became apparent that no amount of tweaking was going to allow the reactor to produce uniform films across the length of the reaction zone. While the reactor only needed to produce uniform films across a $2in^2$ area, rather than down the entire length of the reactor, it was unable to do that as well (Figure 2.12). In addition there is very little consistency between ALD depositions and seemly very little correlation between changing deposition conditions and overall film thickness and uniformity.

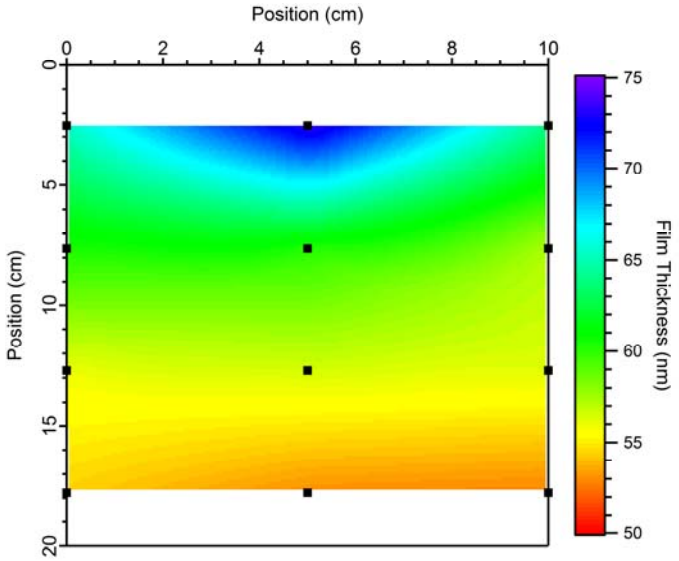

Figure 2.11: Shows another measurement of film uniformity through the reactor. The style and axes are the same as figure 2.10.

Figure 2.12 shows the results of two different ALD depositions. The changes between them are increasing the two solid precursor sheath gas flows from 10sccm to 20sccm, and increasing the purge pulse time from 16s to 20s (Figure 2.12b). The extreme difference in thickness between films makes studying ALD processes functionally impossible. However the differences in uniformity do offer evidence as to the problems, and potential solutions to the ALD reactor problems.

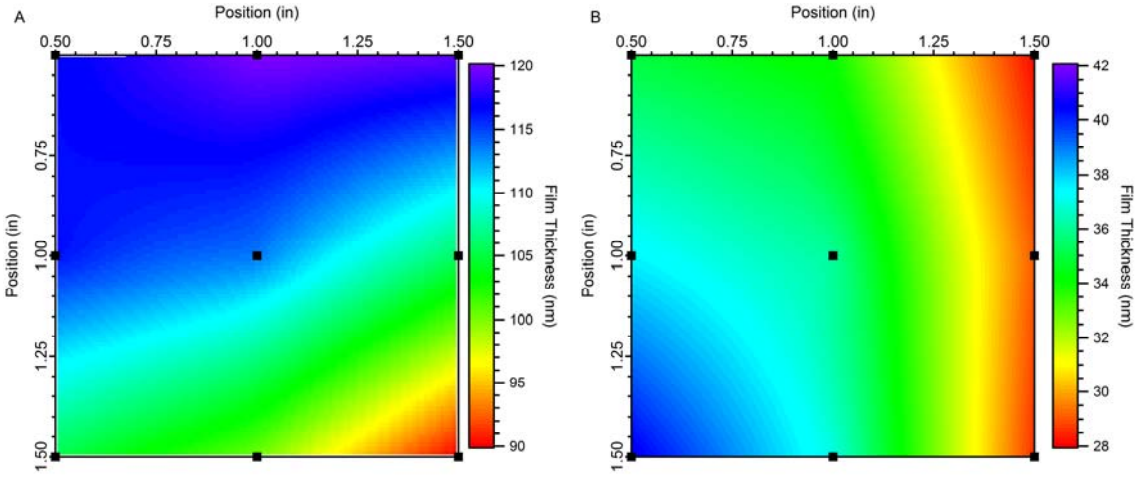

Figure 2.12: An image showing the film thickness of two ALD depositions. Each black square represents a film thickness measurement. These points were used to make an intercalated color map image. The scales are measured in inches from the top left corner of the silicon wafer.

The overall problem with this ALD reactor is its lack of consistency. That lack of consistency extends to patterns between test samples. A large number of depositions have been performed, each changing various reactor conditions in an effort to produce more uniform films. Improvements in film uniformity would result from changing, or overcoming a problem with, the hardware of the reactor. It is worth noting that during the

construction of the ALD reactor very little information was found regarding how to design a new reactor. There are numerous depictions of new systems, with new capabilities, but very little about why they were designed the way they were. The overall refrain was that the self-limiting chemistry of ALD would overcome any engineering problems associated with the reactor setup. Unfortunately it was both untrue and used as a guiding principle during construction. Lower costs and ease of construction were given greater priority during construction. The end result is that the reactor is too large in diameter. A 6in (4in diameter tube) conflat flange system was chosen as it allowed for the easy construction of the precursor manifold (Diagram S3, pg3-4). Rather than need to design and fabricate a complicated tubular manifold, the flange could simply be drilled at an angle at a fixed radius. The reactor uses a 4in diameter tube, and this causes most if not all of the problems. This diameter, along with its shape, causes the reactor to have ~19x the volume and ~5x the surface area over the smaller 1in diameter ALD reactor. The exhaust pumping speed is only 2.5x as fast as the smaller reactor. If the ALD deposition is corrected for this, by increasing the purge pulse by a factor of 8, more uniform films are produced. It also makes the ALD depositions several hours longer. The increase in surface area also causes much greater linear decrease of precursor, especially ozone.[73] This makes it very difficult to achieve uniform films along the length of the reactor.

There is also the problem of sample holding. The precursors are introduced along the equatorial plane of the reactor. Therefore the sample needs to be held along that plane in such a manner as to not cause disruptions in the flow the precursors. The reactor is also too short. This was simply done to save space, however, it means the sample is very close to the precursor inlets. There is very little time or space to establish the correct flow patterns

to ensure even coverage. Fortunately this problem is easy to solve. The main body of the reactor (figure 2.5) can be swapped out for a 2.5in diameter (4.5in conflat flange) and longer main body. Simple conical reduction fittings can be used to change between flange diameters. This modification would require some modification to the reactor support structure and would require the purchase of new 2.5in diameter heater. With this small input of time and money the ALD reactor should be able to produce much more uniform films.

2.5 Secondary ALD Reactor: During construction and testing of the larger solid precursor ALD reactor concurrent studies of ALD processes were ongoing. Our smaller 1in diameter ALD reactor were still limited in the availability of ALD precursors that motivated the construction of the larger solid precursor ALD reactor. However, the concurrent experimental ALD work was hampered by the lack of available precursors. So the decision was made to extend the capabilities of the one of the smaller diameter ALD reactors such that some solid precursors could be used. It should be noted that nothing done here will make this smaller reactor a direct replacement for the larger reactor. This reactor will always suffer from the fundamental constraint of having mechanical valves in the precursor delivery system. The mechanical valves have low flow rates, and a maximum manufacturer recommend operating temperature of 95°C, though extensive testing shows that these valves can be operated at 110°C long term without extensive degradation of the valve components. However, there are a wide range of available solid precursors that fit with the capabilities of this new system. A low cost retrofit to this reactor would be well worth it to extend its capabilities (figure 2.13).

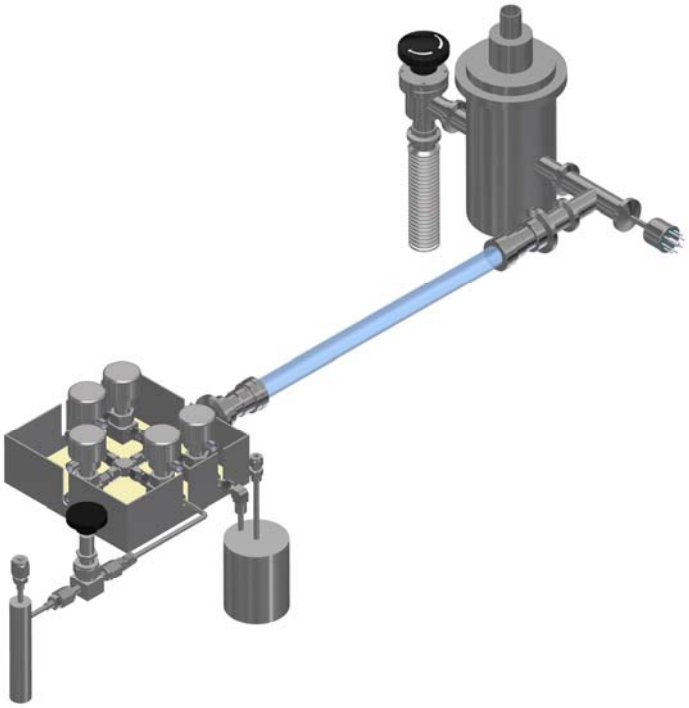

Figure 2.13: An image of the retrofitted small reactor. The left side contains the organometallic precursor vessel (small cylinder), the solid precursor vessel (large cylinder) and the valve assembly in its sand bath. The right side contains a pressure gauge, dry ice trap, and a valve for opening the reactor to the vacuum pump (not shown).

The first problem is how to store and deliver the solid precursor. The idea of using a solid precursor bubbler has been time tested and is more than sufficient for this application. The design philosophies used in the larger reactor were employed here as well. Commercial stainless steel pipe fittings were used as much as possible. Not only are these more than sufficient for the ~1 torr pressures being employed but they are significantly cheaper than having custom machined threaded components made. Figure 2.14 (diagram

S10) shows the constructed bubbler. It also uses commercial vacuum fittings to make it an almost drop in addition to the reactor.

Figure 2.14: Figure showing solid precursor bubbler.

The second problem is how to go about heating the precursor delivery system. If the precursor delivery system isn't heated to approximately the sublimation temperature of the precursor it will simply condense in the delivery lines. Previously these lines were heated with heating tape and a variac. However there were always problems with poor uniformity in heating. A simple holder was devised to contain the entire valve assembly in a sand bath. This not only provides the benefits associated with high thermal mass and even heating, but also from having as short a valve train as possible. Figure 2.15 (diagram S11) shows the complete sand bath container along with the associated valve components.

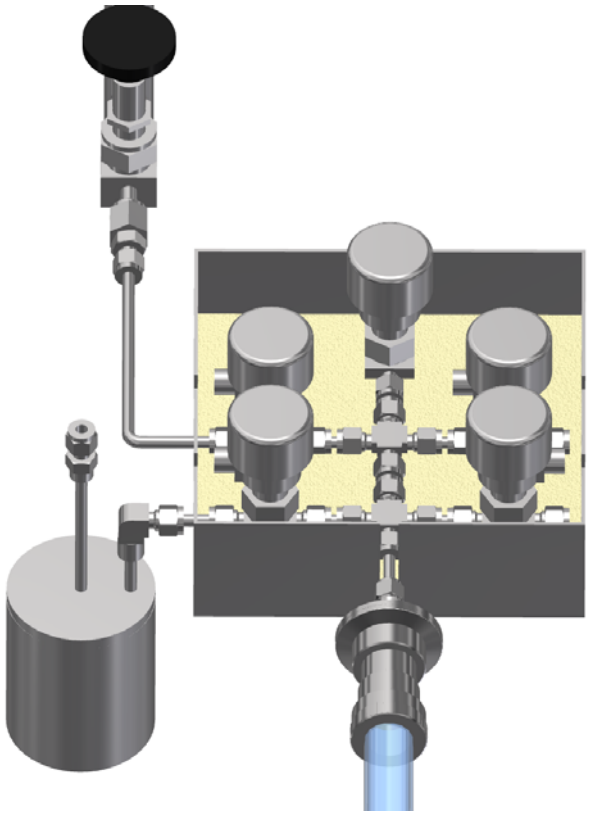

Figure 2.15: Image of sand bath with valve train.

2.6 Conclusion: The study of ALD chemistry requires the ability to pursue new precursors. This pursuit can be hampered by the hardware limitations associated with available ALD reactors. Two new ALD reactors have been constructed and tested in order to expand current ALD capabilities to use solid precursors.

Chapter 3:

3.1 Background: Thin films and coatings are a convenient way to modify the surface properties of a material without sacrificing the desired properties of the bulk material. This has been true even since the first thin coat of grease was rubbed on a moving element to reduce its coefficient of friction. Thin film technology has progressed to the point that then films are ubiquitous in our modern society. Everything from self-cleaning windows and hard anodizing, to semiconductor devices and solar cells requires thin films and processes to deposit them.[74-75]

3.1.1: Atomic Layer Deposition (ALD): There are three broad categories of vacuum-based thin film deposition. Physical vapor deposition where the desired coating material exists in a bulk state and is then used to deposit a thin film of material on a target substrate by means such as evaporation, or ion sputtering of a target.[74] Chemical vapor deposition where two chemical precursors are introduced into the vacuum chamber and their reaction, either in the gas phase or on the substrate surface, causes the deposition of the desired thin film material.[74, 76] Atomic layer deposition splits the CVD process into two half reactions. Each precursor saturates the substrate surface before being reacted with the second precursor in order to form the thin film material.[74, 77] Investigations into the ALD process began in the late 1970's[78] as an offshoot of CVD processes but ALD has several important advantages over CVD that make it a technique well worth the study. All of these advantages arise from the ALD process being self-limiting. The saturation of all the available surface binding sites means that the rate of deposition is independent of precursor delivery time. This leads to the following advantages. ALD provides single monolayer control over final

film thickness.[74-75, 77, 79-80] ALD provides dense, uniform, defect free film, even on high aspect ratio substrates.[74-75, 77, 79-80] These advantages are offset by a major disadvantage of ALD, the slowness of deposition.[74-75, 77, 79-80] Deposition rates are usually measured in angstroms per cycle which can lead to very long depositions times.

3.1.2 Metal Oxide ALD: Metal chalcogenide systems were the original ALD systems.[78, 81] In fact the deposition of zinc oxide[72, 82] and aluminum oxide[83] are still considered to be model ALD systems. Metal oxide ALD has an important use, high-k dielectric gate oxides in semiconductor manufacturing.[79-80] Materials such aluminum oxide, zirconium dioxide, and hafnium dioxide are used to overcome problems with silicon dioxide as gate oxide material in transistors.[79-80] Another use of metal oxide thin films is in transparent conduction oxides (TCO). These materials such as indium tin oxide and aluminum doped zinc oxide, while not necessary to deposit them via ALD, are very important materials.[84-85] As their name implies they are optically transparent semiconductors, and they are vital in any application that requires transparent electrical contacts, such as in electronic displays and solar cells.[84-85]

3.1.3 Copper Oxide: It is worth noting that all of the mentioned TCOs are n-type semiconductors, and the lack of p-type TCOs prevents the creation of more complicated transparent devices. However copper (I) oxide is a p-type semiconductor[86-87] and alloyed with aluminum in the form of copper (I) aluminum oxide [$CuAlO_2$] is a p-type transparent conduction oxide.[87-88] That distinction of copper (I) aluminum oxide is important, copper aluminum oxide exists in two forms: copper (I) with the formula $CuAlO_2$ and copper (II) with the formula $CuAl_2O_4$. These materials have different crystal structures with copper (I) aluminum oxide forming a delafossite crystal structure[87], and copper (II) aluminum oxide

forming a spinel crystal structure.[89] There is also a difference in optical band gap with the copper (I) system having a band gap of ~3.5 eV[90] and the copper (II) system have a band gap of ~2.1 eV.[89] The visible portion of the electromagnetic spectrum covers ~1.77 – 3.00 eV. The wider band gap of the copper (I) aluminum oxide makes it the necessary species for a TCO.

3.1.4 Copper Oxide ALD: The development of copper ALD began by looking at ways to deposit copper metal. This was to ensure even coverage over high aspect-ratio substrates and to serve as seed layers for other, faster, forms of deposition but still ensuring even coverage.[91-92] ALD precursor development started by using copper halides.[93-94] As is the case with most halide salt precursors the precursor and deposition temperatures required were too high to make the process widely viable. As with many previous metal systems[95] precursor development began using bis-bidentate organometallic complexes as ALD precursors. Diketonates[96], highly fluorinated diketonates[96] amidinates[97], diketimines[97-99], and aminoalkoxides[100] have all been used as ALD precursors to deposit copper metal. Copper oxide ALD research has been able to leverage this copper metal ALD research, as copper metal ALD typically uses a copper precursor pulse followed by a reducing agent pulse[92-94, 96-97], while copper oxide ALD uses an oxidizing agent pulse.[71, 101] The system chosen for the ALD deposition of copper aluminum oxide was copper acetylacetonate (acac) and ozone. This system has been successfully used to deposit copper oxide films[71] and copper acac is a safety, air stable, and inexpensive precursor.

3.2 Experimental:

3.2.1 Substrate Preparation: Unless otherwise noted all the sample substrates were prepared in the following manner. All chemicals were used as received from their

manufactures. Soda lime glass was cut in 1cm x 1cm pieces. The samples were placed in a piranha etch solution for 10min. Piranha etch is a 70:30 mixture of concentration (18 M) sulfuric acid and 30% hydrogen peroxide. The samples were removed, rinsed with DI water, rinsed with ethanol and dried under nitrogen. Silicon [100] wafers were cut into 1 cm x 1 cm pieces. The samples were placed in a piranha etch solution for 10 min. The samples were removed, rinsed with DI water and placed in a concentrated HF bath for 10 min. The samples were removed, rinsed with DI water and dried under nitrogen. The magnesium oxide 1 cm x 1 cm wafer was stored in the manufacturer's package until use and used as received. The pyrolytic boron nitride 1 cm x 1 cm wafer was soaked in a 1:10 HF:DI water solution for 15 min, rinsed with DI water and dried under nitrogen.[102] After drying all samples were affixed to a 0.5 in x 3 in stainless steel sample stage with aluminum furnace tape and immediately inserted into the hot ALD reactor. The ALD reactor was then immediately evacuated.

3.2.2 Precursor Preparation: All precursors were commercially available and used as received. All nitrogen was supplied via pure nitrogen (99.99%) compressed gas cylinders. The nitrogen functioned as a reactor purge gas, precursor carrier gas, and gas for actuating the pneumatic valves. The copper precursor used was 97% copper (II) acetylacetonate (acac) from Sigma Aldrich. The copper precursor was loaded into a custom stainless steel bubbler (figure 2.13). It was evacuated before heating to the base pressure of the ALD reactor, ~300 mtorr. The bubbler was heated in an oil bath to 140 °C, and the vacuum line between the bubbler and valve assembly sand bath (figure 2.14) was wrapped in heating tape and heated to ~180 °C. During the copper precursor pulse 40 sccm of nitrogen carrier gas was blown through the top of the bubbler to increase the copper precursor delivery.

The aluminum precursor was 97% trimethylaluminum (TMA), used as a neat liquid from Sigma Aldrich. Since TMA is highly pyrophoric it was handled in a nitrogen glovebox. TMA was loaded into a custom stainless steel bubbler equipped with a valve so the precursor could be safely attached to the ALD reactor. While the bubbler is equipped with an inlet for nitrogen carrier gas, the precursor is volatile enough to be used without a carrier gas. Before opening the precursor valve, the precursor line was evacuated to the base pressure of the reactor to remove any atmosphere oxygen that would cause aluminum oxide deposition in the precursor lines. The bubbler was placed into a 0 °C ice bath, and allowed to cool before a deposition took place. Ozone was supplied via an Ozone Solutions RMU16-08 ozone generator. Industrial grade oxygen was supplied to the generator at a rate of 3 L/min, from which the generator generated a 3% ozone in oxygen mixture that was supplied to the reactor.

3.2.3 Deposition Preparation: All precursors were delivered to the reactor via Swagelok BK series pneumatic valves. The valves were controlled via OMEGA SVP-1 120v solenoids and an OMEGA PCI-PDIS016 120v controller card. The OMEGA card is controlled via National Instruments LabView running custom software. All gas flows are monitored via UNIT 1660 100 sccm mass flow controllers (300 sccm for nitrogen) these are controlled by a URS-100 central controller. The gas flows were set as following: nitrogen purge gas 240 sccm, ozone 80 sccm, and copper carrier gas 40 sccm. The reactor was heated using a Lindberg/Blue M 1 in tube furnace, temperatures varied between 160 °C and 320 °C depending on the deposition. The reactor was evacuated and exhausted via an Alcatel C1 2010 vacuum pump. Depositions of copper oxide follow the same pattern: nitrogen pulse, copper precursor pulse, nitrogen pulse, and ozone pulse. This is one ALD

cycle and is repeated as many time as is required by the deposition (Figure 3.1).

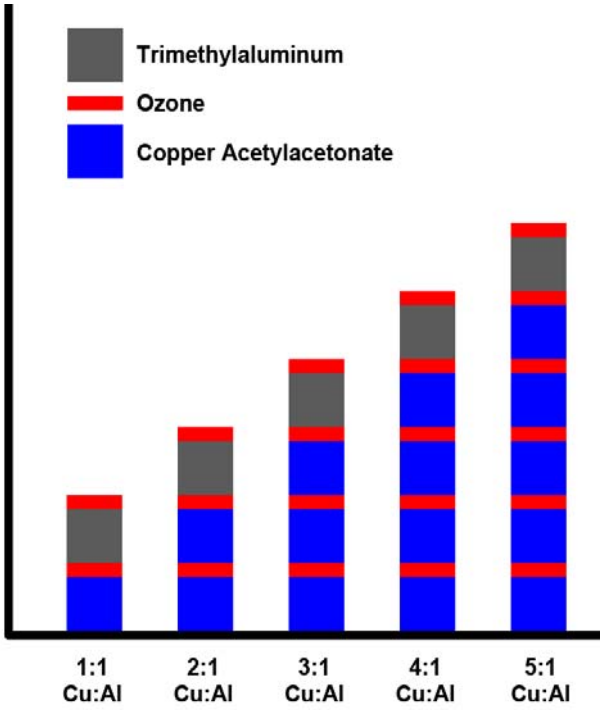

Figure 3.1: Is a visual illustration of supercycles. Each material ALD cycle, represented here by a metal and ozone pulse group, is repeated a number of times in order adjust the final elemental composition of the film. The nitrogen purge pulses have been omitted for clarity.

Unless otherwise noted depositions of copper aluminum oxide use the following supercycle pattern. A supercycle is a name for a single ALD cycle that contains several smaller discrete cycles in it, and is useful way to control the elemental composition of a film. A general copper aluminum oxide pattern is as follows: nitrogen pulse, (copper precursor pulse, nitrogen pulse, ozone pulse, nitrogen pulse) x N, aluminum precursor pulse, nitrogen pulse,

ozone pulse. The number of copper oxide pulses (N) is varied across depositions to control the elemental ratio of the deposited films.

3.3 Characterization:

3.3.1 UV-Vis Spectroscopy: All measurements were taken on an Ocean Optics USB4000 spectrophotometer using an integration time of 5 seconds and averaging 100 scans. All spectra were taken on film deposited on soda lime glass.

3.3.2 Spectroscopic Ellipsometry: All measurements were taken on a J.A. Woollam Co. V-VASE HS-190 spectroscopic ellipsometer. Scans were taken at 60 and 75 degree angles between 800 nm and 1100 nm, using 20 nm steps on films deposited silicon substrates. Film thickness was calculated using a Cauchy fitting model.[103-104]

3.3.3 X-ray Diffraction: All measurements were taken on a Bruker-D8 Discover 2D using a Co K_α x-ray source and a 0.8 mm spot size. Samples were deposited onto silicon wafers before measurement. Each sample was scanned twice, once at $2\theta = 35°$ and $\Omega = 17.5°$ for 5 minutes and once at $2\theta = 60°$ and $\Omega = 30°$ for 5 minutes. The spectra were combined and peaks were fitted using MDI JADE 9.

3.3.4 Auger Spectroscopy: All measurements were taken on a PHI NanoProbe 670 Auger system equipped with a field emission gun and a cylindrical mirror analyzer. The base pressure was 2.0×10^{-10} Torr. The sample was mounted on a sample stage using carbon tape. The primary electron beam energy was 5 keV, and the beam size was ca. 100 nm. In the measurements, a survey spectrum was collected in the energy range of 40 to 2040 keV, followed by the depth profiling using Ar^+ sputtering. The Ar^+ sputtering conditions were: 25 mA emission current, 0.010 Pa Ar pressure, 4 keV Ar^+ beam energy and 2 x 2 mm^2 sputtering size. The sputtering rate calibrated with SiO_2 /Si samples was 8.0 nm per minute.

A 30 second/cycle was used in the depth profiling.

3.3.5 X-ray Photoelectron Spectroscopy: XPS measurements were performed on an SSX-100 system (Surface Science Laboratories, Inc.) equipped with a monochromated Al K_α X-ray source, a hemispherical sector analyzer (HSA) and a resistive anode detector. The base pressure of the XPS system was 4.0 x 10^{-10} Torr. During the data collection, the pressure was 1.0 x 10^{-8} Torr. The sample was mounted on a sample holder using carbon tape. The X-ray spot size was 1 x 1 mm^2, which corresponded to an X-ray power of 200 W. The surface was sputtered with Ar^+ ions (4 keV) until the C 1s peak was no longer visible. The survey spectrum was collected using 150 eV pass energy and 1 eV/step. The high resolution spectra were collected using 50 eV pass energy and 0.1 eV/step. The atomic percentages were calculated from the survey spectra using the ESCA HAWK software provided with the XPS system. For high resolution data, the C 1s peak was set at 285.0 eV and used as the reference for all of the other elements. The curve fitting used the Shirley background subtraction and a combination of Gaussian/Lorenzian function with the Gaussian percentages being at 80% or higher.

XPS measurements were performed on an PHI VersaProbe III XPS system (ULVAC-PHI) equipped with a monochromated Al K_α X-ray source (1486.6 eV). The base pressure of the XPS system was 5.0 x 10^{-8} Pa. During the data collection, the pressure was 1.0 x 10^{-6} Pa. The sample was affixed to the sample holder by copper tabs. The X-ray spot size was 100 μm in diameter, which corresponded to an X-ray power of 25 W. The surface was sputtered with Ar^+ ions (3 keV) in a 3 x 3 mm raster until the C 1s peak was no longer visible. The survey spectrum was collected using 280 eV pass energy and 1 eV/step. The high resolution spectra were collected using 26 eV pass energy and 0.05 eV/step. The

atomic percentages were calculated from the survey spectra using the PHI MULTIPAK software provided with the XPS system. For high resolution data, the C 1s peak was set at 285.0 eV and used as the reference for all of the other elements. The curve fitting used the Shirley background subtraction and a combination of Gaussian/Lorenzian function with the Gaussian percentages being at 80% or higher.

3.3.6 SEM and EDS: Measurements were taken on a Hitachi SU8230 field emission gun scanning electron microscope. Images were taken using the in-column secondary electron detector. Individual working conditions are attached to the relevant images. EDS measurements were taken on an attached Thermo-Fischer Noran system 7 EDS systems with an UltraDry 8525 silicon drift detector. The detector with cooled with liquid nitrogen. The beam current was 5 keV and the take-off angle was 30°. EDS spectra were taken using a 120 s live time measurement. Elemental ratios were calculated using the included Noran software.

3.3.7 Electron Microprobe: Quantitative elemental analysis of thin films were performed on a JEOL JXA-8900R electron probe microanalyzer. The software package ProbeforEPMA was used for data acquisition. Data was then processed with the commercial thin film software STRATAGem, which iteratively fit k-ratios at multiple accelerating voltages in order to determine mass thickness and elemental composition.[105] Data were acquired at three different accelerating voltages of 4, 7 and 10 keV. The beam current was 20 nA, and the beam diameter was 5 microns. Elements were acquired using analyzing crystals PETH for Si Kα, TAP for Al Kα, Cu la, and LDE1 for O Kα. The standards were Al2O3 for Al Kα and O Kα, Cu metal for Cu Lα, and Si metal Si for Si Kα. The on and off peak counting time was 20 seconds for all elements. Off Peak correction

method used a linear background model for Cu Lα, Al Kα, and Si Kα. An exponential background model was used for O Kα.[106] Unknown and standard intensities were corrected for dead time. The ZAF or Phi-Rho-Z matrix correction algorithm utilized was Armstrong/Love Scott.[107]

3.3.8 Rutherford Backscattering Spectroscopy: Measurements were taken on a MAS 1700 pelletron tandem ion accelerator (5SDH) equipped with charge exchange RF plasma source by National Electrostatics Corporation (NEC). The detector angle was fixed at 165°. Samples were analyzed using a He^{++} 2.3 MeV beam with a 5 μC current. Peak areas were found using Gaussian curve fits in the commercial software IgorPro. Elemental ratios were found using equation 3.1.[108]

3.4 Results:

3.4.1 Copper Oxide: The thin film interference color effect, ranging from gold to blue, makes it is apparent upon removing the sample substrates from the ALD reactor that films have been successfully deposited. However, the characterization of both the ALD process, and the material nature of the films themselves is less apparent at the outset. An especially important question, one that will be asked repeatedly throughout the characterization, is the exact nature of the copper atom. The oxidation state of the copper, as previously noted, has a profound effect on the structure of the film, and by extension the film's properties.[86]

The first step in characterizing a new ALD process is to examine whether the process is in fact ALD. The process needs to show the characteristic self-limiting nature of ALD[77], as opposed to non-self-limiting CVD type processes.[76] Figure 3.2 shows a graph of deposited film thickness versus the number of ALD cycles. The linear nature of the plot shows that each cycle is depositing a fixed amount of material, something characteristic of

a self-limiting process. Each cycle deposits 0.038 nm of material, which compares favorably with published results.[71]

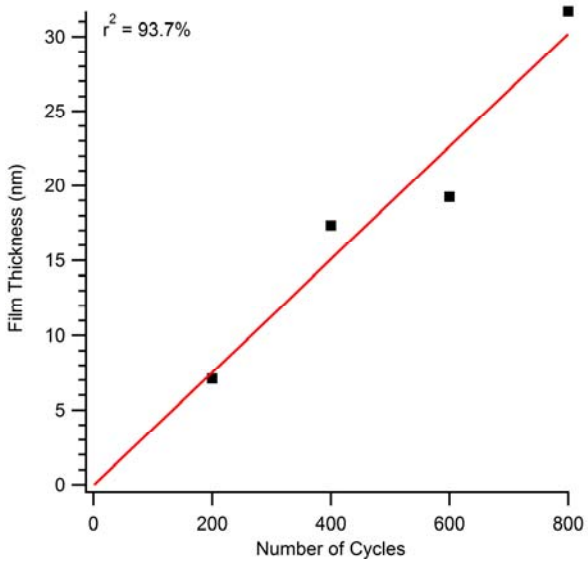

Figure 3.2: A graph a plot of film thickness vs. the number of ALD cycles, a linear fit to the data is shown in red, and with the associated r^2 value.

The next step is to examine how film thickness is affected by precursor pulse time. If the deposition process is self-limiting, above a certain pulse time length there should be no increase in film thickness with increasing pulse time. Figure 3.3 shows how film thickness per cycle varies as a function of the two precursor pulse times. Both precursors show the self-limiting behavior indicative of an ALD process.

The final step in the characterization of an ALD process is to investigate the effects of temperature on the deposition rate. There is a range of temperatures where ALD behavior is observed, called the ALD window.[77] Below that temperature the precursors no longer react, above that temperature ALD behavior breaks down in favor of a more CVD-

type process. This window is apparent when looking at a graph of film thickness per cycle vs. temperature.

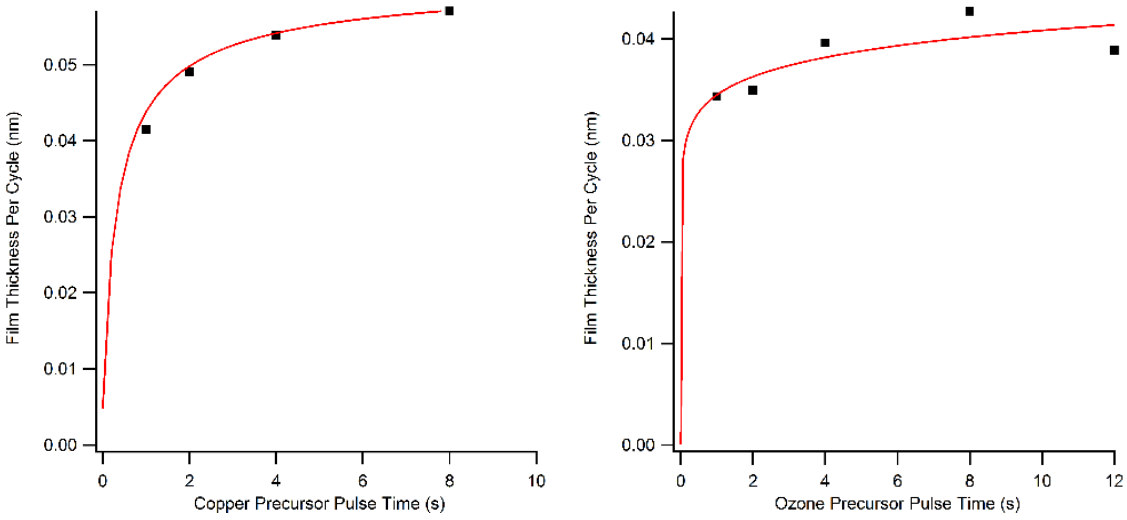

Figure 3.3: Shows the graphs of film thickness per cycle vs copper precursor pulse time (left) and ozone precursor pulse time (right). Both shows the leveling off of film thickness per cycle indicative of a self-limiting deposition process.

Figure 3.4 illustrates this window clearly. Below 140°C, the sublimation temperature of the $Cu(acac)_2$ precursor, the film doesn't form. Above 280°C the films begin to deviate strongly from lower deposition temperature films, both in thickness per cycle and in other properties such as visual appearance, becoming non-uniform and streaky, or chalky in appearance.

Before characterizing the other properties of the deposited film, determining the elemental make up the film is necessary. This serves two purposes. One, to confirm that at least macroscopically the material deposited is the one that was wanted. Two, is to check the contaminate incorporation in the film. A major problem with using organometallic ALD precursors is carbon incorporation into the film. Therefore, checking the elemental

composition of the film at the outset will eliminate any ALD processes that should be disqualified by incorporating too much carbon into the film. Figure 3.5 auger spectroscopy depth profile. The film was ion milled down to the substrate and the elemental composition was measured in steps. There is almost no carbon incorporation into the film and the film shows clean transitions between the carbon rich, contaminated surface, the deposited material, and the silicon substrate.

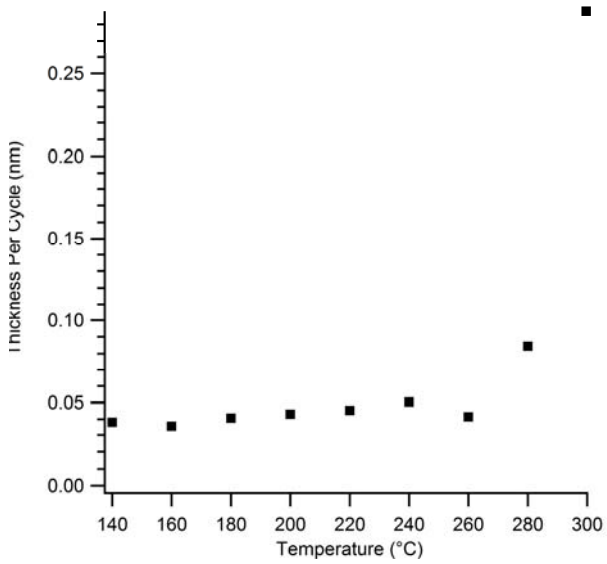

Figure 3.4: A graph showing the film thickness per cycle vs. deposition temperature.

Now that the ALD nature of this deposition process is established, attention can be turned to characterizing the resulting films. The idea behind these copper oxide materials is as a transparent conducting oxide (TCO), thus the obvious choice to look at how these films interact with light. Figure 3.6 shows a UV-Vis absorption spectrum for a copper oxide film deposited on soda lime glass. The film is absorbs somewhat throughout the visible region of the spectrum, more so than is usually acceptable for a TCO.[85]

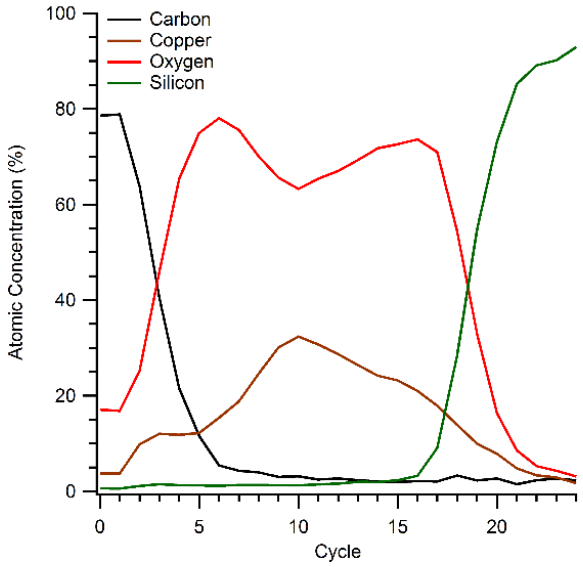

Figure 3.5: An auger depth profile of the as deposited ALD film. Each cycle is ~4nm in depth.

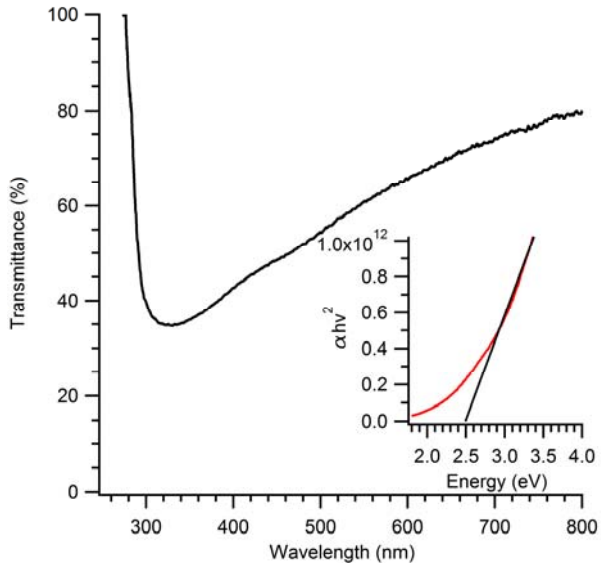

Figure 3.6: An UV-Vis absorption spectrum of a copper oxide thin film. The inset is a Tauc plot of the same film, showing a direct optical band gap of 2.49 eV

The inset in the figure is a Tauc plot, a method of estimating the optical band gaps of materials.[109] The type of transition can be determined by changing the exponent on the y-axis. In this case, $\alpha h\nu^2$ for the direct optical band[109] gap of the film, which is 2.49 eV. This is much closer to the direct optical band gap of Cu_2O band gap of 2.6 eV than to the indirect band gap of 1.4-1.7 eV for CuO.[86, 110]

The optical band gap provides indirect evidence as to the material being deposited. X-ray diffraction, which provides structural information based on the interaction of x-rays with long range order in the sample material, would hopefully provide direct structural information. The x-ray diffraction pattern (figure 3.7) shows the broad, featureless spectrum associated with an amorphous solid.

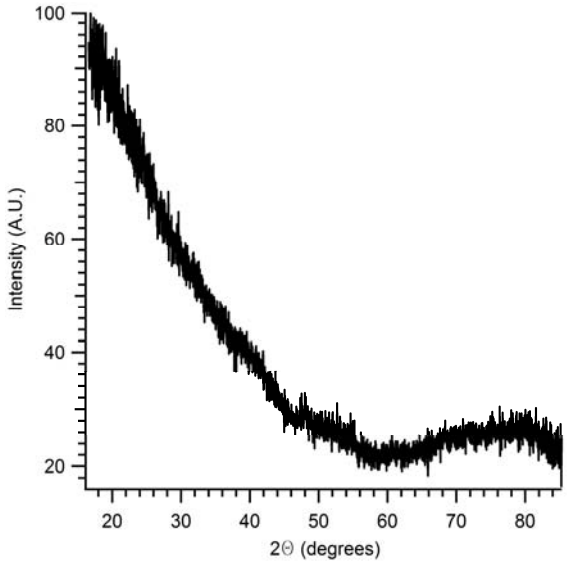

Figure 3.7: X-ray diffraction spectrum. The lack of peaks in the pattern demonstrate the amorphous nature of the ALD film.

This is typical of ALD deposited films. The lack of structural information makes correctly

characterizing the copper oxide film challenging. An SEM images shows a nearly featureless, if somewhat textured surface. (Figure 3.8). If determining the form of copper oxide is not possible from structural information the next option is determining it from the oxidation state of the copper atom.

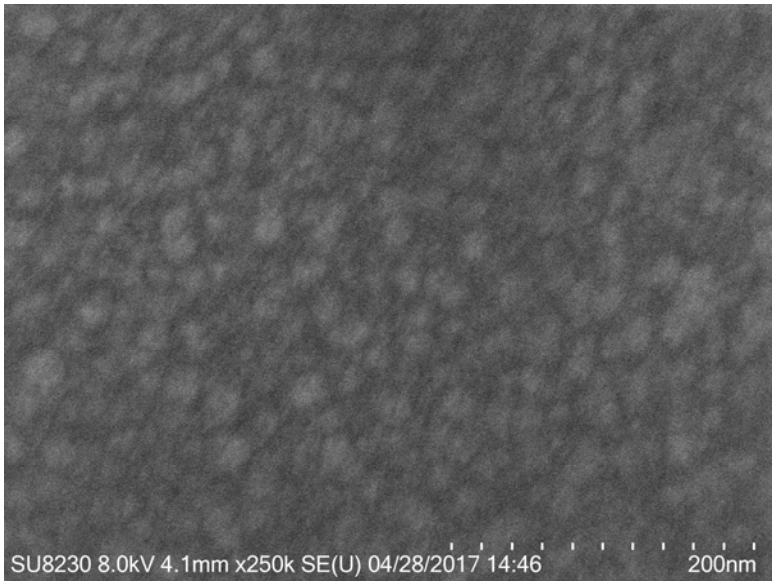

Figure 3.8: An SEM image of a copper oxide film deposited via ALD. The film shows a slightly textured appearance.

X-ray photoelectron spectroscopy (XPS) makes determining the difference between Cu^{1+} and Cu^{2+} very straightforward.[111-113] The copper 2p region for Cu^{1+} shows two peaks for the $2p_{1/2}$ and $2p_{3/2}$ respectively.[112] The same region for Cu^{2+} shows four peaks.[113] These satellite peaks are caused by shake up.[114] Cu^{2+} is a d^9 species and the outgoing photoelectron can interact with empty orbitals. This causes it to lose some energy and the detector sees the photoelectron as having a lower kinetic energy. This then becomes a higher binding energy on the spectrum. Figure 3.9 shows the XPS spectrum of ALD deposited copper oxide. The elemental information from the XPS reaffirms the information

from the Auger measurements. The film contains nearly all copper and oxygen.

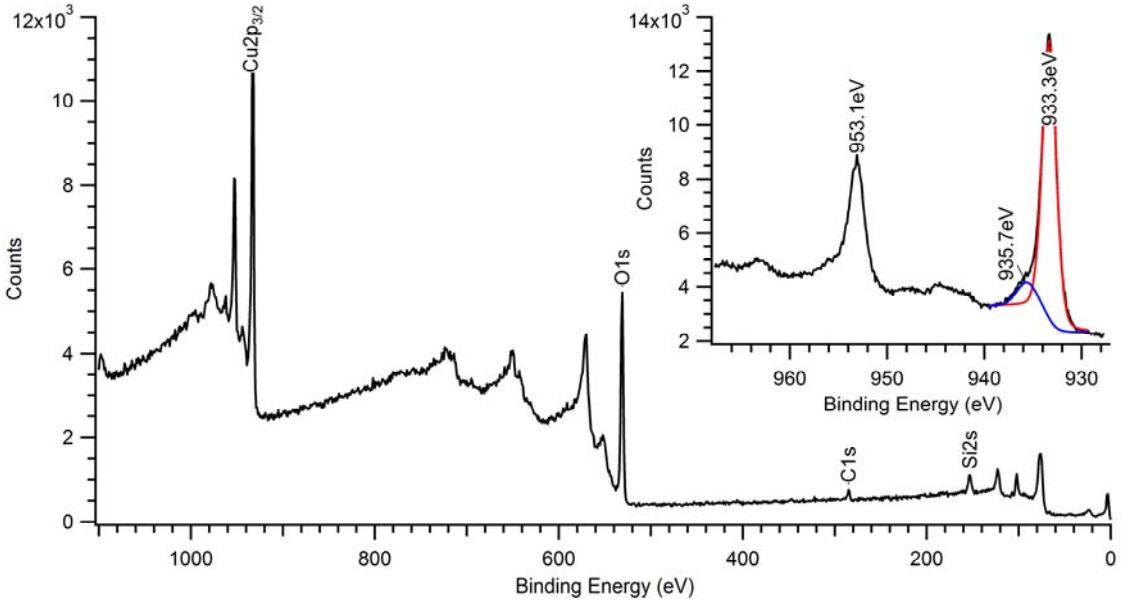

Figure 3.9: XPS spectrum for deposited copper oxide. The inset shows an enlarged portion of the lower survey spectrum. The red trace is a fit to a Cu(I) species and represents 90% of the deposited material. The blue trace is a fit to a Cu(II) species and represents 10% of the material.

The carbon and silicon peaks are just contaminates, from the XPS instrument itself and silicone vacuum grease in the ALD reactor, respectively. The inset shows the Cu 2p region with the accompanying fitting. The red trace is the fit for a Cu^{1+} and represents 90% of the material. The blue trace is a fit for a Cu^{2+} species and represents 10% of the material.[112-113] The presence of Cu^{2+} is also evident in non-linear background between the Cu 2p peaks, while not full on peaks themselves they are evidence for a Cu^{2+} species being present. The higher binding energy (935.7 eV) of the Cu $2p_{3/2}$ peak, as well as the O 1s binding energy (532.5 eV) are a much better fit for $Cu(OH)_2$ that for CuO.[111-113, 115] This is to be expected, the films are amorphous and non-regular bonding environments could easily happen during

the deposition process.

Films of copper (I) oxide have been successfully deposited via ALD using copper (II) acac and ozone. The original strategy was to deposit copper oxide [presumed to be copper (II)] and use trimethylaluminum to reduce the films to the desired copper (I) aluminum oxide films. Simple organometallics have been shown to be useful reductants in copper ALD systems.[116-117] While not strictly necessary the deposition of copper (I) oxide films is a bonus, however, it presents some problems. First at the temperatures and oxygen pressures during the deposition process CuO is much more thermodynamically favorable than Cu_2O.[12, 71] Secondly, a previous study of the same ALD system produced copper (II) oxide films, which were readily observed via XPS.[71] While the XPS data in figure 3.9 shows copper (I) oxide films it is important to understand this ALD system and what parameters are causing the deposition of copper (I) rather than copper (II). Several experiments were conducted in an effort to cause a transition in the deposited material from copper (I) to copper (II).

The obvious first choice is to increase the amount of ozone available during deposition to see if the oxidation state of the copper changes as a result. Figure 3.10 shows the results of the increase in ozone precursor pulse time. The films are essentially identical in the Cu 2p region. Both films show the same 90%/10% two peak fitting as seen in figure 3.9. The binding energies of those two peaks only differ by 0.3 eV.

The films were also heated in air after deposition in an effort to oxidize them further. Figure 3.11 shows the Cu 2p region after various heating regiments. There is some variation between samples but there is no sign for an increase of copper (II) in the films after heating.

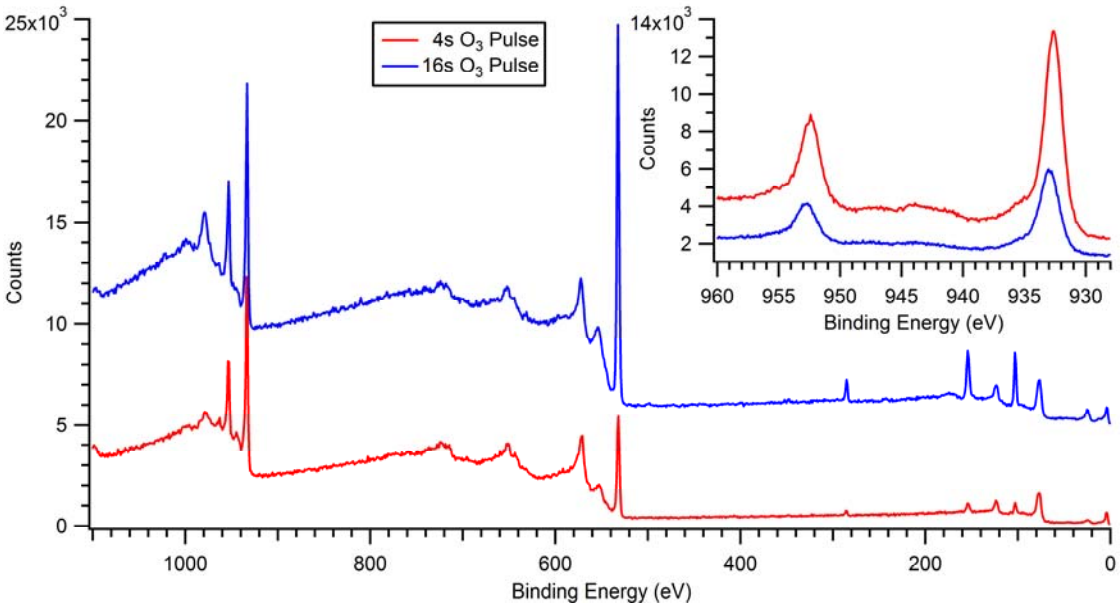

Figure 3.10: XPS spectra of copper oxide films deposited with differing ozone precursor pulse times. Neither sample shows an increase in the higher binding energy shake up peaks associated with copper (II).

Finally, films that were deposited at different reactor temperatures (figure 3.4) were analyzed via XPS. As with previous spectra there is some variation between samples but there is no large increase in Cu 2p shake up peaks that would indicate the presence of larger amounts of copper (II) (figure 3.12). It is also worth noting that for the films deposited at 140 °C and 300 °C there was a C 1s peak that couldn't be removed via sputtering. It was also fit to more than one peak, this indicates different species of carbon atoms in the film, showing that there is carbon being incorporated into the film as it is being deposited. This further strengthens what figure 3.4 already demonstrated that ALD behavior breaks down outside of a temperature window.

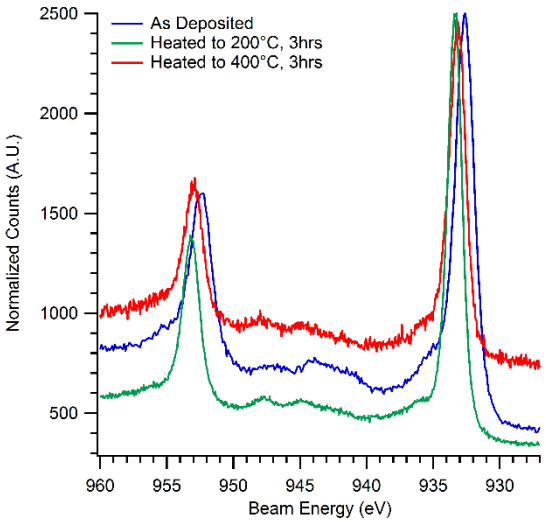

Figure 3.11: XPS spectra of copper oxide ALD films that have been heated in air to various temperatures after deposition. There is no increase in shake up peaks indicated the deposition of copper(II).

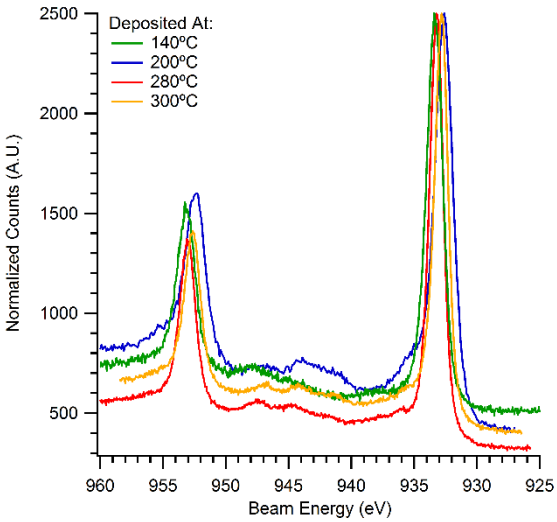

Figure 3.12: XPS spectra from copper oxide films deposited at different temperatures. There is no increase in shake up peaks indicated the deposition of copper(II).

3.4.2 Copper Aluminum Oxide: Films of copper (I) oxide have been successfully produced and incorporating aluminum is the next step in the deposition process. Figure 3.13 shows the linear thickness per cycle relationship for a 5:1 Cu:Al supercycle. (5 copper oxide ALD pulses for every 1 aluminum oxide ALD pulse). The films are visually uniform as seen with the copper oxide films, however the SEM image (figure 3.14) shows the films to have a somewhat more textured surface than the copper oxide films.

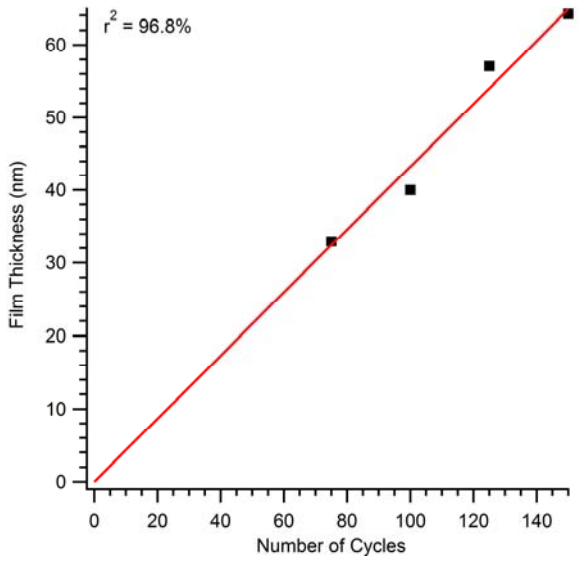

Figure 3.13: Graph of a film thickness per number of deposition cycles for a series of 5:1 Cu:Al depositions. The linear fit shows a consistent deposition rate per cycle.

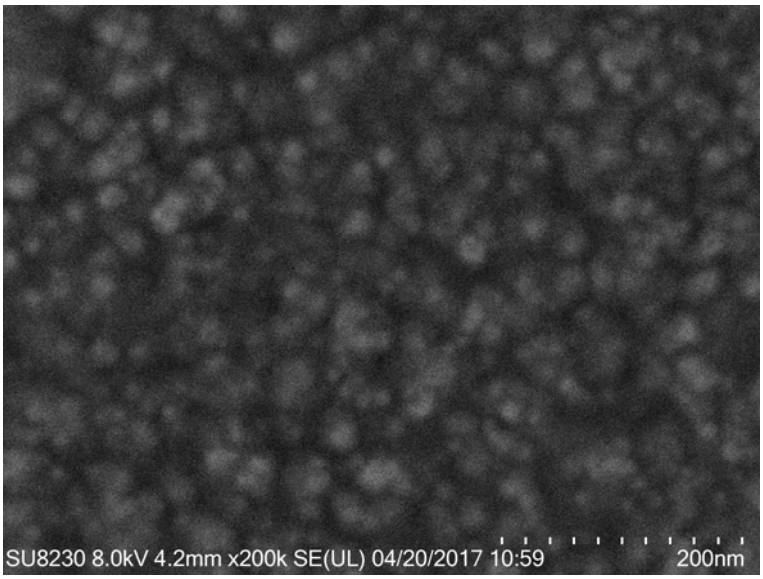

Figure 3.14: SEM image of a copper aluminum oxide film, showing a somewhat textured surface.

The characterization of the copper aluminum oxide deposition process proceeded in two distinct but complimentary directions. The first is analyzing the nature of the copper atom. Copper aluminum oxide exists in two forms that differ based on the oxidation state of the copper. Since these films are amorphous like the copper oxide films (Figure 3.15) the oxidation state of the copper therefore is the best option for determining the composition of the copper aluminum oxide.

The second method for understanding the ALD process is to investigate the elemental ratios of the resulting films. The process variables for this analysis were kept constant, using the pulse times for copper and ozone that result in surface saturation in the copper oxide films.

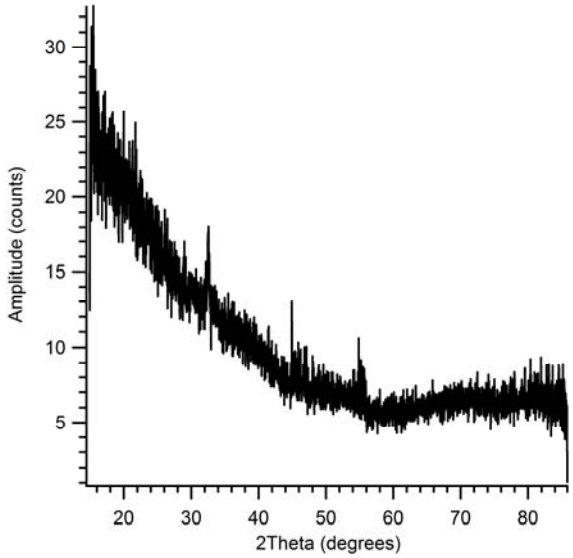

Figure 3.15: XRD spectra of copper aluminum oxide thin film. The lack of diffraction peaks demonstrate that the film is amorphous.

The aluminum pulse times are kept fixed at a small value (0.5s) and the copper:aluminum

ratio is varied by varying the number of copper oxide cycles per supercycle. Figure 3.16 shows the results of varying the number of copper oxide pulses per supercycle. Both the film thickness per supercycle and atomic percentage of copper follow a linear trend. This indicates predictable ALD behavior; copper oxide is being deposited normally onto the layer of aluminum oxide.

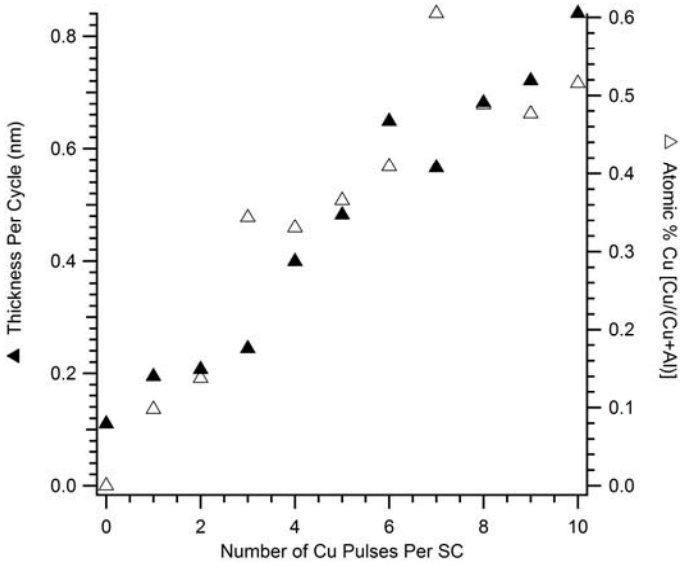

Figure 3.16: Shows a series of copper aluminum oxide films where the Cu:Al pulse ratio was varied from 0:1 to 10:1. Atomic concentration of copper (open triangles) is on the right axis and film thickness per supercycle (filled triangles) is on the left axis. Film thicknesses were measured using spectroscopic ellipsometry. Elemental ratios were measured via an electron microprobe (WDS).

If for example, there was reduced growth of copper oxide onto aluminum oxide, there would be a film thickness per supercycle plateau until the number of copper oxide pulses were sufficient to fully cover the aluminum oxide surface and then allow growth to continue before. This kind of deviation from linear behavior isn't observed, indicating a straightforward deposition process. The graph also shows that for supercycle ratios of greater than 8:1, Cu:Al the ideal atomic ratio of 1:1 Cu:Al is achieved.

Looking forward to determining the oxidation state of the copper there are several methods that can be employed. The first is to look at the differences in optical band gap between the two phases of copper aluminum oxide. Copper (I) aluminum oxide has a band gap of 3.5eV and copper (II) aluminum oxide has a band gap of 2.1eV.[87] Figure 3.17 shows the UV-Vis spectra for several copper:aluminum ratios as well as their associated Tauc plots.

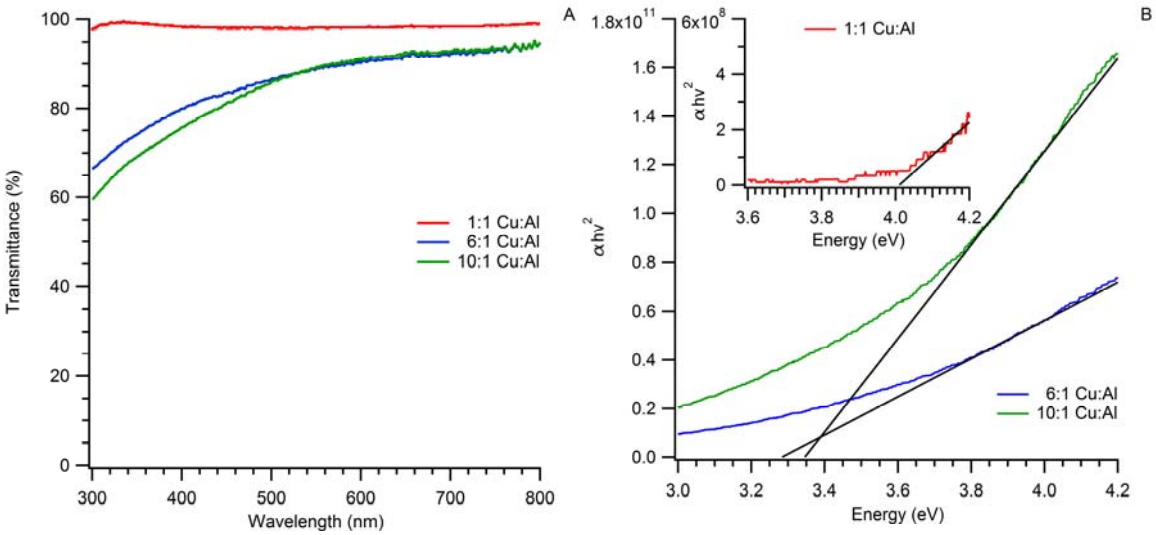

Figure 3.17: Figure A. shows the UV-Vis spectra of several different Cu:Al ratio films. B. show the direct optical band gap Tauc plots for the UV-Vis spectra in figure A.

The UV-Vis spectra show a high degree of transparency, indicative of a large optical band

gap. The associated Tauc plots show band gaps of 4.01eV, 3.28eV, and 3.35eV for the 1:1, 6:1, and 10:1 Cu:Al samples respectively. All clearly show a much closer agreement with the copper (I) aluminum oxide with its band gap of 3.5eV then with copper (II) aluminum oxide with its band gap of 2.1eV.[87]

The optical band gap provides indirect evidence of the oxidation state of the copper atom, but as with the investigation into the copper oxide, XPS provides a more direct measurement of the copper oxidation state. Figure 3.18 is the XPS spectrum for a 6:1 Cu:Al sample, and it shows remarkable similarity to the XPS spectrum of the copper oxide. The major difference is the appearance of the aluminum 2p peak on the right of the spectrum.

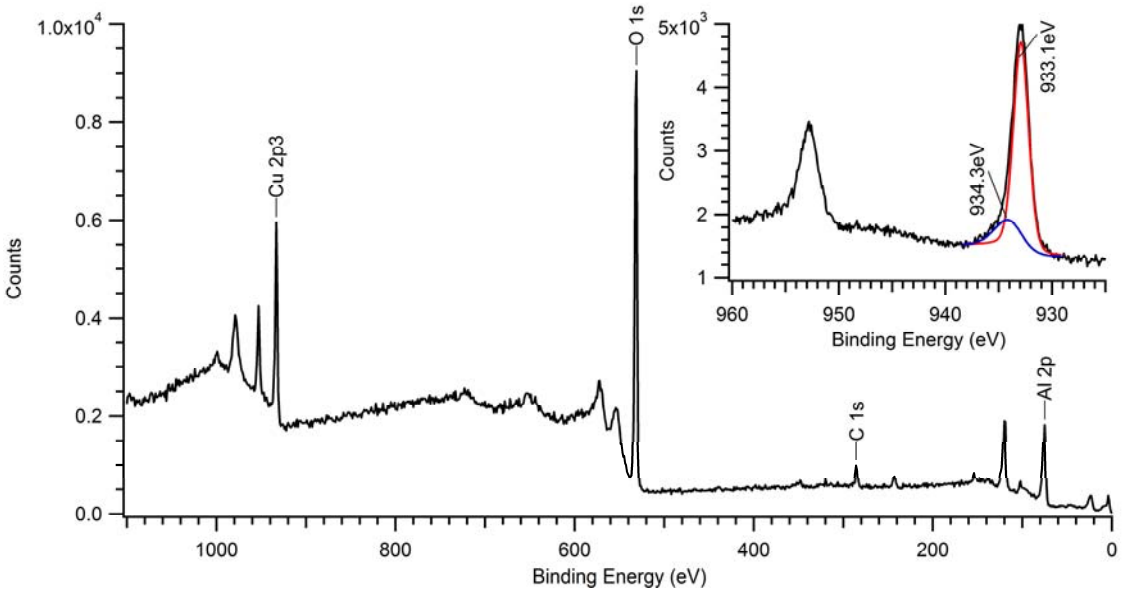

Figure 3.18: XPS spectrum for deposited copper aluminum oxide. The inset shows an enlarged portion of the lower survey spectrum. The red trace is a fit to a Cu(I) species and represents 80% of the deposited material. The blue trace is a fit to a $Cu_x(OH)_y$ species and represents 20% of the material.

The fit to the $Cu2p_{3/2}$ peak is also very similar showing a fit to a copper (I) species and a

$Cu_x(OH)_y$ species. The Auger depth profile is also remarkably similar to its copper oxide predecessor. The film shows elemental uniformity throughout the depth of the film. There is very little carbon incorporation into the film, and the film smoothly transitions into the silicon substrate. (Figure 3.19).

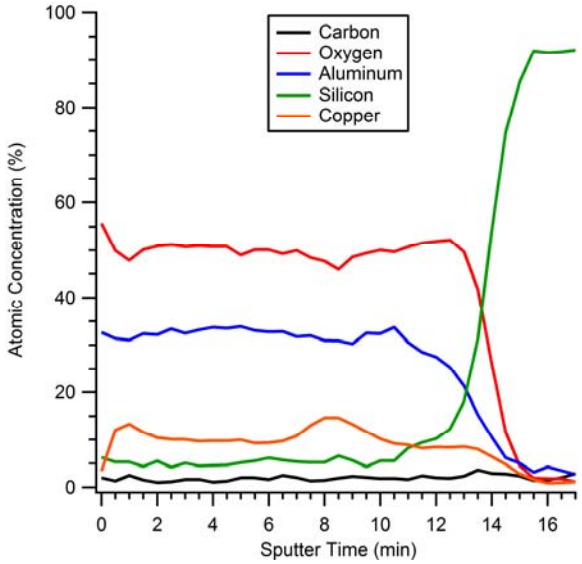

Figure 3.19: Auger depth profile of a copper aluminum oxide ALD film.

The films of copper aluminum oxide have been shown to have copper (I) as their primary component. That is the first method of confirming that the material formed in $CuAlO_2$. The second is looking at the elemental ratio of the components. This proved difficult as techniques such as EDS, WDS, and XPS provided conflicting elemental information. For a 6:1 Cu:Al deposition ratio film EDS gives a Cu:Al ratio of 0.97:1 while WDS and XPS give ratios of 0.54:1 and 0.43:1 respectively. Ideally, a technique that gives elemental information without having to rely on standards, as these three techniques do, would provide a known reference of comparison to gauge the applicablity of these other

elemental techniques.

Rutherford backscattering spectrometery would provide such a reference, however these copper aluminum oxide films are traditionally deposited on pieces of silicon wafer. Silicon has a higher atomic number than aluminum, therefore the aluminum signal would be difficult, if not impossible, to analyze under the silicon background. It was necessary to find usable non-silicon substrates to deposite films on. Out of the limited range of commercially available substrates single crystal magnesium oxide and pyroletic boron nitride were chosen as ALD substrates. Figure 3.20 shows the resulting RBS spectra.

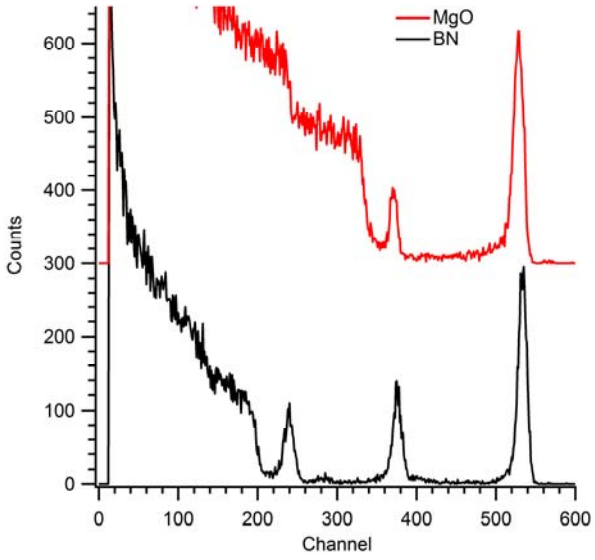

Figure 3.20: RBS spectra of copper aluminum oxide ALD films deposited on BN and MgO. The spectra have been offset for clarity.

The spectra show clear peaks for the copper and aluminum species. The boron nitride even shows the oxygen peak. The elemental concentrations were calculated by fitting a Gaussian curve to each peak to calculate area (A), and using the area to calculate atomic ratios via

equation 3.1, where Z is atomic number.[108]

$$\frac{C_{Cu}}{C_{Al}} = \frac{A_{Cu}/Z_{Cu}^2}{A_{Al}/Z_{Al}^2} \tag{3.1}$$

This works out to a material formula of $CuAl_{2.47}O_{5.2}$ for the 6:1 Cu:Al ratio film deposited on boron nitride and a formula of $CuAl_{2.41}O_x$ for the same film deposited on magnesium oxide. This agrees well with the XPS and WDS data, which for the boron nitride sample showed formulas of $CuAl_{2.32}O_x$ and $CuAl_{1.85}O_x$ respectively. These answer differ wildly from the $CuAl_{0.907}O_x$ formula reported from EDS. The magnesium oxide substrated proved difficult to measure relibly. The insulating nature of the substrate made electrical charging a major issue, which even coating the film in conductive carbon couldn't resolve. Also, while all the non-RBS techniques do report elemental information for oxygen it should be regarded with sketicism, as it is a very light element and therefore difficult to measure relably with those methods.

3.5 Conclusion: Films of copper (I) oxide and copper (I) aluminum oxide have been successfully deposited using a copper acetylacetonate and ozone ALD process. Spectroscopic ellispometery was used to confirm a constant film thickness per cycle and self-limiting deposition behavior for each of the precursors. Being TCOs both materials were mostly transparent across the visible region and both had optical band gaps consistent with a copper (I) species being deposited. The copper (I) oxidation state was confirmed via XPS, which along with Auger spectroscopy confirmed the elemental purity of the deposited films.

The following diagrams are not at the correct scale in order to meet graduate school formatting requirements. Correctly scaled diagrams (i.e. useful ones) can be requested from Professor Wayne Gladfelter (wlg@umn.edu).

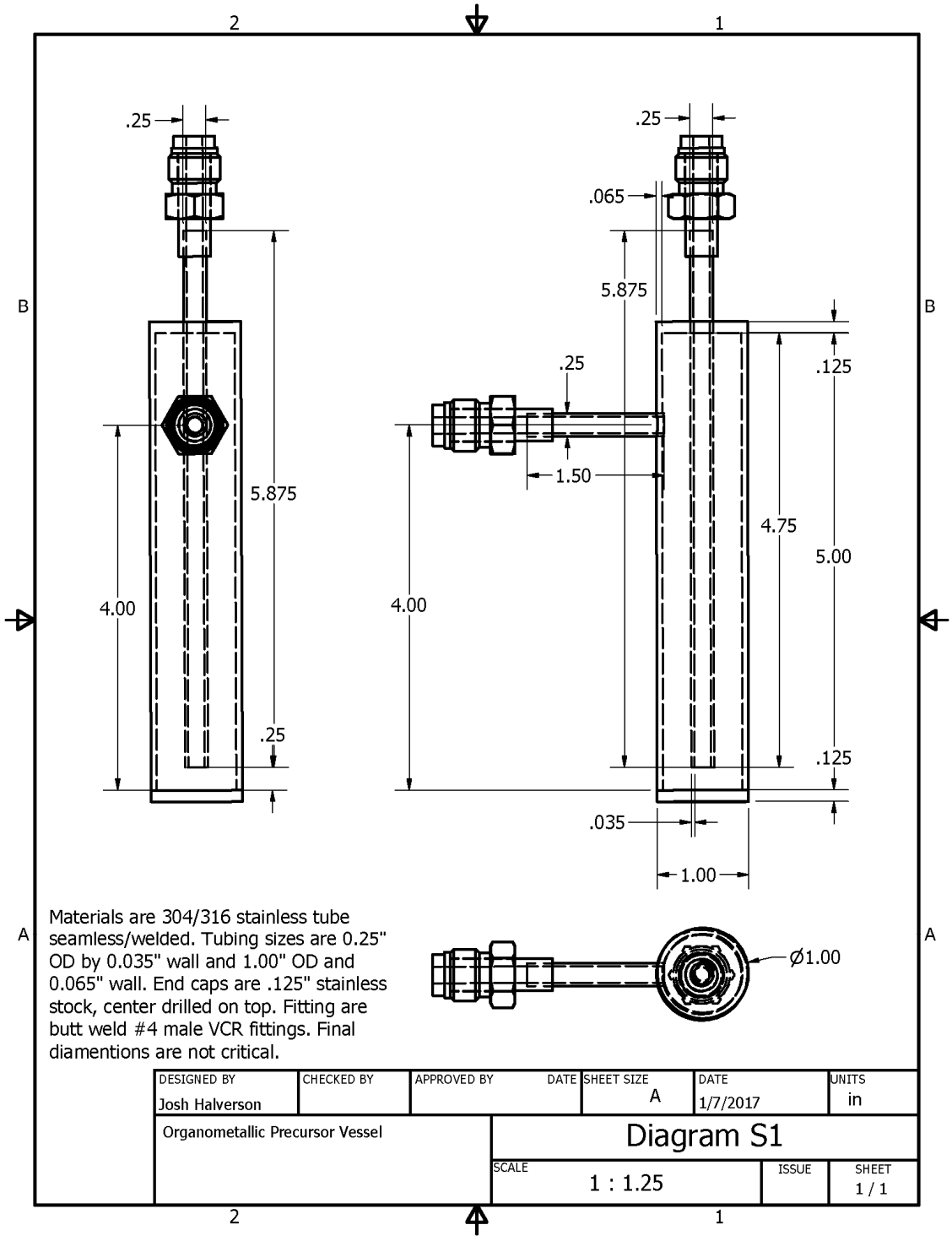

The following diagrams are not at the correct scale in order to meet graduate school formatting requirements. Correctly scaled diagrams (i.e. useful ones) can be requested from Professor Wayne Gladfelter (wlg@umn.edu).

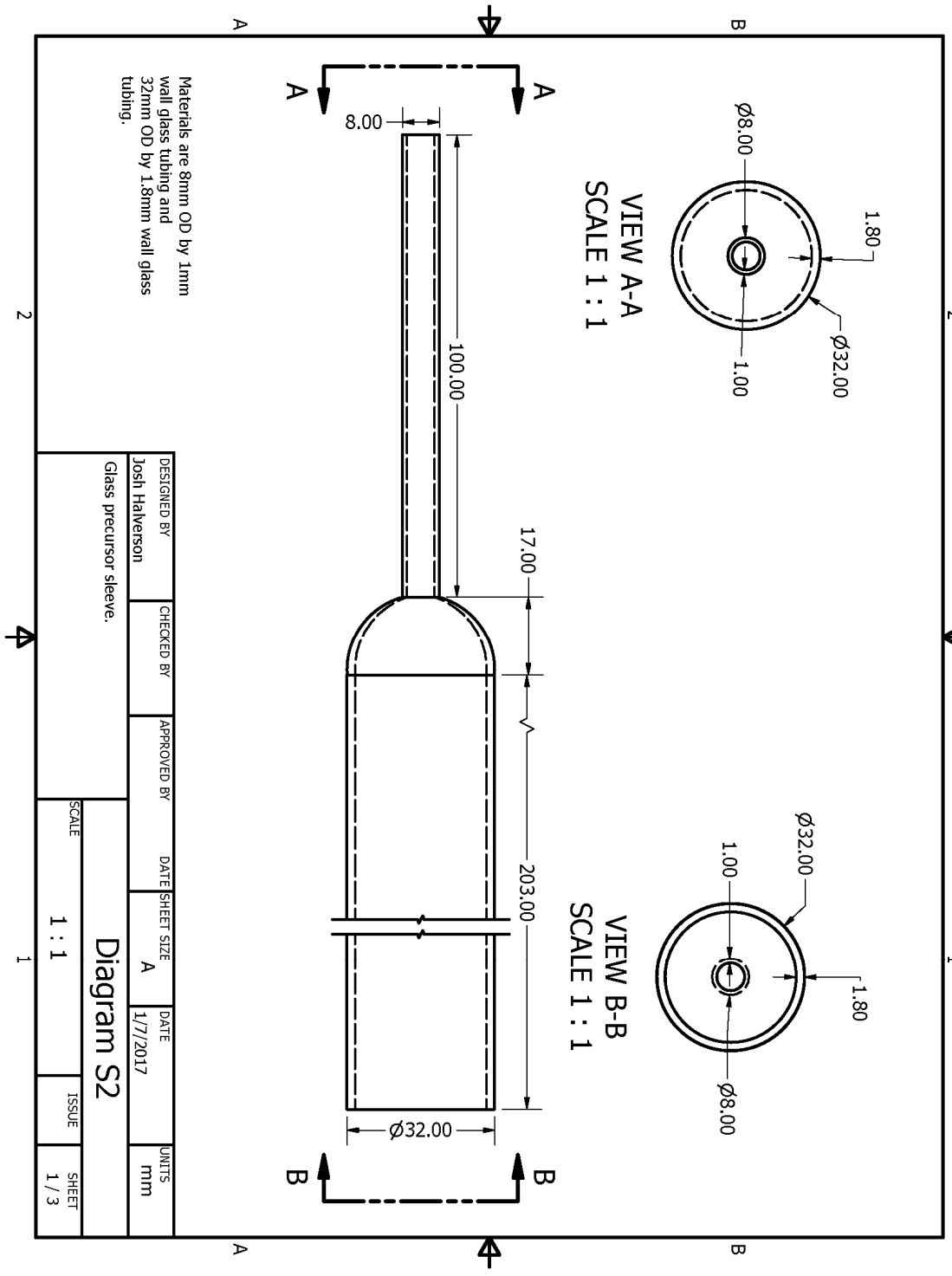

The following diagrams are not at the correct scale in order to meet graduate school formatting requirements. Correctly scaled diagrams (i.e. useful ones) can be requested from Professor Wayne Gladfelter (wlg@umn.edu).

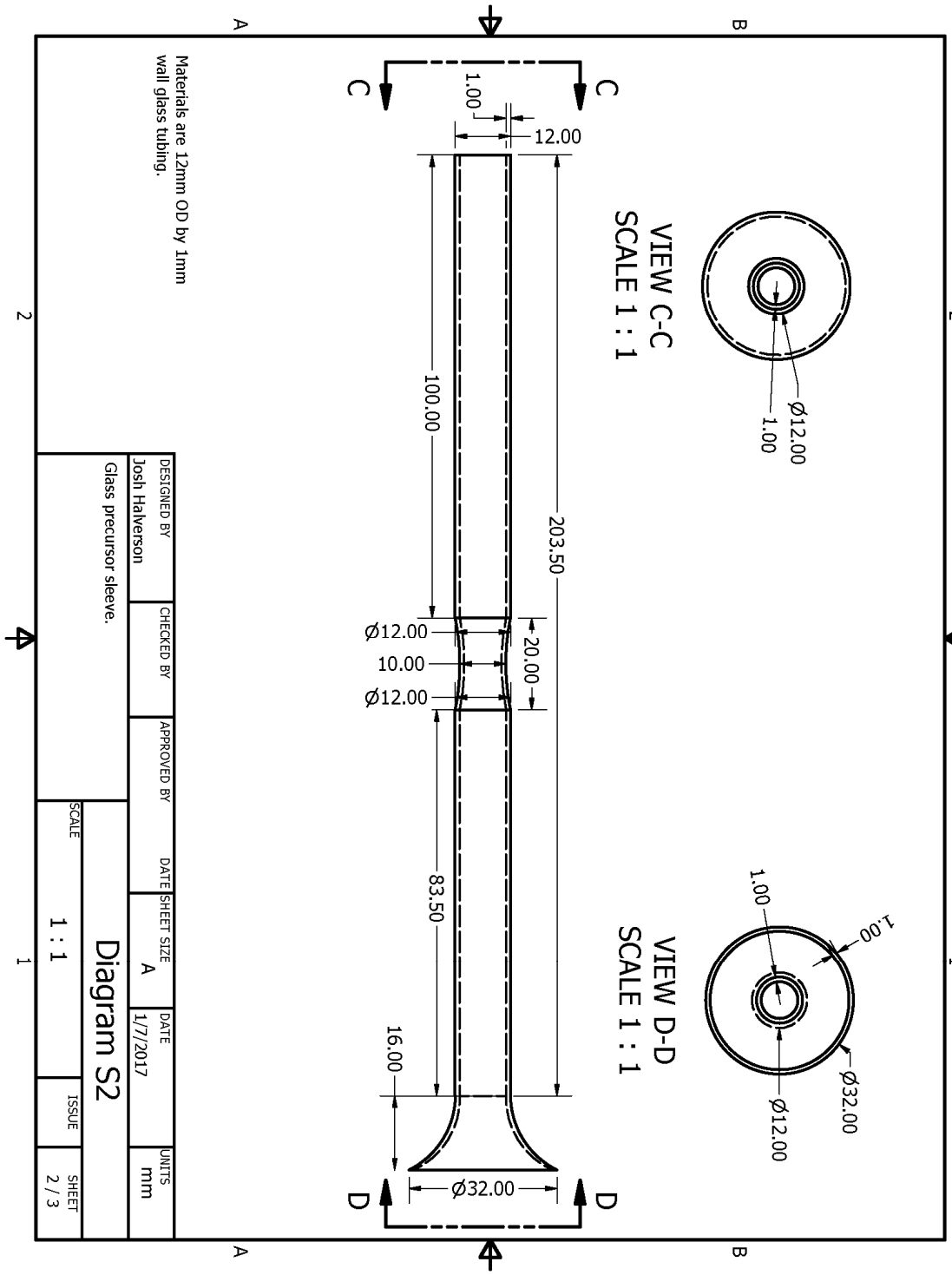

The following diagrams are not at the correct scale in order to meet graduate school formatting requirements. Correctly scaled diagrams (i.e. useful ones) can be requested from Professor Wayne Gladfelter (wlg@umn.edu).

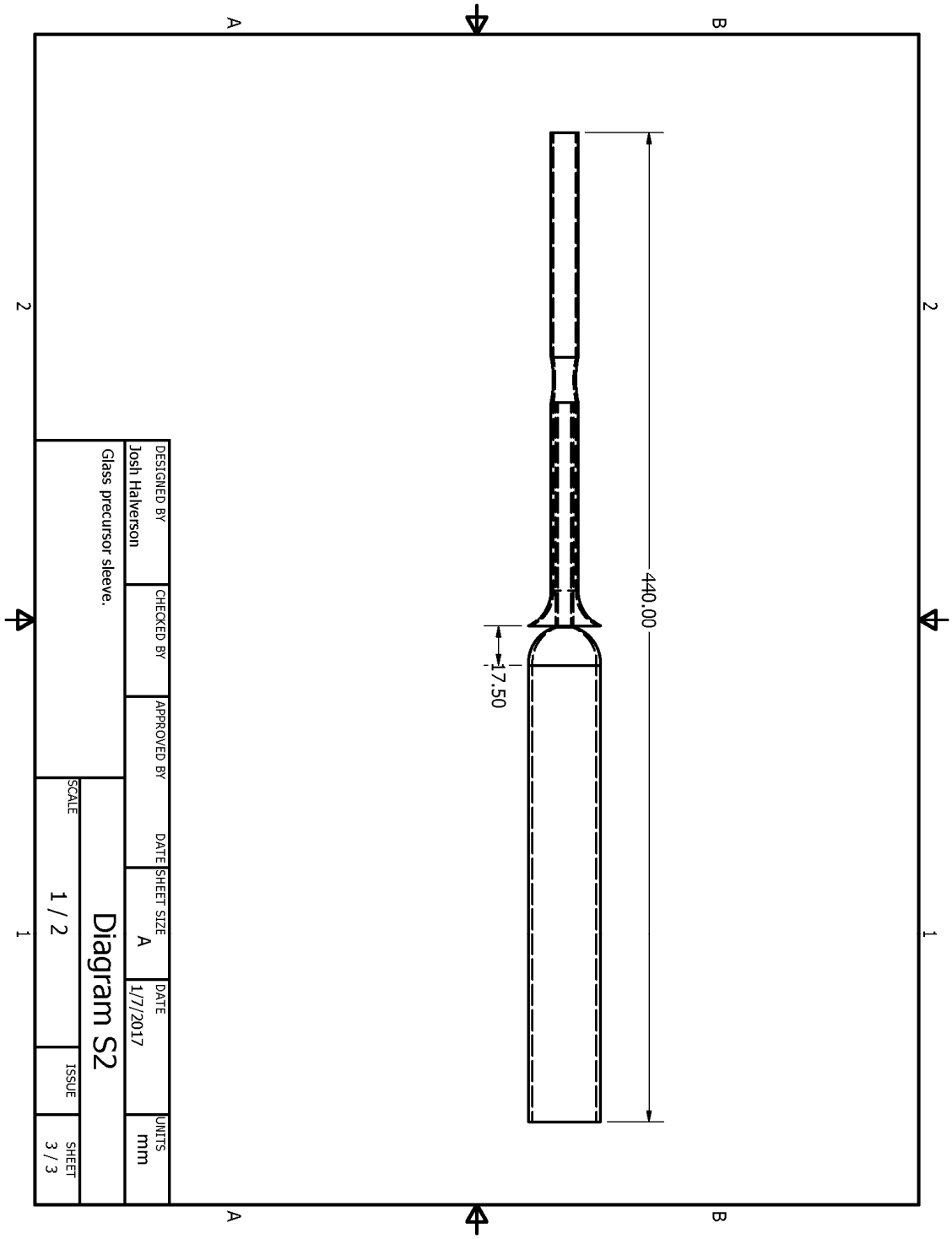

The following diagrams are not at the correct scale in order to meet graduate school formatting requirements. Correctly scaled diagrams (i.e. useful ones) can be requested from Professor Wayne Gladfelter (wlg@umn.edu).

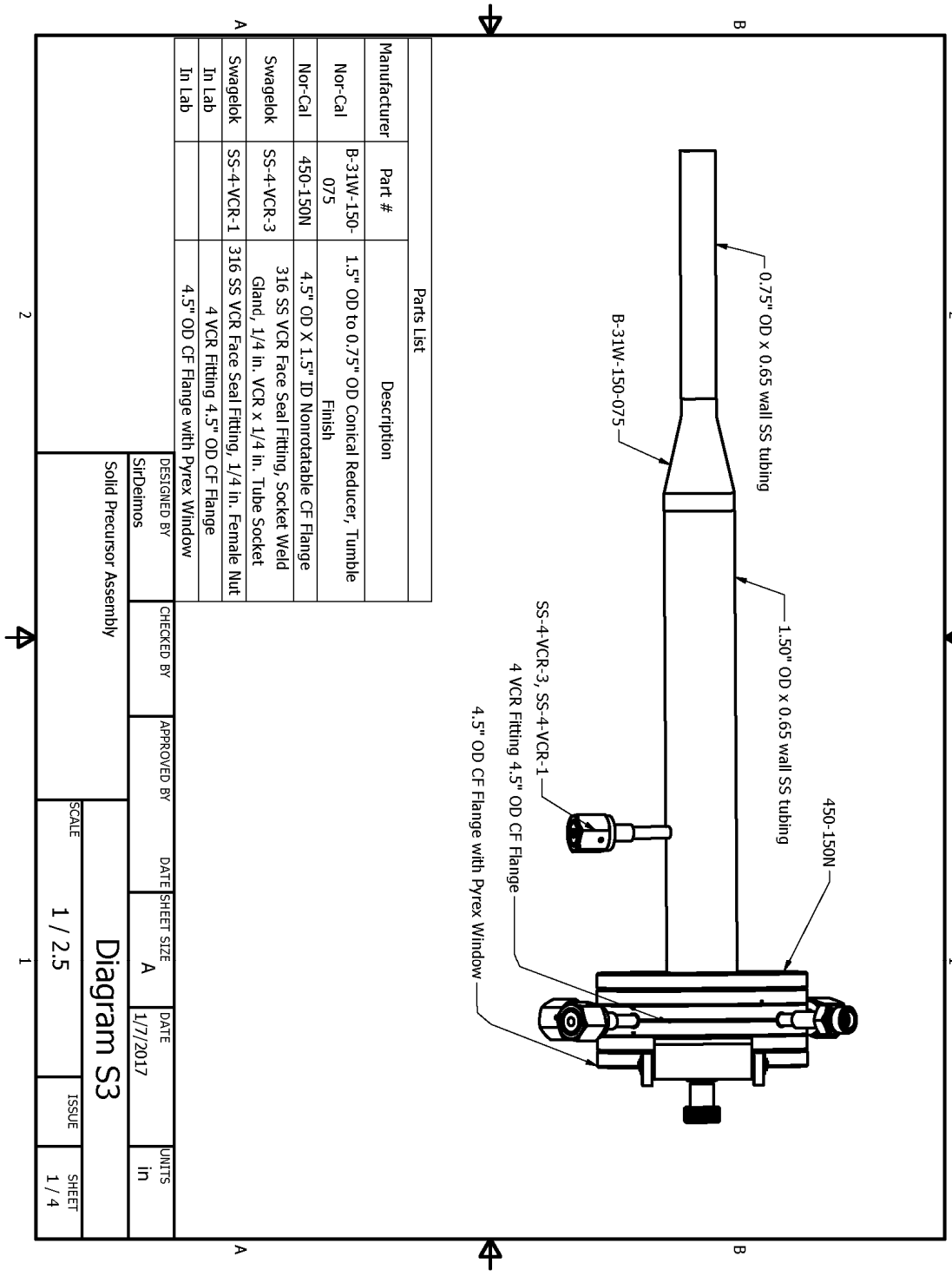

Parts List

	Manufacturer	Part #	Description
	Nor-Cal	B-31W-150-075	1.5" OD to 0.75" OD Conical Reducer, Tumble Finish
	Nor-Cal	450-150N	4.5" OD X 1.5" ID Nonrotatable CF Flange
	Swagelok	SS-4-VCR-3	316 SS VCR Face Seal Fitting, Socket Weld Gland, 1/4 in. VCR x 1/4 in. Tube Socket
	Swagelok	SS-4-VCR-1	316 SS VCR Face Seal Fitting, 1/4 in. Female Nut
	In Lab		4 VCR Fitting 4.5" OD CF Flange
	In Lab		4.5" OD CF Flange with Pyrex Window

DESIGNED BY	CHECKED BY	APPROVED BY	DATE	SHEET SIZE	DATE	UNITS
SirDeimos				A	1/7/2017	in

Solid Precursor Assembly

Diagram S3

SCALE	ISSUE	SHEET
1 / 2.5		1 / 4

The following diagrams are not at the correct scale in order to meet graduate school formatting requirements. Correctly scaled diagrams (i.e. useful ones) can be requested from Professor Wayne Gladfelter (wlg@umn.edu).

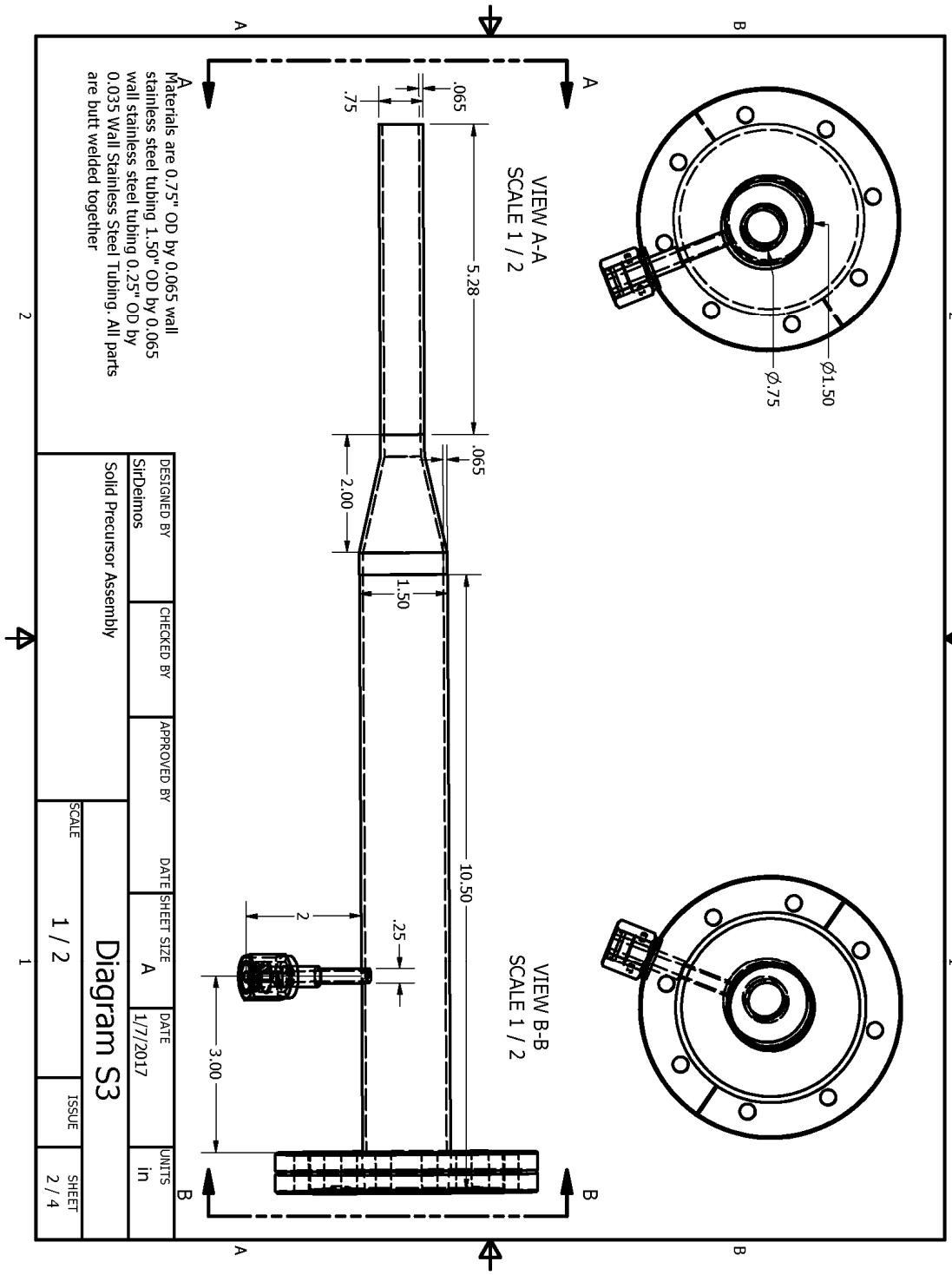

The following diagrams are not at the correct scale in order to meet graduate school formatting requirements. Correctly scaled diagrams (i.e. useful ones) can be requested from Professor Wayne Gladfelter (wlg@umn.edu).

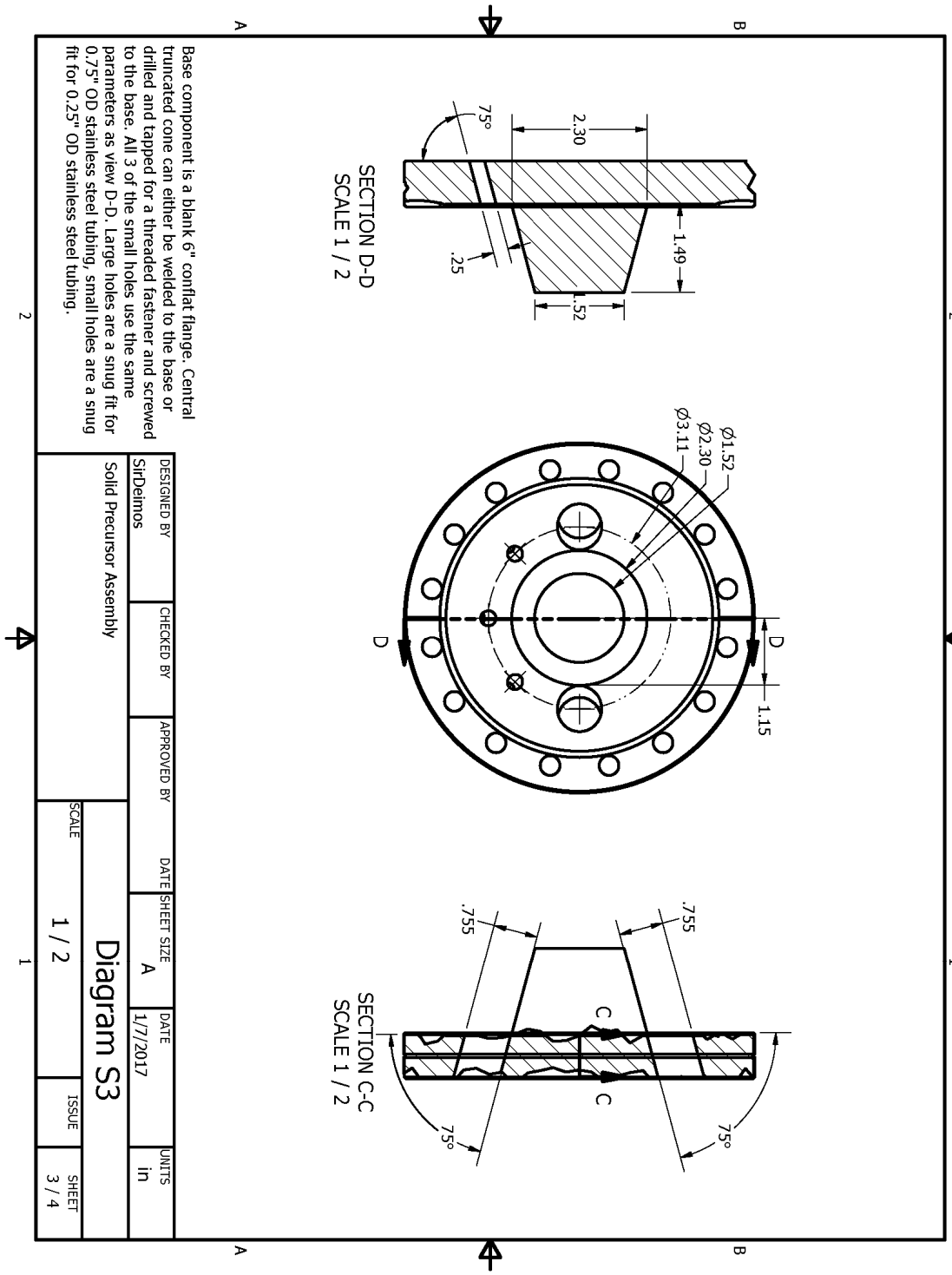

The following diagrams are not at the correct scale in order to meet graduate school formatting requirements. Correctly scaled diagrams (i.e. useful ones) can be requested from Professor Wayne Gladfelter (wlg@umn.edu).

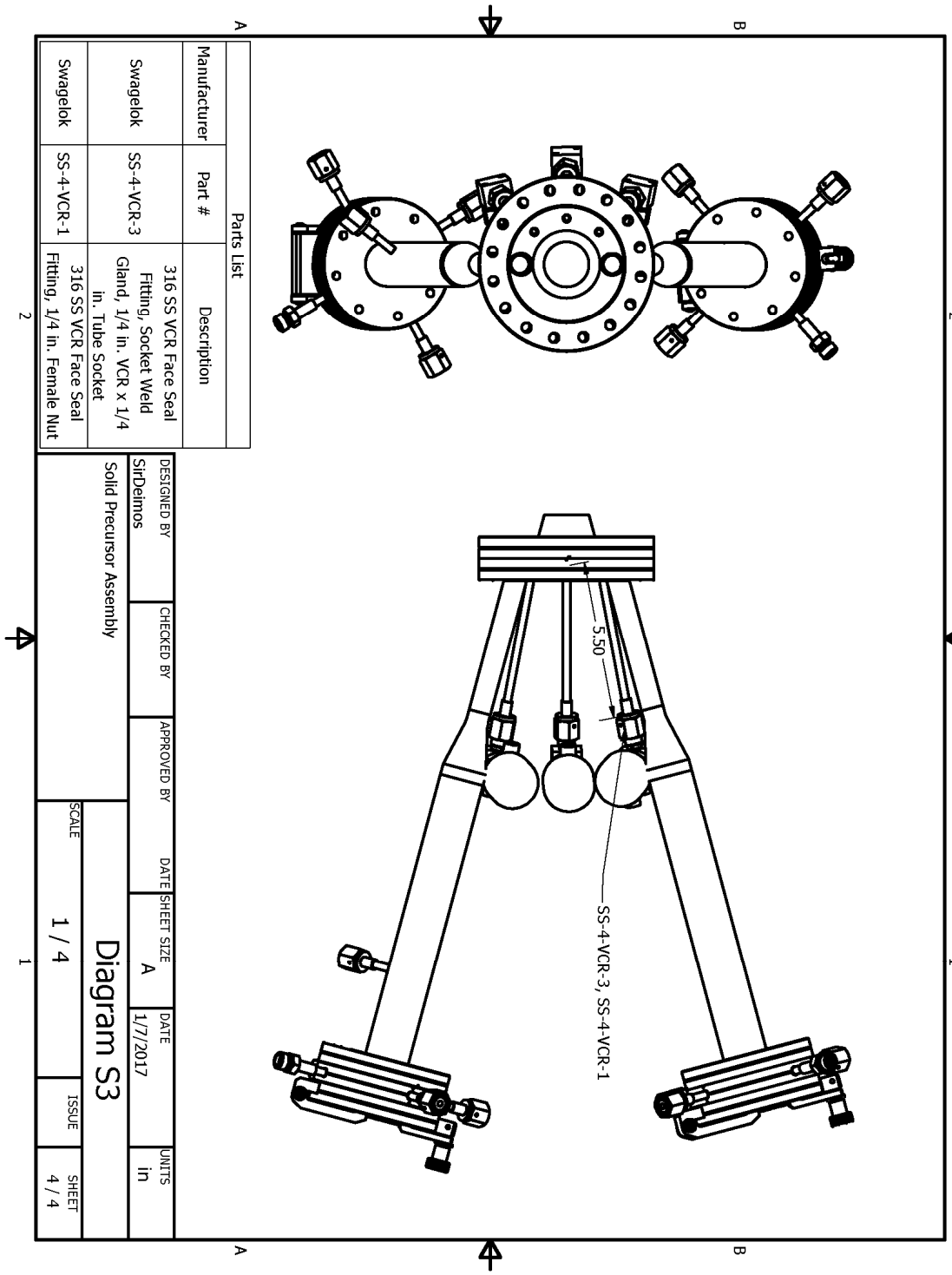

Parts List

Part #	Description	Manufacturer
SS-4-VCR-3	316 SS VCR Face Seal Fitting, Socket Weld Gland, 1/4 in. VCR x 1/4 in. Tube Socket	Swagelok
SS-4-VCR-1	316 SS VCR Face Seal Fitting, 1/4 in. Female Nut	Swagelok

DESIGNED BY	SirDeimos
CHECKED BY	
APPROVED BY	
DATE	1/7/2017
SHEET SIZE	A
UNITS	in
SCALE	1 / 4
ISSUE	
SHEET	4 / 4

Solid Precursor Assembly

Diagram S3

The following diagrams are not at the correct scale in order to meet graduate school formatting requirements. Correctly scaled diagrams (i.e. useful ones) can be requested from Professor Wayne Gladfelter (wlg@umn.edu).

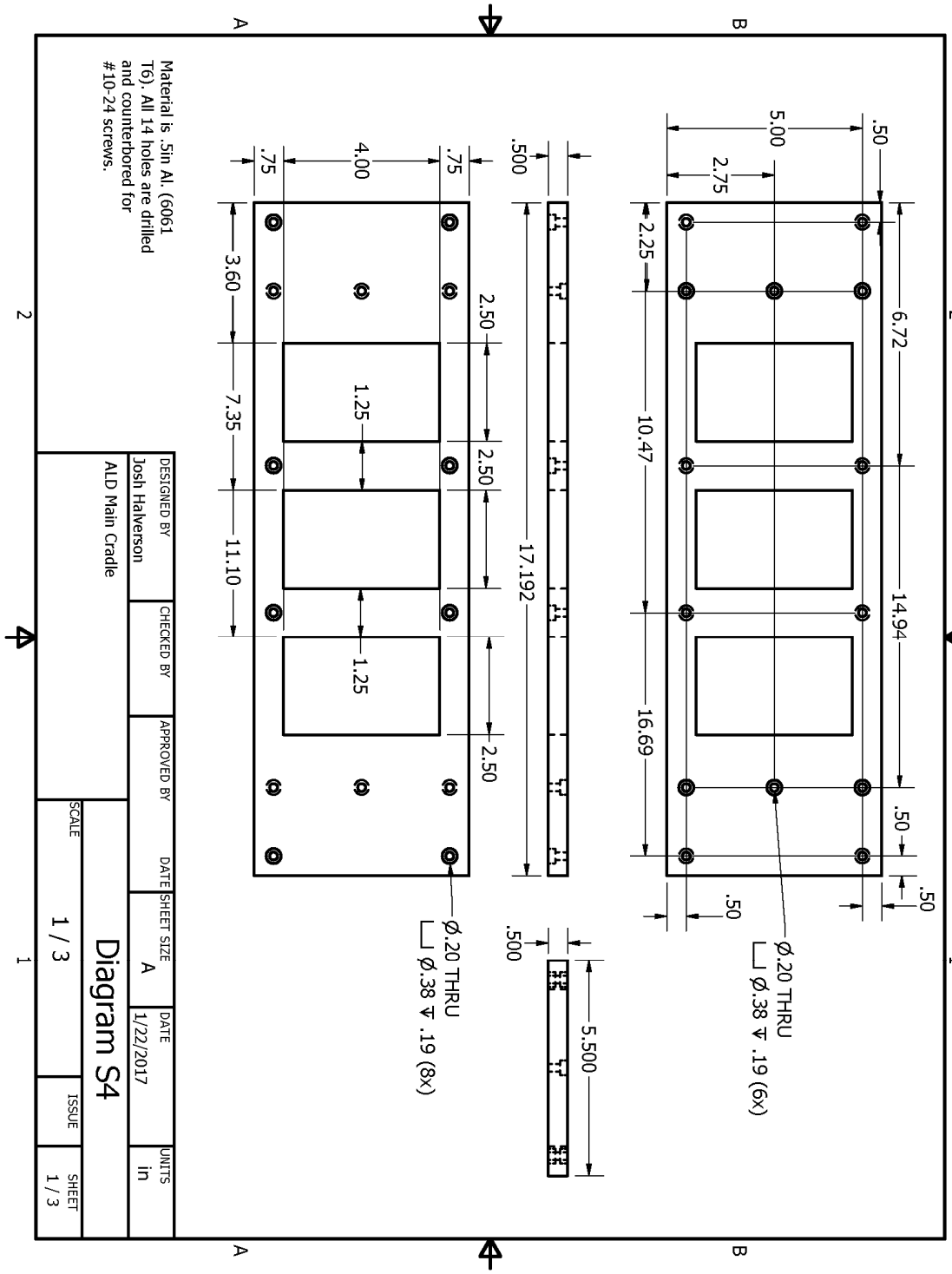

The following diagrams are not at the correct scale in order to meet graduate school formatting requirements. Correctly scaled diagrams (i.e. useful ones) can be requested from Professor Wayne Gladfelter (wlg@umn.edu).

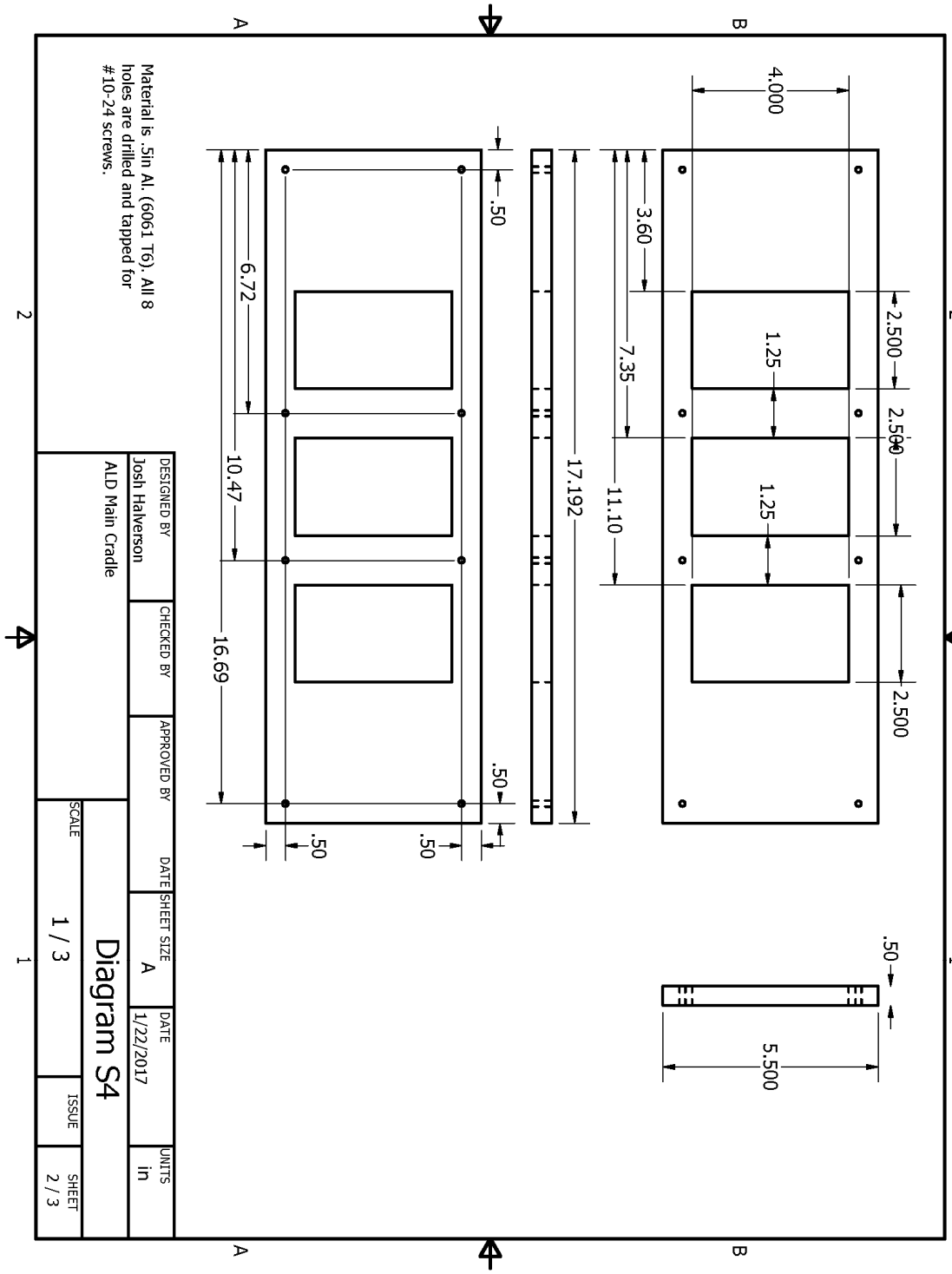

The following diagrams are not at the correct scale in order to meet graduate school formatting requirements. Correctly scaled diagrams (i.e. useful ones) can be requested from Professor Wayne Gladfelter (wlg@umn.edu).

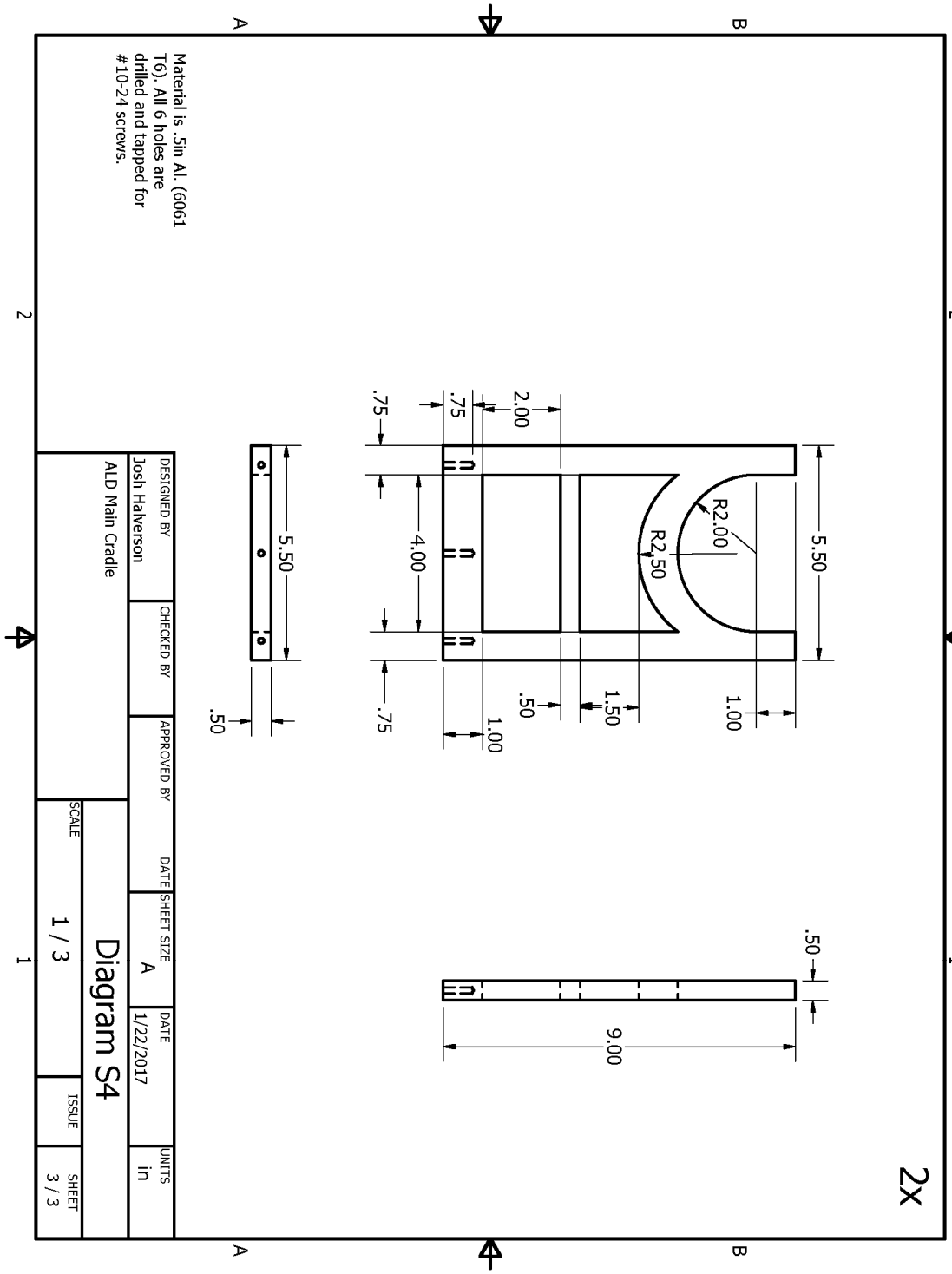

The following diagrams are not at the correct scale in order to meet graduate school formatting requirements. Correctly scaled diagrams (i.e. useful ones) can be requested from Professor Wayne Gladfelter (wlg@umn.edu).

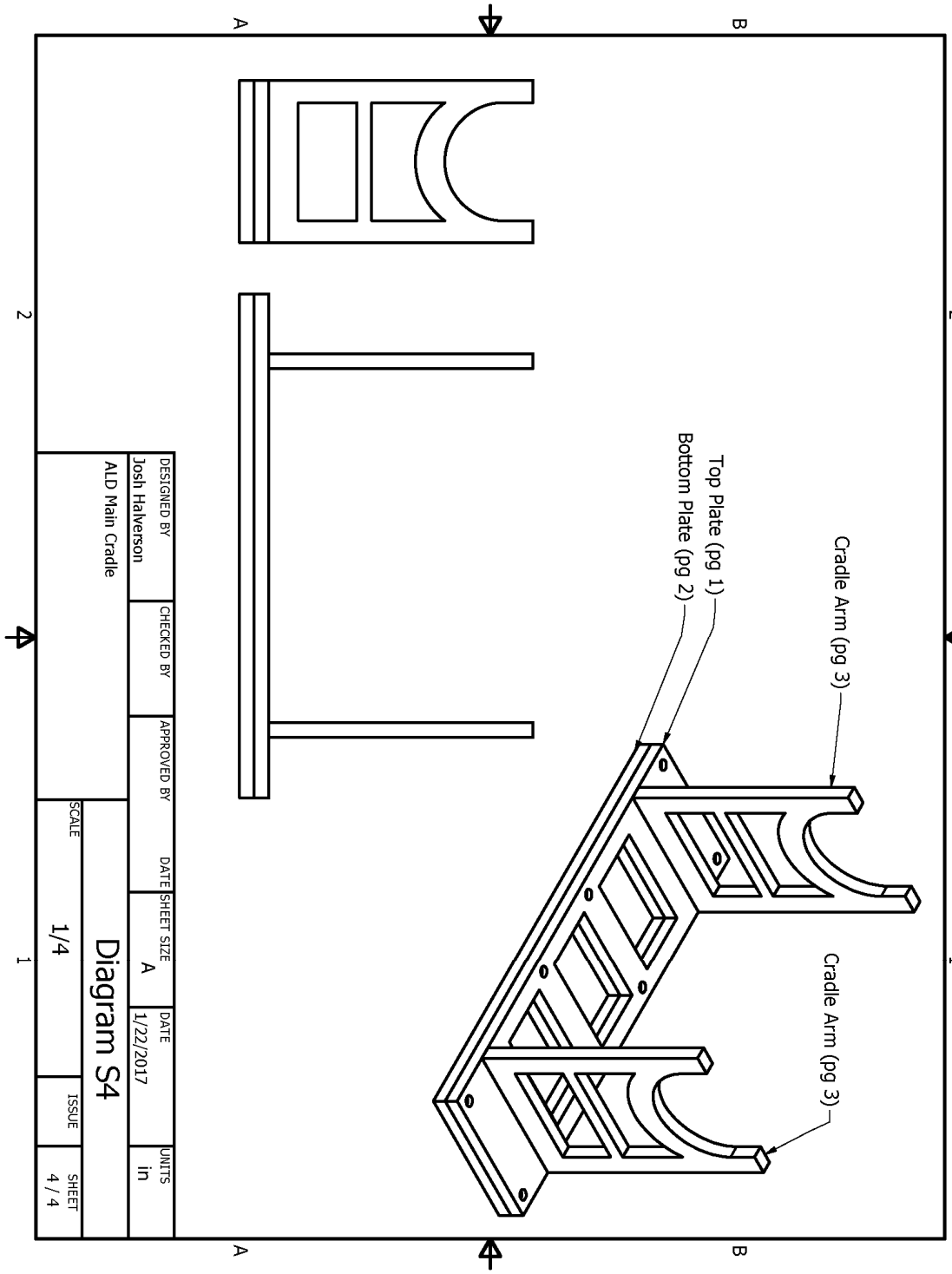

The following diagrams are not at the correct scale in order to meet graduate school formatting requirements. Correctly scaled diagrams (i.e. useful ones) can be requested from Professor Wayne Gladfelter (wlg@umn.edu).

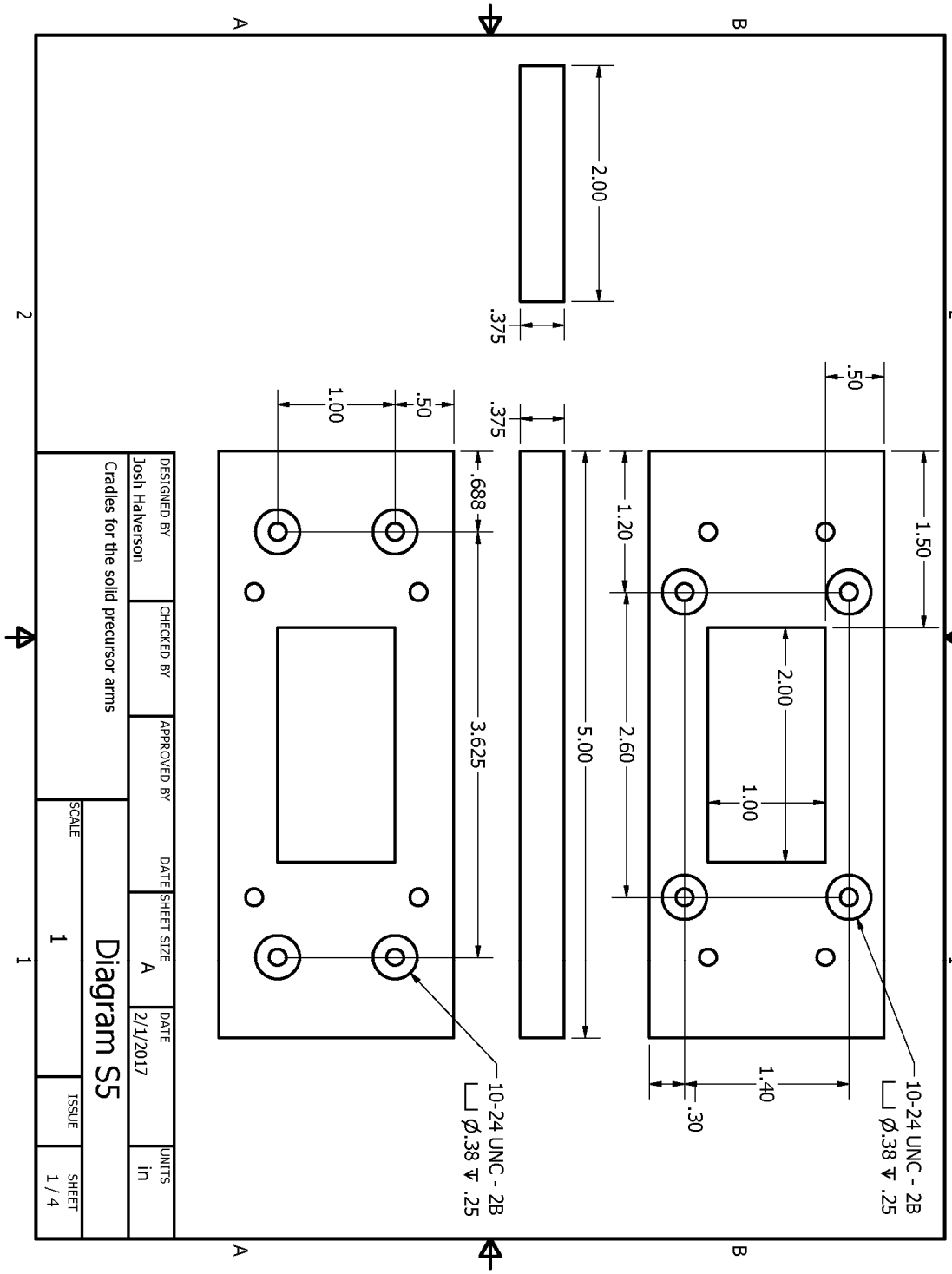

The following diagrams are not at the correct scale in order to meet graduate school formatting requirements. Correctly scaled diagrams (i.e. useful ones) can be requested from Professor Wayne Gladfelter (wlg@umn.edu).

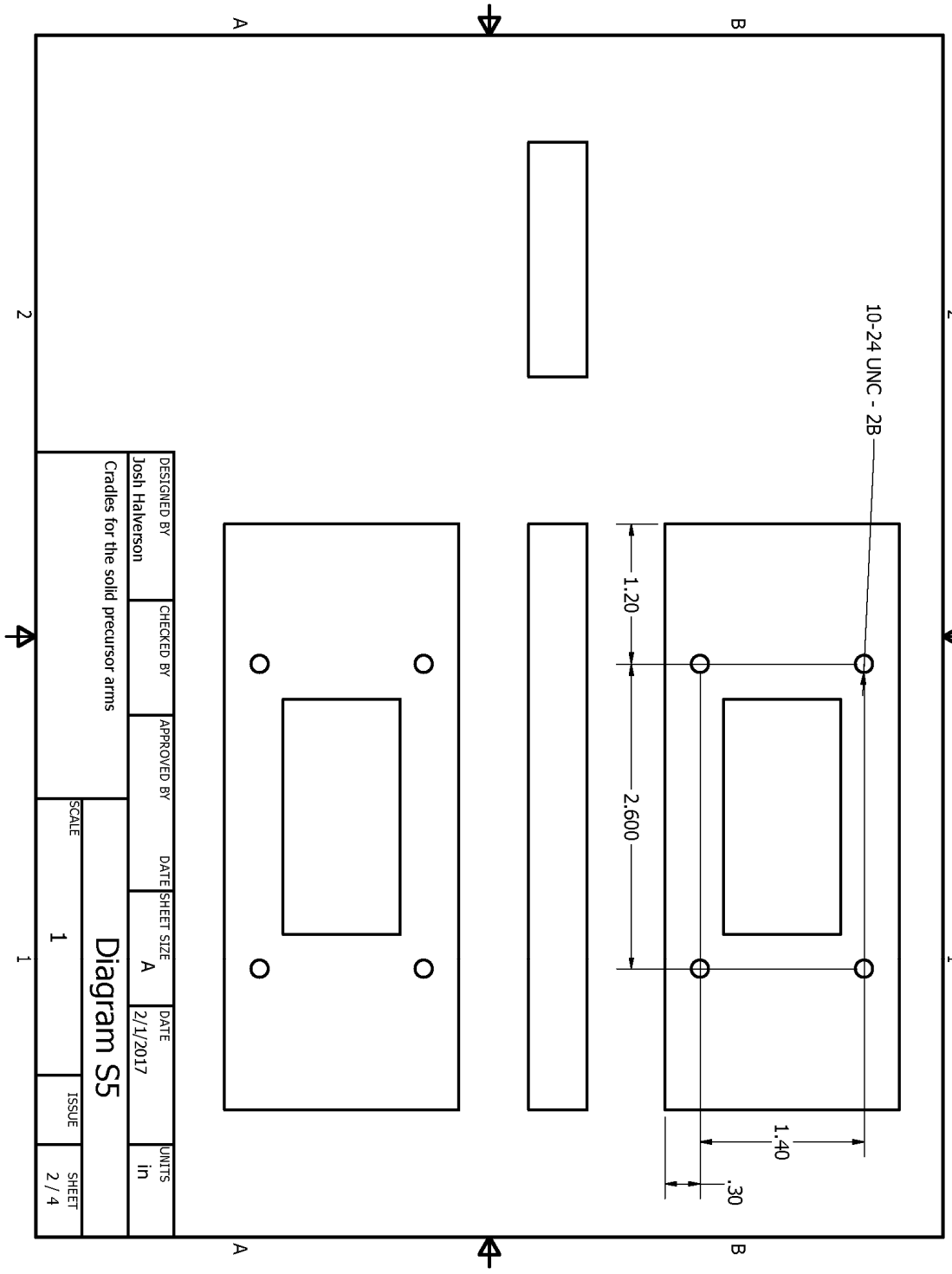

The following diagrams are not at the correct scale in order to meet graduate school formatting requirements. Correctly scaled diagrams (i.e. useful ones) can be requested from Professor Wayne Gladfelter (wlg@umn.edu).

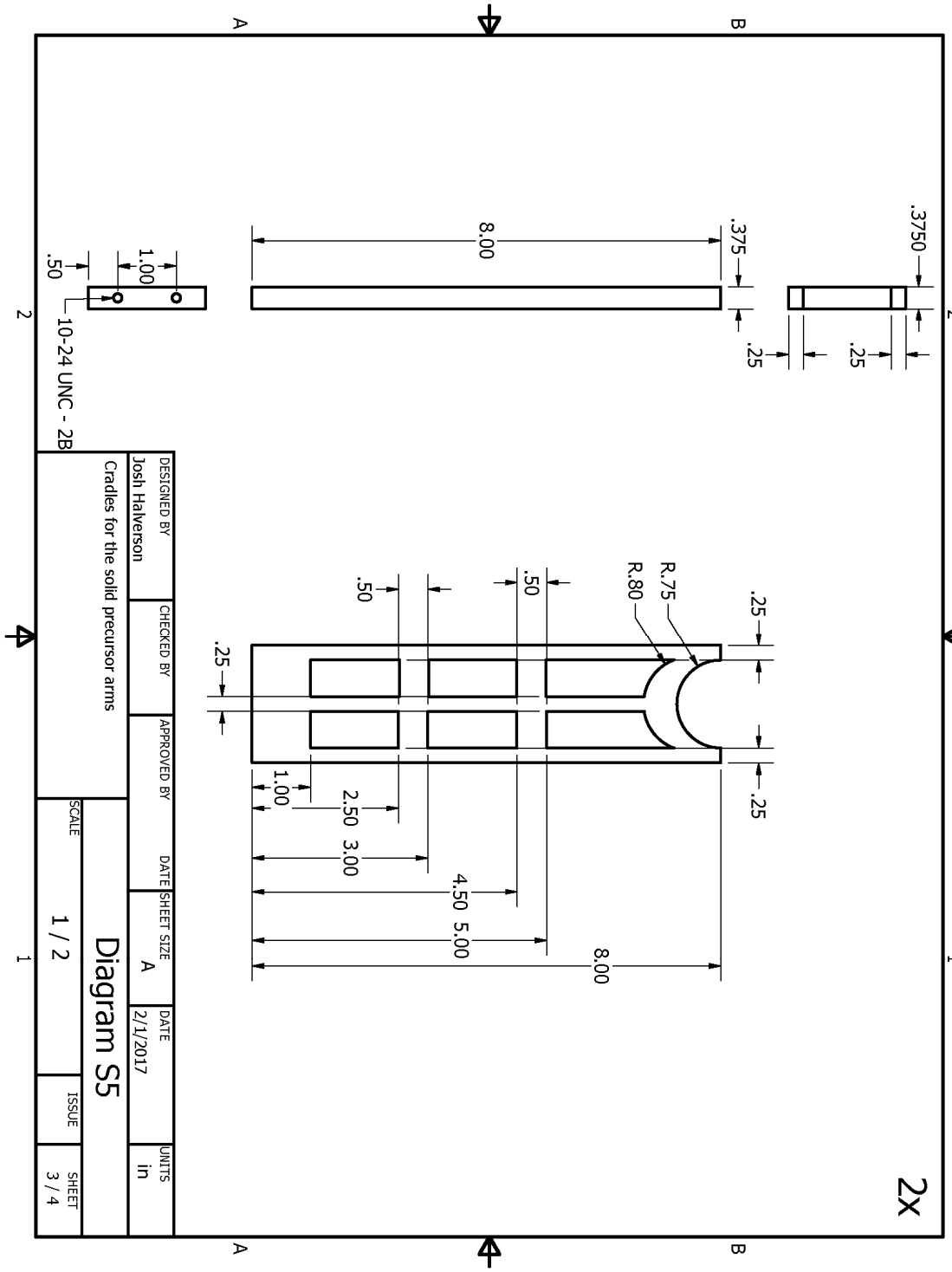

The following diagrams are not at the correct scale in order to meet graduate school formatting requirements. Correctly scaled diagrams (i.e. useful ones) can be requested from Professor Wayne Gladfelter (wlg@umn.edu).

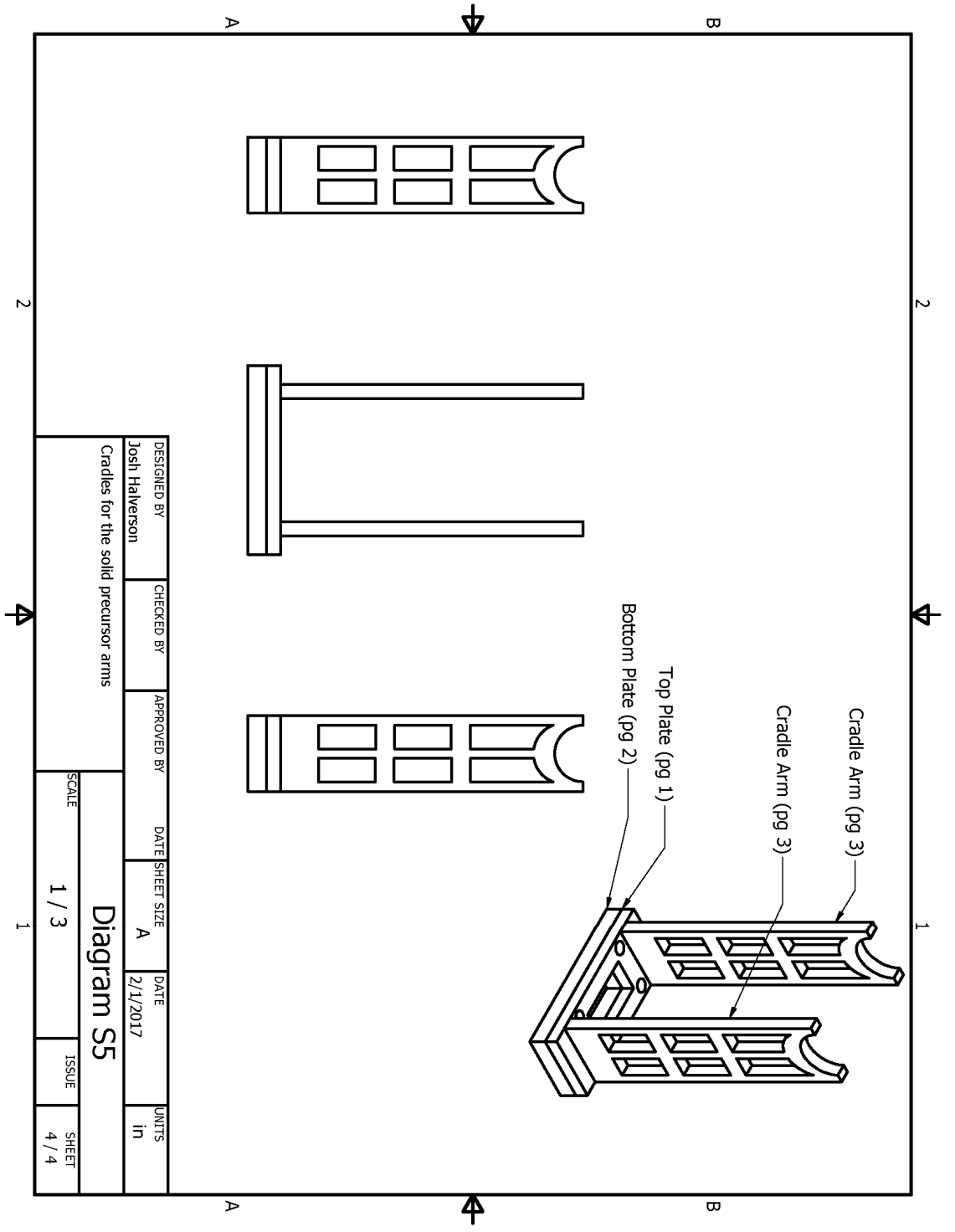

The following diagrams are not at the correct scale in order to meet graduate school formatting requirements. Correctly scaled diagrams (i.e. useful ones) can be requested from Professor Wayne Gladfelter (wlg@umn.edu).

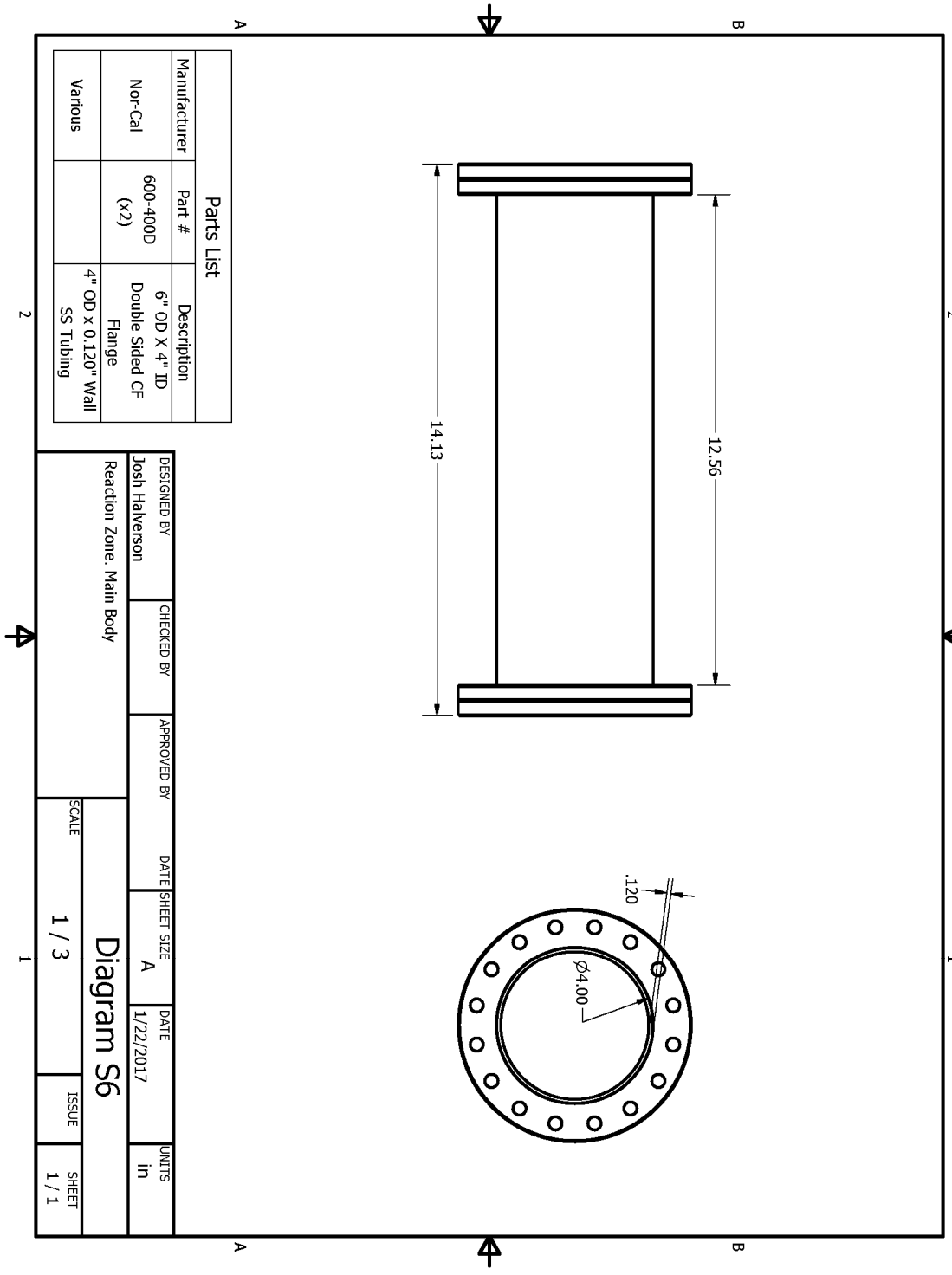

The following diagrams are not at the correct scale in order to meet graduate school formatting requirements. Correctly scaled diagrams (i.e. useful ones) can be requested from Professor Wayne Gladfelter (wlg@umn.edu).

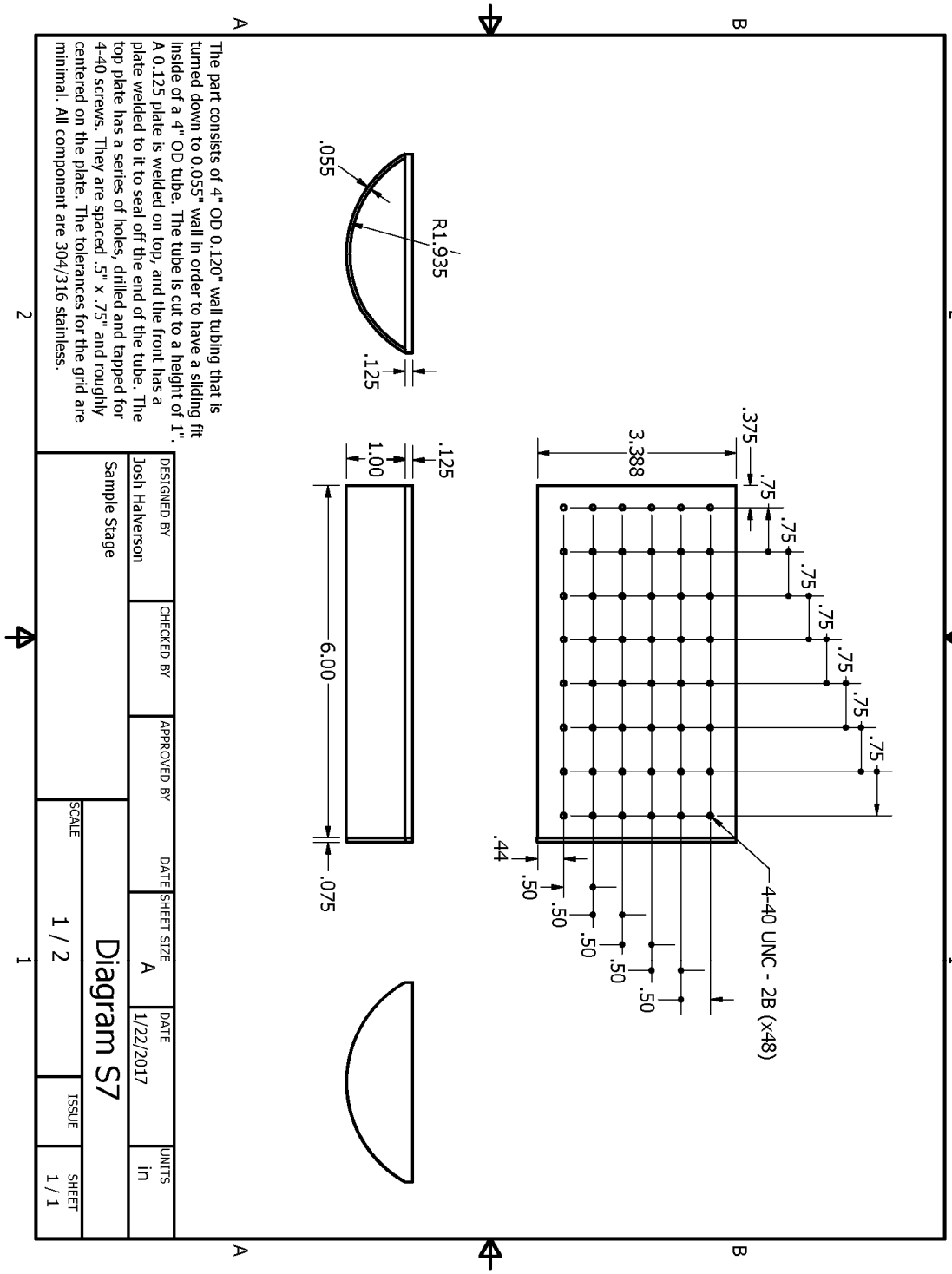

The following diagrams are not at the correct scale in order to meet graduate school formatting requirements. Correctly scaled diagrams (i.e. useful ones) can be requested from Professor Wayne Gladfelter (wlg@umn.edu).

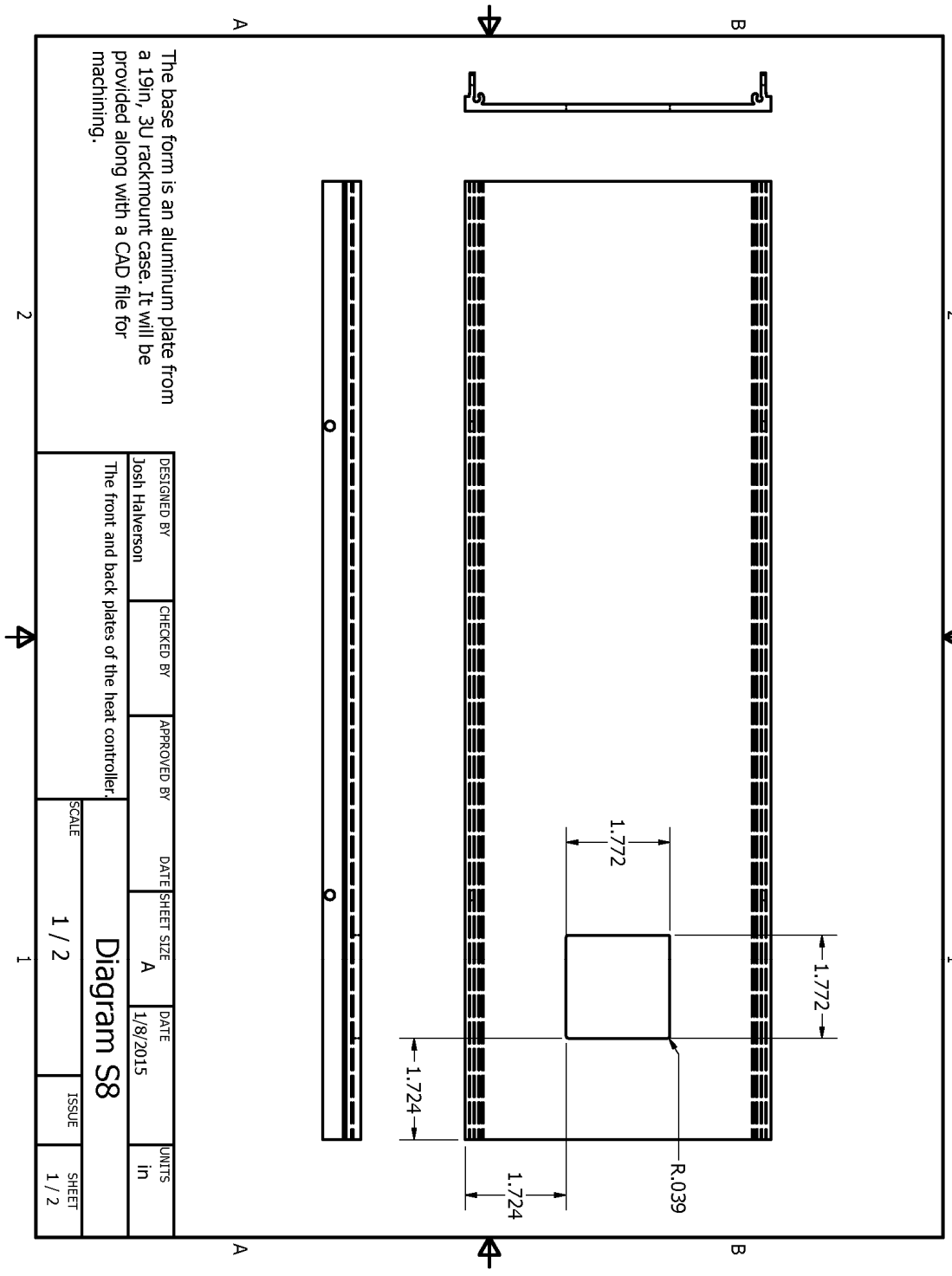

The following diagrams are not at the correct scale in order to meet graduate school formatting requirements. Correctly scaled diagrams (i.e. useful ones) can be requested from Professor Wayne Gladfelter (wlg@umn.edu).

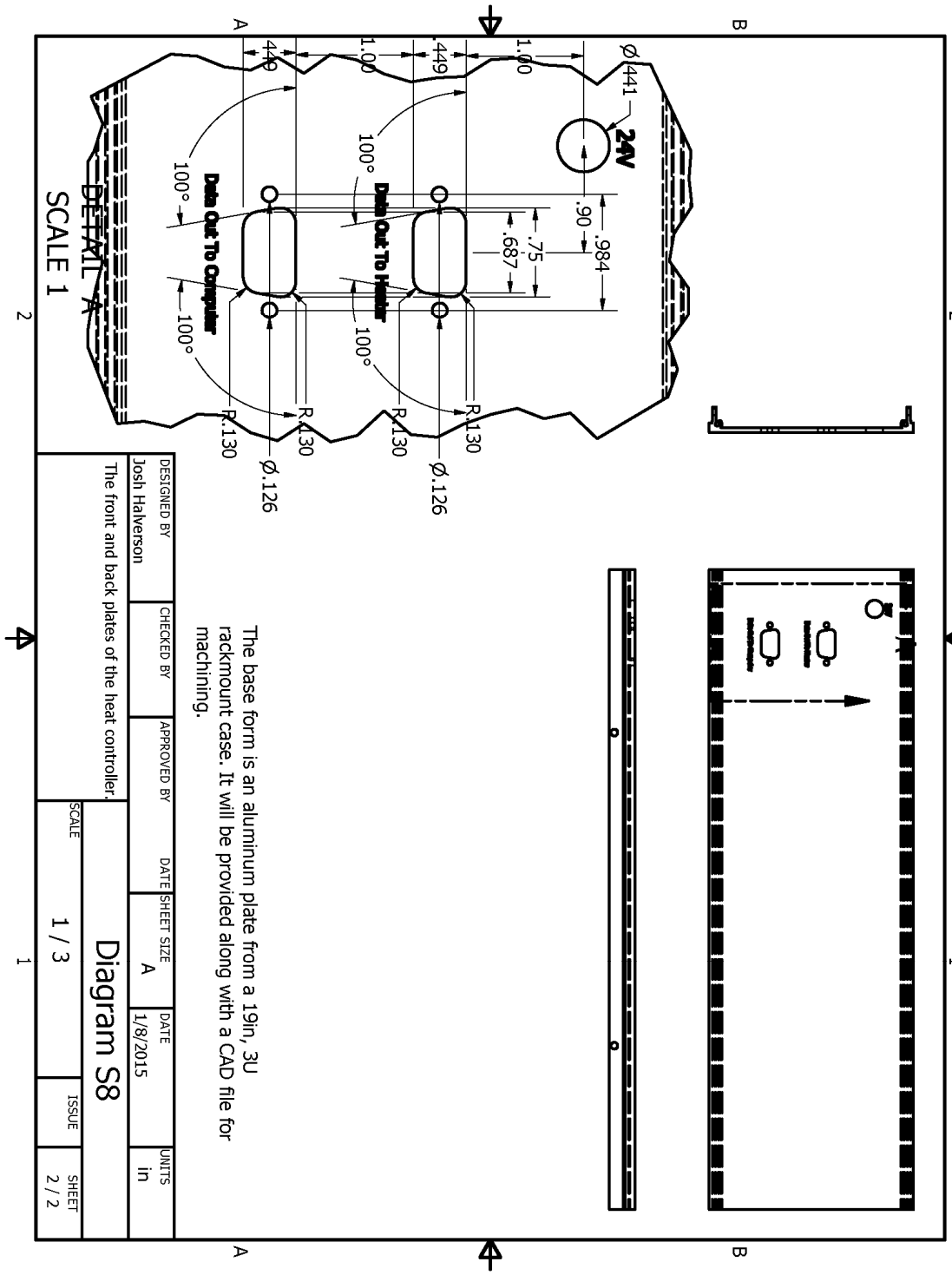

The following diagrams are not at the correct scale in order to meet graduate school formatting requirements. Correctly scaled diagrams (i.e. useful ones) can be requested from Professor Wayne Gladfelter (wlg@umn.edu).

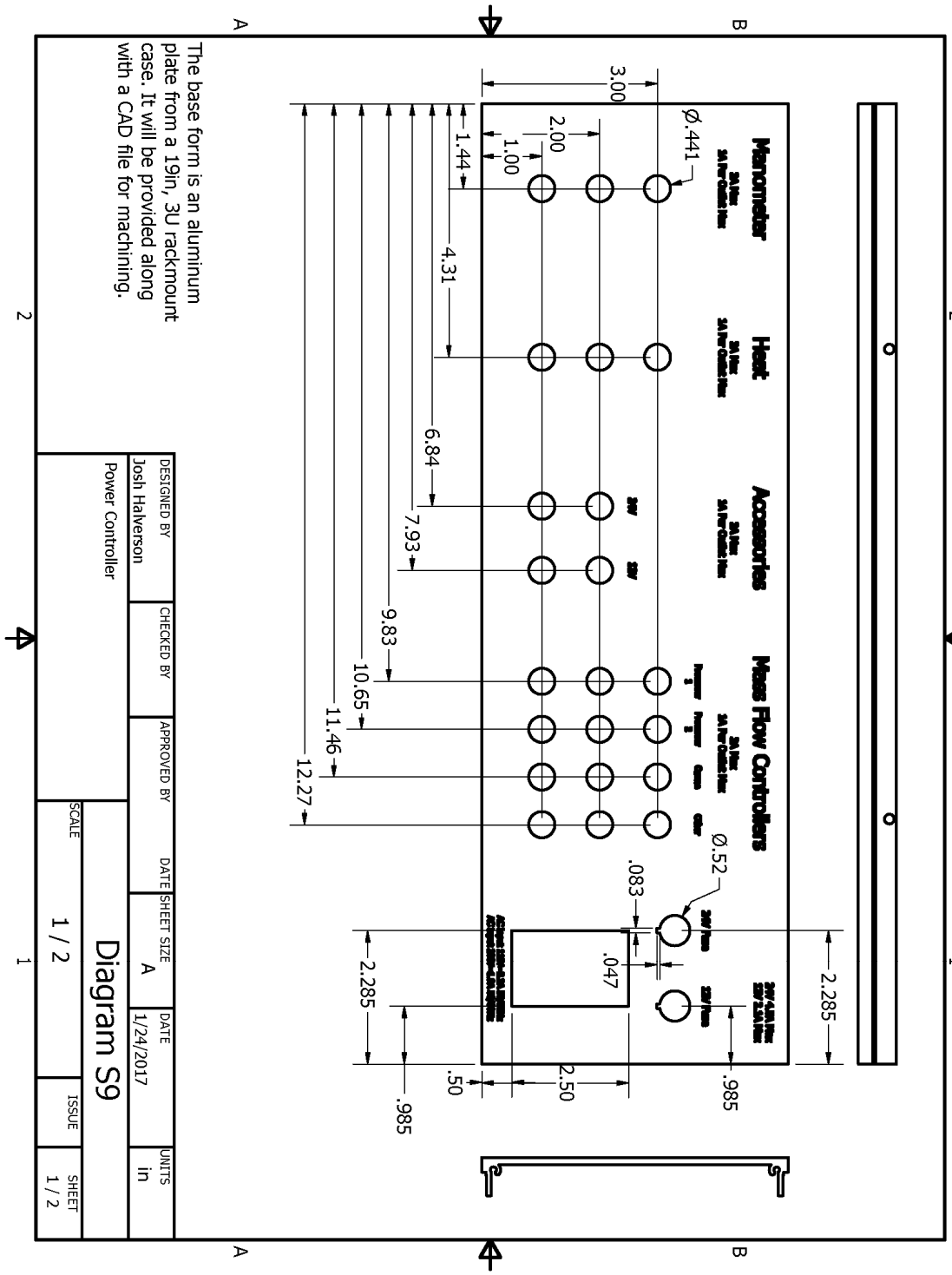

The following diagrams are not at the correct scale in order to meet graduate school formatting requirements. Correctly scaled diagrams (i.e. useful ones) can be requested from Professor Wayne Gladfelter (wlg@umn.edu).

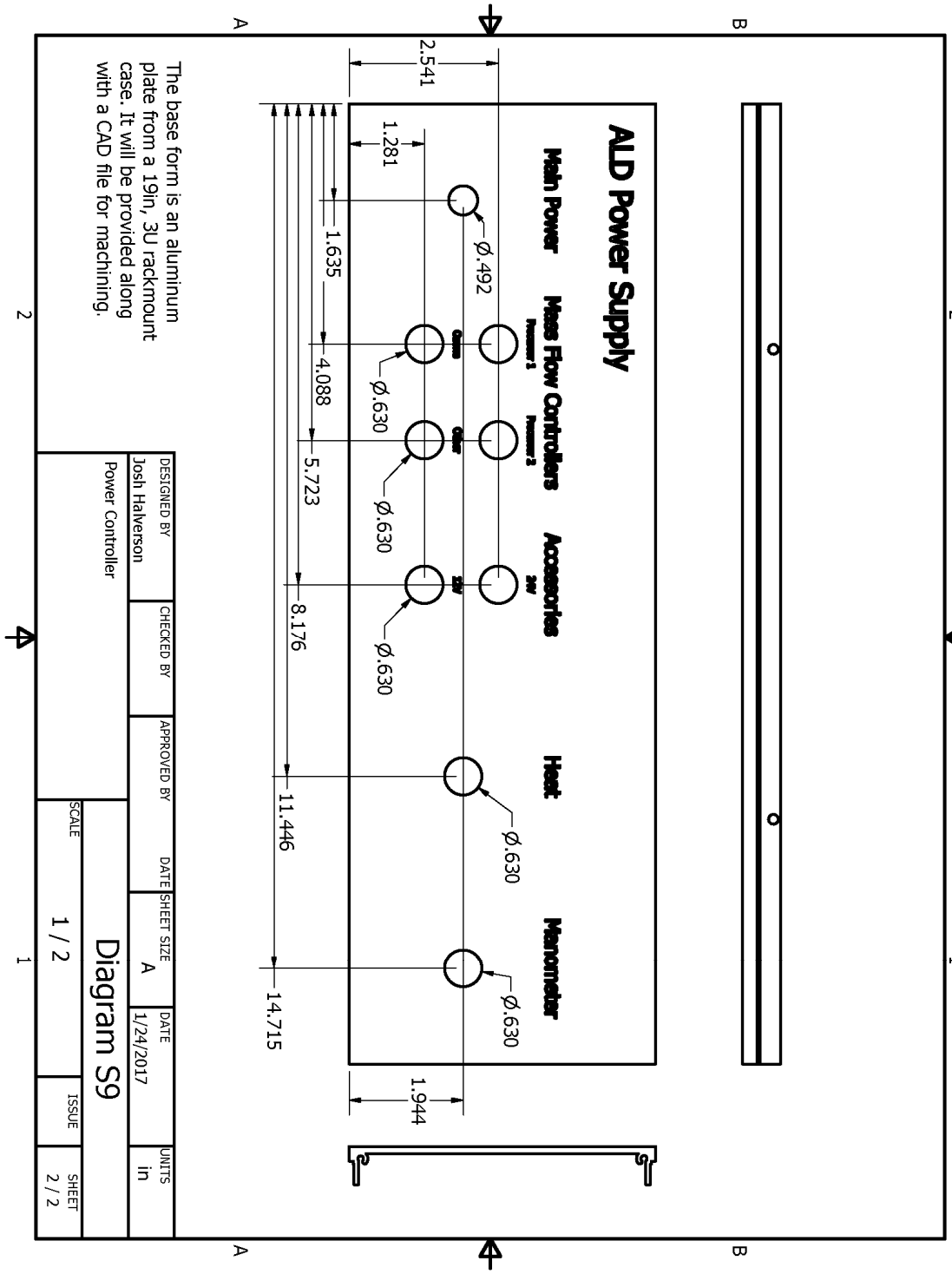

References

1. Faraday, M., The Bakerian Lecture: On the Relations of Gold and other Metals to Light. *Proceedings of the Royal Society of London* **1856,** *8* (ArticleType: research-article / Full publication date: 1856 - 1857 / Copyright © 1856 The Royal Society), 356-361.
2. Henglein, A., Mechanism of Reactions on Colloidal Microelectrodes and Size Quantization Effects. In *Electrochemistry II*, Steckhan, E., Ed. Springer Berlin / Heidelberg: 1988; Vol. 143, pp 113-180.
3. Brus, L., Quantum crystallites and nonlinear optics. *Appl. Phys. A: Mater. Sci. Process.* **1991,** *53* (6), 465-474.
4. Ostwald, W., *Introduction to theoretical and applied colloid chemistry, "the world of neglected dimensions,"*. 1st ed.; John Wiley & Sons: New York, 1917.
5. Weller, H., Colloidal Semiconductor Q-Particles: Chemistry in the Transition Region Between Solid State and Molecules. *Angew. Chem., Int. Ed. Engl.* **1993,** *32* (1), 41-53.
6. Darwent, J. R., H2 production photosensitized by aqueous semiconductor dispersions. *J. Chem. Soc., Faraday Trans. 2* **1981,** *77* (9), 1703-1709.
7. Norris, D. J.; Efros, A. L.; Rosen, M.; Bawendi, M. G., Size dependence of exciton fine structure in CdSe quantum dots. *Phys. Rev. B.* **1996,** *53* (24), 16347.
8. Norris, D. J.; Bawendi, M. G., Measurement and assignment of the size-dependent optical spectrum in CdSe quantum dots. *Phys. Rev. B.* **1996,** *53* (24), 16338.
9. Murray, C. B.; Norris, D. J.; Bawendi, M. G., Synthesis and characterization of nearly monodisperse CdE (E = sulfur, selenium, tellurium) semiconductor nanocrystallites. *J. Am. Chem. Soc.* **1993,** *115* (19), 8706-8715.
10. Bawendi, M. G.; Carroll, P. J.; Wilson, W. L.; Brus, L. E., Luminescence properties of cadmium selenide quantum crystallites: resonance between interior and surface localized states. *J. Chem. Phys.* **1992,** *96* (Copyright (C) 2011 American Chemical Society (ACS). All Rights Reserved.), 946-54.
11. Norris, D. J., Electronic Structure in Semiconductor Nanocrystals: Optical Experiment. In *Nanocrystal Quantum Dots*, 2nd ed.; Klimov, V. I., Ed. CRC Press: 2010; pp 63-96.
12. Yu, P. Y.; Cardona, M., *Fundamentals of Semiconductors: Physics and Materials Properties*. 4th ed.; Springer: London, 2010; p 775.
13. Bryan, J. D.; Gamelin, D. R., Doped Semiconductor Nanocrystals: Synthesis, Characterization, Physical Properties, and Applications. In *Prog. Inorg. Chem.*, Karlin, K. D., Ed. John Wiley & Sons, Inc.: 2005; Vol. 54, pp 47-126.
14. Mikulec, F. V.; Kuno, M.; Bennati, M.; Hall, D. A.; Griffin, R. G.; Bawendi, M. G., Organometallic Synthesis and Spectroscopic Characterization of Manganese-Doped CdSe Nanocrystals. *J. Am. Chem. Soc.* **2000,** *122* (11), 2532-2540.
15. Erwin, S. C.; Zu, L.; Haftel, M. I.; Efros, A. L.; Kennedy, T. A.; Norris, D. J., Doping semiconductor nanocrystals. *Nature* **2005,** *436* (7047), 91-94.
16. Beaulac, R.; Ochsenbein, S. T.; Gamelin, D. R., Colloidal Transition-Metal-Doped

Quantum Dots. In *Nanocrystal Quantum Dots*, 2nd ed.; Klimov, V. I., Ed. Taylor & Francis Group: Boca Raton, 2010; pp 397-453.
17. Norris, D. J.; Efros, A. L.; Erwin, S. C., Doped Nanocrystals. *Science* **2008,** *319* (5871), 1776-1779.
18. Bhargava, R. N.; Gallagher, D.; Hong, X.; Nurmikko, A., Optical properties of manganese-doped nanocrystals of zinc sulfide. *Phys. Rev. Lett.* **1994,** *72* (Copyright (C) 2011 American Chemical Society (ACS). All Rights Reserved.), 416-19.
19. Norris, D. J.; Yao, N.; Charnock, F. T.; Kennedy, T. A., High-Quality Manganese-Doped ZnSe Nanocrystals. *Nano Lett.* **2000,** *1* (1), 3-7.
20. Ji, T.; Jian, W.-B.; Fang, J., The First Synthesis of Pb1-xMnxSe Nanocrystals. *J. Am. Chem. Soc.* **2003,** *125* (28), 8448-8449.
21. Son, D. H.; Hughes, S. M.; Yin, Y.; Paul Alivisatos, A., Cation Exchange Reactions in Ionic Nanocrystals. *Science* **2004,** *306* (5698), 1009-1012.
22. Yu, D.; Wang, C.; Guyot-Sionnest, P., n-Type Conducting CdSe Nanocrystal Solids. *Science* **2003,** *300* (5623), 1277-1280.
23. Shim, M.; Wang, C.; Norris, D. J.; Guyot-Sionnest, P., Doping and charging in colloidal semiconductor nanocrystals. *MRS Bull.* **2001,** *26* (Copyright (C) 2011 American Chemical Society (ACS). All Rights Reserved.), 1005-1008.
24. Shim, M.; Guyot-Sionnest, P., n-type colloidal semiconductor nanocrystals. *Nature* **2000,** *407* (6807), 981-983.
25. Roy, S.; Tuinenga, C.; Fungura, F.; Dagtepe, P.; Chikan, V.; Jasinski, J., Progress toward Producing n-Type CdSe Quantum Dots: Tin and Indium Doped CdSe Quantum Dots. *J. Phys. Chem. C* **2009,** *113* (30), 13008-13015.
26. Tuinenga, C.; Jasinski, J.; Iwamoto, T.; Chikan, V., In Situ Observation of Heterogeneous Growth of CdSe Quantum Dots: Effect of Indium Doping on the Growth Kinetics. *ACS Nano* **2008,** *2* (7), 1411-1421.
27. Mandal, P. K.; Chikan, V., Plasmon−Phonon Coupling in Charged n-Type CdSe Quantum Dots: A THz Time-Domain Spectroscopic Study. *Nano Lett.* **2007,** *7* (8), 2521-2528.
28. Steigerwald, M. L.; Alivisatos, A. P.; Gibson, J. M.; Harris, T. D.; Kortan, R.; Muller, A. J.; Thayer, A. M.; Duncan, T. M.; Douglass, D. C.; Brus, L. E., Surface derivatization and isolation of semiconductor cluster molecules. *J. Am. Chem. Soc.* **1988,** *110* (10), 3046-3050.
29. Dannhauser, T.; O'Neil, M.; Johansson, K.; Whitten, D.; McLendon, G., Photophysics of quantized colloidal semiconductors. Dramatic luminescence enhancement by binding of simple amines. *J. Phys. Chem.* **1986,** *90* (23), 6074-6076.
30. LaMer, V. K.; Dinegar, R. H., Theory, Production and Mechanism of Formation of Monodispersed Hydrosols. *J. Am. Chem. Soc.* **1950,** *72* (11), 4847-4854.
31. Tricot, Y. M.; Fendler, J. H., Visible light induced hydrogen production from in situ generated colloidal rhodium-coated cadmium sulfide in surfactant vesicles. *J. Am. Chem. Soc.* **1984,** *106* (8), 2475-2476.
32. Stramel, R. D.; Nakamura, T.; Thomas, J. K., Photophysical and photochemical properties of CdS with limited dimensions. *J. Chem. Soc., Faraday Trans. 1* **1988,** *84* (5), 1287-1300.

33. Peng, Z. A.; Peng, X., Formation of High-Quality CdTe, CdSe, and CdS Nanocrystals Using CdO as Precursor. *J. Am. Chem. Soc.* **2000,** *123* (1), 183-184.
34. Talapin, D. V.; Rogach, A. L.; Kornowski, A.; Haase, M.; Weller, H., Highly Luminescent Monodisperse CdSe and CdSe/ZnS Nanocrystals Synthesized in a Hexadecylamine−Trioctylphosphine Oxide−Trioctylphospine Mixture. *Nano Lett.* **2001,** *1* (4), 207-211.
35. Nicolau, Y. F., Solution deposition of thin solid compound films by a successive ionic-layer adsorption and reaction process. *Applications of Surface Science* **1985,** *22-23* (Part 2), 1061-1074.
36. Li, J. J.; Wang, Y. A.; Guo, W.; Keay, J. C.; Mishima, T. D.; Johnson, M. B.; Peng, X., Large-Scale Synthesis of Nearly Monodisperse CdSe/CdS Core/Shell Nanocrystals Using Air-Stable Reagents via Successive Ion Layer Adsorption and Reaction. *J. Am. Chem. Soc.* **2003,** *125* (41), 12567-12575.
37. Carbone, L.; Nobile, C.; De Giorgi, M.; Sala, F. D.; Morello, G.; Pompa, P.; Hytch, M.; Snoeck, E.; Fiore, A.; Franchini, I. R.; Nadasan, M.; Silvestre, A. F.; Chiodo, L.; Kudera, S.; Cingolani, R.; Krahne, R.; Manna, L., Synthesis and Micrometer-Scale Assembly of Colloidal CdSe/CdS Nanorods Prepared by a Seeded Growth Approach. *Nano Lett.* **2007,** *7* (10), 2942-2950.
38. Willoughby, A. F. W., Atomic diffusion in semiconductors. *Reports on Progress in Physics* **1978,** *41* (10), 1665.
39. Mokari, T.; Aharoni, A.; Popov, I.; Banin, U., Diffusion of Gold into InAs Nanocrystals. *Angewandte Chemie International Edition* **2006,** *45* (47), 8001-8005.
40. Sahu, A.; Kang, M. S.; Kompch, A.; Notthoff, C.; Wills, A. W.; Deng, D.; Winterer, M.; Frisbie, C. D.; Norris, D. J., Electronic Impurity Doping in CdSe Nanocrystals. *Nano Lett.* **2012,** *12* (5), 2587-2594.
41. Viswanatha, R.; Brovelli, S.; Pandey, A.; Crooker, S. A.; Klimov, V. I., Copper-Doped Inverted Core/Shell Nanocrystals with "Permanent" Optically Active Holes. *Nano Lett.* **2011**.
42. Lytle, F. W., The EXAFS family tree: a personal history of the development of extended X-ray absorption fine structure. *Journal of Synchrotron Radiation* **1999,** *6* (3), 123-134.
43. Winterer, M., XAFS - A Data Analysis Program for Materials Science. *J. Phys. IV France* **1997,** *7* (C2), C2-243-C2-244.
44. Ravel, B.; Newville, M., ATHENA, ARTEMIS, HEPHAESTUS: data analysis for X-ray absorption spectroscopy using IFEFFIT. *Journal of Synchrotron Radiation* **2005,** *12* (4), 537-541.
45. Reiss, P.; Bleuse, J.; Pron, A., Highly Luminescent CdSe/ZnSe Core/Shell Nanocrystals of Low Size Dispersion. *Nano Lett.* **2002,** *2* (Copyright (C) 2011 American Chemical Society (ACS). All Rights Reserved.), 781-784.
46. Wills, A., University of Minnesota: Minneapolis, 2011.
47. Reiss, P.; Carayon, S.; Bleuse, J.; Pron, A., Low polydispersity core/shell nanocrystals of CdSe/ZnSe and CdSe/ZnSe/ZnS type: preparation and optical studies. *Synth. Met.* **2003,** *139* (3), 649-652.
48. Cumberland, S. L.; Hanif, K. M.; Javier, A.; Khitrov, G. A.; Strouse, G. F.; Woessner, S. M.; Yun, C. S., Inorganic Clusters as Single-Source Precursors for

Preparation of CdSe, ZnSe, and CdSe/ZnS Nanomaterials. *Chem. Mater.* **2002,** *14* (4), 1576-1584.
49. Yu, W. W.; Qu, L.; Guo, W.; Peng, X., Experimental Determination of the Extinction Coefficient of CdTe, CdSe, and CdS Nanocrystals. *Chem. Mater.* **2003,** *15* (14), 2854-2860.
50. Berger, L. I., *Semiconductor Materials*. 1st ed.; CRC Press: Boca Raton, 1997.
51. Gupta, T. K.; Doh, J., Optical properties of polycrystalline cadmium selenide (CdSe) films. *J. Mater. Res.* **1992,** *7* (Copyright (C) 2011 American Chemical Society (ACS). All Rights Reserved.), 1243-6.
52. Ishizumi, A.; Kanemitsu, Y., Photoluminescence Spectra and Dynamics of Al^{3+}- and Ag^{+}- Doped CdS Nanocrystals. *J. Phys. Soc. Jpn.* **2010,** *79* (9), 093706-1-093706-4.
53. Xie, R.; Kolb, U.; Li, J.; Basch√©, T.; Mews, A., Synthesis and Characterization of Highly Luminescent CdSe-Core CdS/Zn0.5Cd0.5S/ZnS Multishell Nanocrystals. *J. Am. Chem. Soc.* **2005,** *127* (20), 7480-7488.
54. Fonoberov, V. A.; Balandin, A. A., Origin of ultraviolet photoluminescence in ZnO quantum dots: Confined excitons versus surface-bound impurity exciton complexes. *Appl. Phys. Lett.* **2004,** *85* (24), 5971-5973.
55. Wills, A. W.; Kang, M. S.; Wentz, K. M.; Hayes, S. E.; Sahu, A.; Gladfelter, W. L.; Norris, D. J., Synthesis and characterization of Al- and In-doped CdSe nanocrystals. *J. Mater. Chem.* **2012,** *22* (13), 6335-6342.
56. Mocatta, D.; Cohen, G.; Schattner, J.; Millo, O.; Rabani, E.; Banin, U., Heavily Doped Semiconductor Nanocrystal Quantum Dots. *Science* **2011,** *332* (6025), 77-81.
57. Karan, N. S.; Sarma, D. D.; Kadam, R. M.; Pradhan, N., Doping Transition Metal (Mn or Cu) Ions in Semiconductor Nanocrystals. *The Journal of Physical Chemistry Letters* **2010,** *1* (19), 2863-2866.
58. Perna, G.; Capozzi, V.; Ambrico, M.; Augelli, V.; Ligonzo, T.; Minafra, A.; Schiavulli, L.; Pallara, M., Structural and optical characterization of Zn doped CdSe films. *Appl. Surf. Sci.* **2004,** *233* (1-4), 366-372.
59. Rehr, J. J.; Albers, R. C., Theoretical approaches to x-ray absorption fine structure. *Reviews of Modern Physics* **2000,** *72* (3), 621-654.
60. Rehr, J. J.; Kas, J. J.; Vila, F. D.; Prange, M. P.; Jorissen, K., Parameter-free calculations of X-ray spectra with FEFF9. *Physical Chemistry Chemical Physics* **2010,** *12* (21), 5503-5513.
61. Xu, Y.-N.; Ching, W. Y., Electronic, optical, and structural properties of some wurtzite crystals. *Physical Review B* **1993,** *48* (7), 4335-4351.
62. Beaulac, R.; Archer, P. I.; Gamelin, D. R., Luminescence in colloidal Mn2+-doped semiconductor nanocrystals. *J. Solid State Chem.* **2008,** *181* (7), 1582-1589.
63. Peng, X.; Schlamp, M. C.; Kadavanich, A. V.; Alivisatos, A. P., Epitaxial Growth of Highly Luminescent CdSe/CdS Core/Shell Nanocrystals with Photostability and Electronic Accessibility. *J. Am. Chem. Soc.* **1997,** *119* (30), 7019-7029.
64. Luo, H.; Tuinenga, C.; Guidez, E. B.; Lewis, C.; Shipman, J.; Roy, S.; Aikens, C. M.; Chikan, V., Synthesis and Characterization of Gallium-Doped CdSe Quantum Dots. *The Journal of Physical Chemistry C* **2015,** *119* (19), 10749-10757.

65. Raola, O. E.; Strouse, G. F., Synthesis and Characterization of Eu-Doped Cadmium Selenide Nanocrystals. *Nano Lett.* **2002,** *2* (12), 1443-1447.
66. Cargnello, M.; Johnston-Peck, A. C.; Diroll, B. T.; Wong, E.; Datta, B.; Damodhar, D.; Doan-Nguyen, V. V. T.; Herzing, A. A.; Kagan, C. R.; Murray, C. B., Substitutional doping in nanocrystal superlattices. *Nature* **2015,** *524* (7566), 450-453.
67. Wills, A. W.; Kang, M. S.; Khare, A.; Gladfelter, W. L.; Norris, D. J., Thermally Degradable Ligands for Nanocrystals. *ACS Nano* **2010,** *4* (8), 4523-4530.
68. Suntola, T. S.; Pakkala, A. J.; Lindfors, S. G. Apparatus For Performing Growth of Compound Thin Films. 4389973, 1983.
69. Martinson, A. B. F.; DeVries, M. J.; Libera, J. A.; Christensen, S. T.; Hupp, J. T.; Pellin, M. J.; Elam, J. W., Atomic Layer Deposition of Fe2O3 Using Ferrocene and Ozone. *The Journal of Physical Chemistry C* **2011,** *115* (10), 4333-4339.
70. Kukli, K.; Ritala, M.; Leskelä, M.; Sajavaara, T.; Keinonen, J.; Hegde, R. I.; Gilmer, D. C.; Tobin, P. J., Properties of Oxide Film Atomic Layer Deposited from Tetraethoxy Silane, Hafnium Halides, and Water. *Journal of The Electrochemical Society* **2004,** *151* (5), F98-F104.
71. Alnes, M. E.; Monakhov, E.; Fjellvåg, H.; Nilsen, O., Atomic Layer Deposition of Copper Oxide using Copper(II) Acetylacetonate and Ozone. *Chemical Vapor Deposition* **2012,** *18* (4-6), 173-178.
72. Tommi, T.; Maarit, K., Atomic layer deposition of ZnO: a review. *Semiconductor Science and Technology* **2014,** *29* (4), 043001.
73. Knoops, H. C. M.; Elam, J. W.; Libera, J. A.; Kessels, W. M. M., Surface Loss in Ozone-Based Atomic Layer Deposition Processes. *Chemistry of Materials* **2011,** *23* (9), 2381-2387.
74. Martin, P. M., Chapter 1 - Deposition Technologies: An Overview. In *Handbook of Deposition Technologies for Films and Coatings (Third Edition)*, William Andrew Publishing: Boston, 2010; pp 1-31.
75. Knez, M.; Nielsch, K.; Niinistö, L., Synthesis and Surface Engineering of Complex Nanostructures by Atomic Layer Deposition. *Advanced Materials* **2007,** *19* (21), 3425-3438.
76. Carlsson, J.-O.; Martin, P. M., Chapter 7 - Chemical Vapor Deposition. In *Handbook of Deposition Technologies for Films and Coatings (Third Edition)*, William Andrew Publishing: Boston, 2010; pp 314-363.
77. Pakkala, A.; Putkonen, M., Chapter 8 - Atomic Layer Deposition. In *Handbook of Deposition Technologies for Films and Coatings (Third Edition)*, William Andrew Publishing: Boston, 2010; pp 364-391.
78. Suntola, T.; Antson, J. Method for producing compound thin films. US4058430 A, 1977.
79. George, S. M., Atomic Layer Deposition: An Overview. *Chemical Reviews* **2010,** *110* (1), 111-131.
80. Leskelä, M.; Ritala, M., Atomic Layer Deposition Chemistry: Recent Developments and Future Challenges. *Angewandte Chemie International Edition* **2003,** *42* (45), 5548-5554.
81. Ahonen, M.; Pessa, M.; Suntola, T., A study of ZnTe films grown on glass

substrates using an atomic layer evaporation method. *Thin Solid Films* **1980,** *65* (3), 301-307.
82. Tammenmaa, M.; Koskinen, T.; Hiltunen, L.; Niinistö, L.; Leskelä, M., Zinc chalcogenide thin films grown by the atomic layer epitaxy technique using zinc acetate as source material. *Thin Solid Films* **1985,** *124* (2), 125-128.
83. Puurunen, R. L., Surface chemistry of atomic layer deposition: A case study for the trimethylaluminum/water process. *Journal of Applied Physics* **2005,** *97* (12), 121301.
84. Edwards, P. P.; Porch, A.; Jones, M. O.; Morgan, D. V.; Perks, R. M., Basic materials physics of transparent conducting oxides. *Dalton Transactions* **2004,** (19), 2995-3002.
85. Tadatsugu, M., Transparent conducting oxide semiconductors for transparent electrodes. *Semiconductor Science and Technology* **2005,** *20* (4), S35.
86. Meyer, B. K.; Polity, A.; Reppin, D.; Becker, M.; Hering, P.; Klar, P. J.; Sander, T.; Reindl, C.; Benz, J.; Eickhoff, M.; Heiliger, C.; Heinemann, M.; Bläsing, J.; Krost, A.; Shokovets, S.; Müller, C.; Ronning, C., Binary copper oxide semiconductors: From materials towards devices. *physica status solidi (b)* **2012,** *249* (8), 1487-1509.
87. Tate, J.; Keszler, D. A., p-Type Wide-Band-Gap Semiconductors for Transparent Electronics. In *Transparent Electronics*, John Wiley & Sons, Ltd: 2010; pp 61-87.
88. Kawazoe, H.; Yasukawa, M.; Hyodo, H.; Kurita, M.; Yanagi, H.; Hosono, H., P-type electrical conduction in transparent thin films of CuAlO2. *Nature* **1997,** *389* (6654), 939-942.
89. Salavati-Niasari, M.; Davar, F.; Farhadi, M., Synthesis and characterization of spinel-type CuAl2O4 nanocrystalline by modified sol–gel method. *Journal of Sol-Gel Science and Technology* **2009,** *51* (1), 48-52.
90. Yanagi, H.; Inoue, S.-i.; Ueda, K.; Kawazoe, H.; Hosono, H.; Hamada, N., Electronic structure and optoelectronic properties of transparent p-type conducting CuAlO2. *Journal of Applied Physics* **2000,** *88* (7), 4159-4163.
91. Huo, J.; Solanki, R.; McAndrew, J., Characteristics of copper films produced via atomic layer deposition. *Journal of Materials Research* **2002,** *17* (09), 2394-2398.
92. Solanki, R.; Pathangey, B., Atomic Layer Deposition of Copper Seed Layers. *Electrochemical and Solid-State Letters* **2000,** *3* (10), 479-480.
93. Mårtensson, P.; Carlsson, J.-O., Atomic Layer Epitaxy of Copper on Tantalum. *Chemical Vapor Deposition* **1997,** *3* (1), 45-50.
94. Törndahl, T.; Ottosson, M.; Carlsson, J.-O., Growth of copper metal by atomic layer deposition using copper(I) chloride, water and hydrogen as precursors. *Thin Solid Films* **2004,** *458* (1–2), 129-136.
95. Lim, B. S.; Rahtu, A.; Park, J.-S.; Gordon, R. G., Synthesis and Characterization of Volatile, Thermally Stable, Reactive Transition Metal Amidinates. *Inorganic Chemistry* **2003,** *42* (24), 7951-7958.
96. Doppelt, P., Why is coordination chemistry stretching the limits of micro-electronics technology? *Coordination Chemistry Reviews* **1998,** *178–180, Part 2*, 1785-1809.
97. Li, Z.; Barry, S. T.; Gordon, R. G., Synthesis and Characterization of Copper(I)

Amidinates as Precursors for Atomic Layer Deposition (ALD) of Copper Metal. *Inorganic Chemistry* **2005,** *44* (6), 1728-1735.
98. Park, K.-H.; Bradley, A. Z.; Thompson, J. S.; Marshall, W. J., Nonfluorinated Volatile Copper(I) 1,3-Diketiminates as Precursors for Cu Metal Deposition via Atomic Layer Deposition. *Inorganic Chemistry* **2006,** *45* (21), 8480-8482.
99. Park, K.-H.; Marshall, W. J., Remarkably Volatile Copper(II) Complexes of N,N'-Unsymmetrically Substituted 1,3-Diketimines as Precursors for Cu Metal Deposition via CVD or ALD. *Journal of the American Chemical Society* **2005,** *127* (26), 9330-9331.
100. Kim, Y.; Kim, C. G.; Chung, T. M.; Lee, S. S.; An, K. S.; Yang, T. S.; Jang, H. S. Volatile copper aminoalkoxide complex and deposition of copper thin film using same. 2006.
101. Dhakal, D.; Waechtler, T.; Schulz, S. E.; Gessner, T.; Lang, H.; Mothes, R.; Tuchscherer, A., Surface chemistry of a Cu(I) beta-diketonate precursor and the atomic layer deposition of Cu2O on SiO2 studied by x-ray photoelectron spectroscopy. *Journal of Vacuum Science & Technology A: Vacuum, Surfaces, and Films* **2014,** *32* (4), 041505.
102. King, S. W.; Nemanich, R. J.; Davis, R. F., Cleaning of pyrolytic hexagonal boron nitride surfaces. *Surface and Interface Analysis* **2015,** *47* (7), 798-803.
103. Jenkins, F.; White, H., *Fundamentals of Optics*. 3rd ed.; McGRAW-HILL: New York, 1957.
104. Fujiwara, H., *Spectroscopic Ellipsometry*. Maruzen Co. Ltd: Tokyo, 2007.
105. Pouchou, J.-L., X-Ray Microanalysis of Thin Surface Films and Coatings. *Microchimica Acta* **2002,** *138* (3), 133-152.
106. Donovan, J. J.; Lowers, H. A.; Rusk, B. G., Improved electron probe microanalysis of trace elements in quartz. *American Mineralogist* **2011,** *96* (2-3), 274-282.
107. Armstrong, J. T., Quantitative analysis of silicates and oxide minerals: Comparison of Monte-Carlo, ZAF and Phi-Rho-Z procedures. *Microbeam Analysis* **1988**, 239-246.
108. Ohring, M., *Materials Science of Thin Films*. 2nd ed.; Academic Press: 2002.
109. Tauc, J.; Grigorovici, R.; Vancu, A., Optical Properties and Electronic Structure of Amorphous Germanium. *physica status solidi (b)* **1966,** *15* (2), 627-637.
110. Cocke, D.; Peterson, E.; Gomes, J.; Rutman, D.; Reed, M.; Hossain, M. A. In *Characterization of copper oxides by EDS-SEM depth profiling, EIS and XRD*, Minerals, Metals & Materials Society: 2009; pp 145-152.
111. Chawla, S. K.; Sankarraman, N.; Payer, J. H., Diagnostic spectra for XPS analysis of Cu・O・S・H compounds. *Journal of Electron Spectroscopy and Related Phenomena* **1992,** *61* (1), 1-18.
112. Vasquez, R. P., Cu2O by XPS. *Surface Science Spectra* **1998,** *5* (4), 257-261.
113. Vasquez, R. P., CuO by XPS. *Surface Science Spectra* **1998,** *5* (4), 262-266.
114. Moulder, J. F.; Stickle, W. F.; Sobol, P. E.; Bomben, K. D., *Handbook of X-ray Photoelectron Spectroscopy*. Perkin-Elmer: Eden Prairie, MN, 1992.
115. Vasquez, R. P., Cu(OH)2 by XPS. *Surface Science Spectra* **1998,** *5* (4), 267-272.
116. Dey, G.; Elliott, S. D., Mechanism for the Atomic Layer Deposition of Copper Using Diethylzinc as the Reducing Agent: A Density Functional Theory Study

Using Gas-Phase Molecules as a Model. *The Journal of Physical Chemistry A* **2012,** *116* (35), 8893-8901.

117. Lee, B. H.; Hwang, J. K.; Nam, J. W.; Lee, S. U.; Kim, J. T.; Koo, S.-M.; Baunemann, A.; Fischer, R. A.; Sung, M. M., Low-Temperature Atomic Layer Deposition of Copper Metal Thin Films: Self-Limiting Surface Reaction of Copper Dimethylamino-2-propoxide with Diethylzinc. *Angewandte Chemie International Edition* **2009,** *48* (25), 4536-4539.